EĞİTİM yayınevi

CURRENT STUDIES IN ELECTRICAL ELECTRONICS AND COMPUTER ENGINEERING

EDITORS:
PROF. DR. ISMAIL SARITAS
ASSOC. PROF. DR. ILKER ALI OZKAN

CURRENT STUDIES IN ELECTRICAL ELECTRONICS AND COMPUTER ENGINEERING

EDITORS:
PROF. DR. ISMAIL SARITAS
ASSOC. PROF. DR. ILKER ALI OZKAN

EĞİTİM
yayınevi

CURRENT STUDIES IN ELECTRICAL ELECTRONICS AND COMPUTER ENGINEERING

Editors: Prof. Dr. Ismail Saritas, Assoc. Prof. Dr. Ilker Ali Ozkan

Executive Editor: Yusuf Ziya Aydoğan (yza@egitimyayinevi.com)
Publishing Coordinator: Yusuf Yavuz (yusufyavuz@egitimyayinevi.com)
Interior Designer: Eğitim Yayınevi Graphics Unit
Cover Designer: Eğitim Yayınevi Graphics Unit

Republic of Türkiye Ministry of Tourizm and Culture
Publisher Certificate No: 47830

E-ISBN: 978-625-8468-50-3
1. Edition, December 2022

Library Information Card
CURRENT STUDIES IN ELECTRICAL ELECTRONICS AND COMPUTER ENGINEERING
Editors: Prof. Dr. Ismail Saritas, Assoc. Prof. Dr. Ilker Ali Ozkan
p.156, 165x240 mm
Includes references, no index.
E-ISBN: 978-625-8468-50-3

EĞİTİM
yayınevi

Publisher Turkey Office: İstanbul: Eğitim Yayınevi Tic. Ltd. Şti., Atakent mah. Yasemen sok. No: 4/B, Ümraniye, İstanbul, Türkiye

Konya: Eğitim Yayınevi Tic. Ltd. Şti., Fevzi Çakmak Mah. 10721 Sok. B Blok, No: 16/B, Safakent, Karatay, Konya, Türkiye
+90 332 351 92 85, +90 533 151 50 42, 0 332 502 50 42
bilgi@egitimyayinevi.com

Publisher USA Office: New York: Egitim Publishing Group, Inc.
P.O. Box 768/Armonk, New York, 10504-0768, United States of America
americaoffice@egitimyayinevi.com

Logistics and Shipping Center: Kitapmatik Lojistik ve Sevkiyat Merkezi, Fevzi Çakmak Mah. 10721 Sok. B Blok, No: 16/B, Safakent, Karatay, Konya, Türkiye
sevkiyat@egitimyayinevi.com

Bookstore Branch: Eğitim Kitabevi, Şükran mah. Rampalı 121, Meram, Konya, Türkiye
+90 332 499 90 00
bilgi@egitimkitabevi.com

Internet Sales: www.kitapmatik.com.tr
+90 537 512 43 00
bilgi@kitapmatik.com.tr

ilk okuyan siz olun
kitapmatik
internetteki kitapçınız

TABLE OF CONTENTS

Chapter 1

MEDICAL IMAGING TOOL OF THE FUTURE: MAGNETIC PARTICLE IMAGING (MPI)

Muhammad IRFAN [1], Nurcan DOGAN[2]

1 Gebze Technical University, Faculty of Engineering, Electronics Engineering, Kocaeli, Türkiye
2 Gebze Technical University, Faculty of Science, Physics Department, Kocaeli, Türkiye

INTRODUCTION

Magnetic particle imaging (MPI) is a novel imaging tool that offers great spatial resolution and minimal scanning time as compared to well-known magnetic resonance imaging (MRI) and computed tomography (CT). MPI was disclosed to the research community in 2005 which employs superparamagnetic iron oxide nanoparticles (SPIONs) as tracer agents [1]. The SPIONs are super magnetic nanoparticles that have been utilized as contrast agents to minimize background noise. In contrast, SPIONs are the sole signal source for MPI. The development of medical imaging, diagnostic tools, and therapeutic devices are interrelated. Magnetization of the positive contrast agent utilized in MPI outperforms the proton magnetization in MRI which becomes the source of this invention [2].

BRIEF REVIEW OF MEDICAL IMAGING TECHNIQUES

Biological tissues do not generate background signals for the MPI technique. Hence, MPI is a zero-depth attenuation technique. It is fundamentally distinct from other imaging tools such as MRI, Computed Tomography (CT), but resembles Positron Emission Tomography (PET) [3]. A comparison of some medical imaging modalities adapted from the reference [5-16] is presented in Table 1. The high Spatio-temporal resolution, nanomolar sensitivity, and super contrast agent capability of MPI make it a potential candidate for the advancement of pre-clinical and clinical applications [4]. Since its invention, MPI has expanded rapidly [16-18], resulting in a wide range of biomedical applications including stem cell labeling and tracking [19], vascular and perfusion imaging [14], lung imaging [20], and magnetic hyperthermia [21, 22].

Table 1. A brief comparison of most common medical imaging techniques [5-16].

Modality	Ultrasound	CT	MRI	SPECT	MPI
Spatial Resolution*	1 mm	<1 mm	1 mm	3-10 mm	< 1 mm (Preclinical)
Acquisition time*	< 1 s	1 s	10 s- 30 min	1 min	<0.1 s (preclinical)
Sensitivity*	~10-12 Molar	Millimolar	Millimolar	Picomolar	Micromolar (preclinical)
Quantifiability	No	Yes	No	Yes	Yes
Harmfulness	Cavitation and heating	Radiation	Peripheral nerve stimulation and heating	Radiation	Peripheral nerve stimulation and heating
Contrast agents/tracers	Microbubbles	Iodine	Gadolinium,	Radionuclide	SPIO
Imaging method	Anatomic scanning	Anatomic scanning	Anatomic scanning	Tracer scanning	Tracer scanning

* These are widely accepted generalized values, subject to variation based on instrumentation and tracer agent specifications.

MAGNETIC NANOPARTICLES FOR MPI

Magnetic nanoparticles have a long history in medical imaging. MNPs with different magnetic cores and hydrodynamic coating are used for various medical applications. SPIONs have been used in MRI [23] as a negative contrast agent to suppress the background signal. However, MPI does not have a background signal issue. SPIONs are utilized as signal sources [1] to conduct an object scan (phantoms, in-vitro, and in-vivo applications) in MPI. SPIONs have been widely used in other biomedical applications such as hyperthermia therapy [24, 25], tissue repair [26, 27], drug delivery [28, 29], and stem cell tracking [30, 31]. A single-domain nanoparticle with possible functionalities adapted from reference [32] is pictorially represented in Figure 1. The thickness of the coating layers ensures the minimum particle-to-particle interaction that prevents agglomeration phenomena.

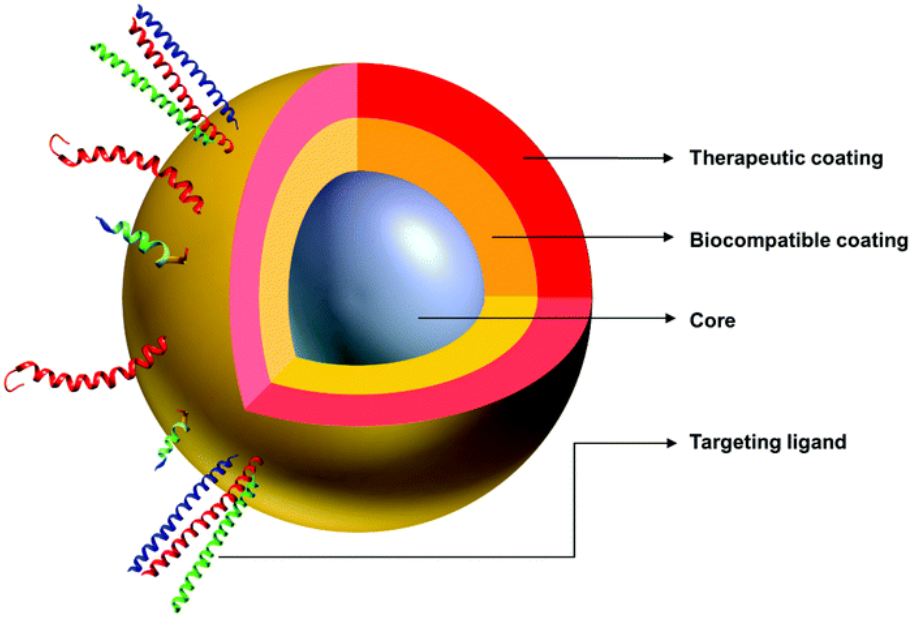

Figure 1. A single-domain magnetic nanoparticle with a magnetic core, hydrodynamic coating, and targeting ligand shows a brief representation of a tracer agent [32,33].

Magnetization Response

Superparamagnetic behavior is observed in Fe_3O_4 (magnetite) and γ-Fe_2O_4 (maghemite) which are fundamental SPIONs with magnetization similar to their bulk materials [37]. The magnetization and applied field of SPIONs have non-linear relations instead of linear relationships for paramagnetic materials. The magnetization behavior changes abruptly at low applied magnetic fields and stays at fixed magnetization levels at higher magnetic fields as shown in Figure 2. As the magnetic field increases magnetization becomes saturated after a certain point, so applying a higher magnetic field does not enhance particle magnetization. In MPI, a non-linear response in the dynamic range is utilized.

The relationship between the applied magnetic field and the magnetization response of the SPIONs can be mathematically expressed using the Langevin function [15,33];

$$\mathcal{L}(\xi) := \begin{cases} \left(\coth(\xi) - \frac{1}{\xi}\right) & \xi \neq 0 \\ 0 & \xi = 0 \end{cases} \quad (1)$$

All the nanoparticles are assumed at thermal equilibrium.

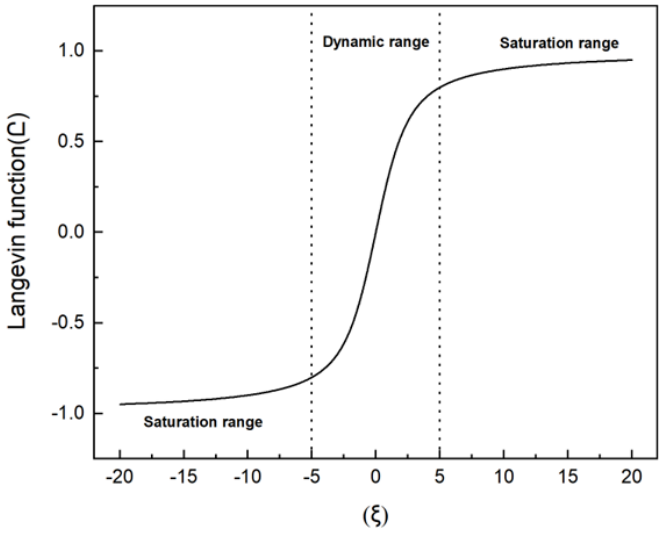

Figure 2. The SPIONs' magnetization is based on the Langevin function. It is abruptly changing from -5 to 5 (dynamic range). As the applied magnetic field increases, the Langevin function becomes saturated after a certain point [33].

SPIONs are composed of nanoscale magnetic nanoparticles. A particle's magnetic moment is denoted by the symbol m. The samples' magnetic moments are randomly orientated as a result of Brownian motion. Hence, the net magnetic movement of the sample is zero. ΔV is the volume of the magnetic nanoparticles. Overall, the magnetization (M) of the sample is expressed as [15,33];

$$M := \frac{1}{\Delta V} \sum_{i=0}^{N^r-1} m_i \quad (2)$$

MNPs follow the direction of the applied magnetic field. In the saturation range, nanoparticles are fully aligned to the applied field direction. If the relaxation time phenomenon is ignored, then magnetization at the applied magnetic field is easily expressed as [15,33];

$$\boldsymbol{M(H)} = M(H)e_H \quad (3)$$

The magnetization response of the MNPs based on the Langevin function can be calculated as [15,33];

$$M(H) = cm\mathcal{L}(\alpha H) \quad (4)$$

$$\alpha := \frac{\mu_0 m}{k_B T} \tag{5}$$

Here, T represents the temperature of the nanoparticles, while k_B is the Boltzmann constant. In the meantime, c in equation (4) represents the particle concentration. Similarly, m in equation (4) denotes the magnetic moment which can be calculated as [15,33];

$$m = V_c M_s \tag{6}$$

Here, V_c is the volume of the particle core, while M_s is the saturation level of the magnetization. If the particles have a diameter of D_c then the volume of the spherical particle can be calculated as [15,33];

$$V_c = \frac{1}{6}\pi D_c^3 \tag{7}$$

Practically, the iron concentration of the sample is more important as compared to particle concentration. If the iron concentration (c) is kept constant, then particle concentration has an inverse relation with its particle volume. Saturation magnetization can be expressed as [15,33];

$$M_s = cm \tag{8}$$

Magnetization is independent of particle size as presented in Figure 3. The magnetization response of SPIONs with core diameter from 5 nm to 45 nm have the same saturation level at higher excitation fields.

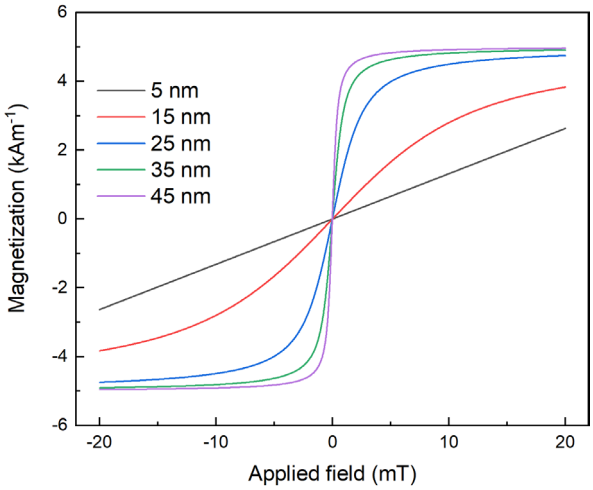

Figure 3. The magnetization of SPIONs (tracer agents) for magnetic core diameters ranging from 5 nm to 45 nm [33].

SPATIAL ENCODING

Spatial encoding is the primary goal of imaging tools (MPI, MRI) that use alternating gradient fields and constant magnetic fields. According to the Maxwell

configuration, the selection field of MPI is implemented using a field-free point (FFP) or field-free line (FFL) utilizing permanent magnets and/or electromagnets. To produce a selection field, direct current is applied to electromagnets in opposite directions, just as permanent magnet poles are positioned in opposition to one another. Permanent magnets or electromagnets in the form of discs or rings can produce a zero magnetic field point FFP while permanent magnets or electromagnets in the form of rectangles can produce a zero magnetic field line FFL. The implementation of FFP and FFL spatial encoding by permanent magnets and electromagnets are represented in Figure 4.

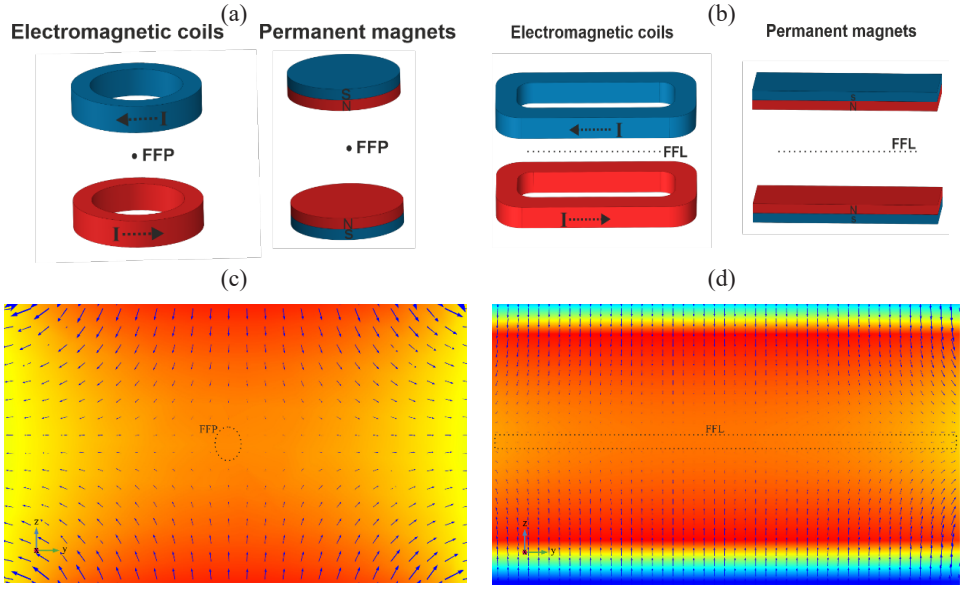

Figure 4. Fundamental selection fields for magnetic particle imaging scanners; (a) 3D view of Disc-shaped permanent magnets and ring-shaped electromagnets for the implementation of FFP (b) 3D view of rectangular-shaped permanent magnets and electromagnets for the implementation of FFL (c) 2D gradient field slice that encompasses FFP at the midpoint(d) 2D gradient field slice that encompasses FFL at the midpoint [33,34].

Basic Theory of the Selection Field

The selection fields for the MPI scanners are produced using permanent magnets and/or electromagnetic coils. A highly homogenous gradient field is required for artifact-free MPI imaging. The strength of the gradient field is a key factor in determining the field of view (FOV) of a scanned object. The MPI scanner's spatial resolution increases with a larger gradient field. However, it narrows the FOV's scanning coverage area. The gradient field (G) strength along the x and y axes is half of the z-axis value with a negative sign. The divergence of the magnetic field (B) in equation (9) is described by Gauss's law of magnetism.

$$G = G_x + G_y + G_z = \nabla \cdot \boldsymbol{B} = \frac{\partial B_x}{\partial x} + \frac{\partial B_y}{\partial y} + \frac{\partial B_z}{\partial z} = 0 \tag{9}$$

where $G_x := \frac{\partial B_x}{\partial x}$, $G_y := \frac{\partial B_y}{\partial y}$ and $G_z := \frac{\partial B_z}{\partial z}$

The following are the three gradient strengths' relationships:

$$G_z = -2G_x = -2G_y \tag{10}$$

The asymmetry of the selection field, which significantly affects the spatial resolution of MPI scanners is demonstrated by equations (9) and (10). The FOV has an ellipsoid shape due to the asymmetry of the gradient field relationship.

Permanent Magnet Design

Permanent magnets (PM) in disc shape can have their magnetic flux density analytically calculated in MATLAB and numerically simulated in COMSOL Multiphysics. Using equation (11), the permanent magnets' magnetic flux density at d distances from the middle can be written as [33,38];

$$B_{PM}(z) = \frac{B_r}{2}\left[\frac{z-d+\frac{L}{2}}{\sqrt{R^2+(z-d+\frac{L}{2})^2}} - \frac{z-d-\frac{L}{2}}{\sqrt{R^2+(z-d-\frac{L}{2})^2}}\right] \quad \text{for } (-d+\tfrac{L}{2}) < z < (d-\tfrac{L}{2}) \tag{11}$$

where d is the distance from the center of the disc-type permanent magnets from the midpoint, R is the radius, L is the thickness, and B_r is the remanent flux density.

With peak values at |d|, the magnetic flux density of the magnets linearly decays on either side (toward the middle point) along the z-axis. The magnetic field in the center of the system is canceled by the opposing responses from each side. The design and numerical simulation results of disc-shaped permanent magnet (NdFeB) based FFP spatial encoding is presented in Figure 5.

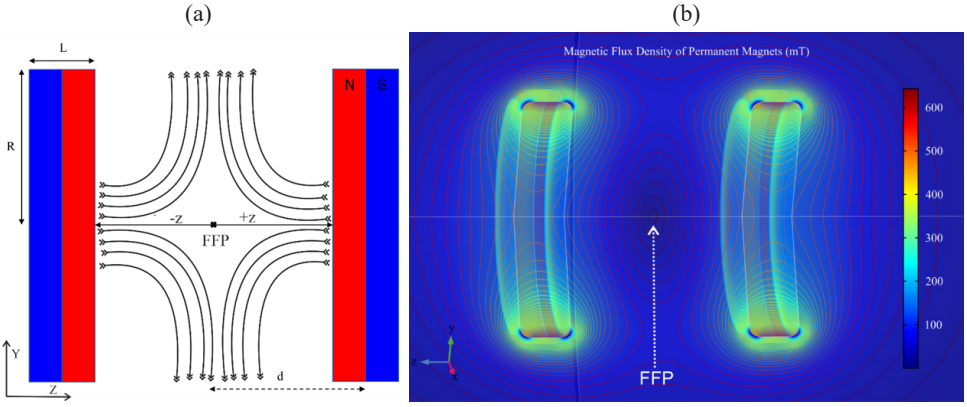

Figure 5. (a) NdFeB permanent magnets-based selection field design for the MPI scanner, (b) In COMSOL Multiphysics, a 2D axisymmetric numerical simulation of the configuration was conducted and demonstrates FFP at the midpoint [33,35].

Electromagnets Design

Electromagnets are used to design and simulate more precise and homogeneous selection fields for the MPI scanners. The magnetic flux density produced by the multi-layer electromagnetic coil [33,39] at d distance from the midpoint is theoretically modeled by using equation (12).

$$B_{EM}(z) = \frac{\mu_0 NI}{2L(R_{out} - R_{in})}\left[A \ln \frac{R_{out} + \sqrt{R_{out}^2 + A^2}}{R_{in} + \sqrt{R_{in}^2 + A^2}} + B \ln \frac{R_{out} + \sqrt{R_{out}^2 + B^2}}{R_{in} + \sqrt{R_{in}^2 + B^2}}\right] \quad (12)$$

where $A = \frac{L}{2} - (z - d)$, $B = \frac{L}{2} + (z - d)$, and $\left(-d + \frac{L}{2}\right) < z < \left(d - \frac{L}{2}\right)$

R_{out} is the coil's outer radius, R_{in} is its inner radius, L is its thickness, I is the current flowing through it, N is how many turns there are, and μ_0 is the air's permittivity. The design and numerical simulation results of ring-shaped electromagnets based FFP spatial encoding is presented in Figure 6.

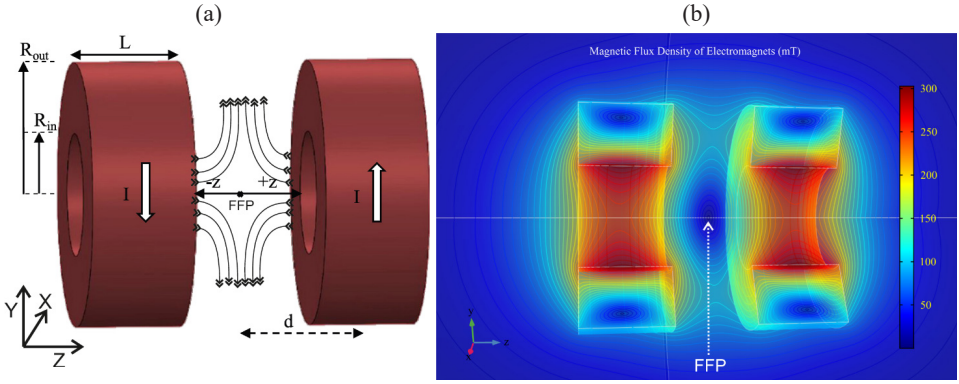

Figure 6. (a) Electromagnetic coils-based selection field design for the MPI scanner, (b) In COMSOL Multiphysics, a 2D axisymmetric numerical simulation of the configuration was conducted and demonstrates FFP at the midpoint [33,35].

DRIVE AND RECEIVE COILS

Dynamic magnetic fields are used to excite superparamagnetic iron oxides (SPIONs) at specific frequencies (e.g., 1-100 kHz) for magnetic particle imaging (MPI) applications [40]. These magnetic fields are implemented with different-shaped electromagnetic coils. Similarly, the non-linear response of the magnetic nanoparticles is detected with electromagnetic coils. However, alternating current at higher frequencies through a single copper wire causes high resistance as compared to direct current. The skin effect is a phenomenon that causes large power losses in driving coils and a poor SNR ratio. Both the driving and receiving coils use Litz wires to address these problems. The number of drive and receive coil pairs define the scanning dimensions of the MPI scanners. Usually, solenoid or Helmholtz coils are preferred to generate axial magnetic fields (for the x-axis). Rectangular, saddle, and fingerprint-shaped coils are utilized to generate transverse magnetic fields.

Drive and receive coils of the 1D-MPI scanner along the bore axis can be designed in a solenoid shape. The homogeneity of the magnetic fields has significant importance in MRI, however, it is less crucial in MPI. The optimum homogeneity of the solenoid coil [33] is achieved when its length is equal to 1.73 times its radius. The magnetic field of the coil is calculated with the following equation;

$$B(z) = \frac{\mu_0 NI}{2L(R_{out} - R_{in})}\left[A\ ln\frac{R_{out} + \sqrt{R_{out}^2 + A^2}}{R_{in} + \sqrt{R_{in}^2 + A^2}} + B\ ln\frac{R_{out} + \sqrt{R_{out}^2 + B^2}}{R_{in} + \sqrt{R_{in}^2 + B^2}}\right] \quad (13)$$

where $A = \frac{L}{2} - z,\ B = \frac{L}{2} + z$, and $-\frac{L}{2} < z < \frac{L}{2}$

L is the length of the solenoid coil. R_{in} and R_{out} are the inner and outer radii of the coil, respectively. N is the number of turns on a multi-layer solenoid coil. Numerical simulations were carried out in COMSOL to achieve optimum homogeneity. The drive and receive coils are designed in a cylindrical shape as shown in Figure 7.

The nonlinear response of the SPIONs is measured through the inductive method using a solenoid receive coil. However, the tracer response is a million times smaller than the fundamental harmonics of the excitation frequency. The induction of the first harmonic on the receive coil is known as the direct feedthrough phenomenon. There are two methods to eliminate the direct feedthrough effect. One is based on the geometric design of the receive coil which consists of three sections; the outer section winding is opposite the middle section. Another method is to integrate a band stop filter (BSF) to suppress the fundamental harmonics of the receive coil.

(a) (b)

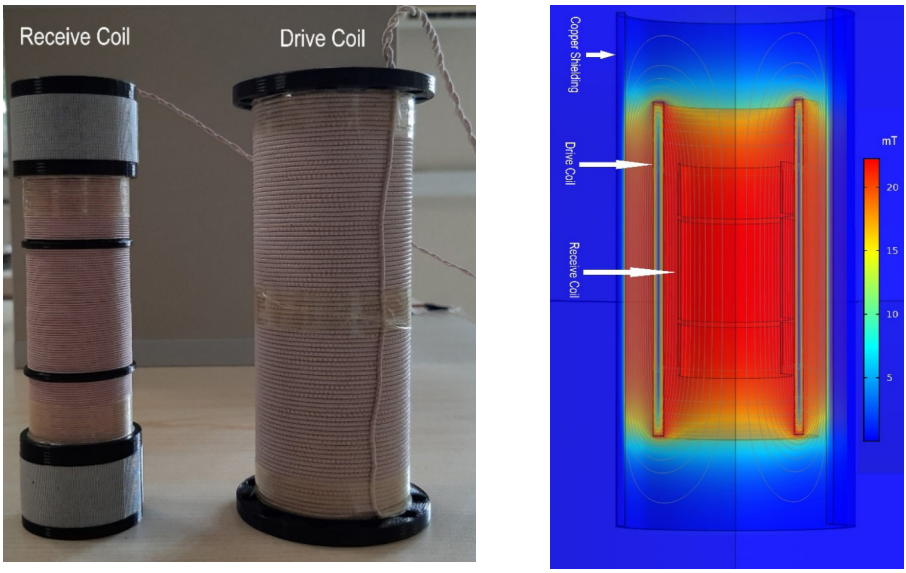

Figure 7. (a) The construction of solenoid drive and receive coils for 1D-MPI scanner [33,36] (b) The homogeneous magnetic flux density of the drive coil.

Sensitivities of Drive and Receive Coils

Magnetic flux density generated by the drive coil is directly controlled by electric current passing through it. A cylindrical copper shielding with a thickness of 3 mm was utilized to protect the drive and reception coils from the nonlinearities of the permanent magnets and environmental electromagnetic interferences. High-frequency magnetic fields are also restrained by shielding in a closed

space. Depending on the air gap between the drive coil and copper shielding, the placement of the drive coil inside the cylindric copper shield also decreased the coil's effectiveness. To measure the sensitivity of the electromagnetic coil, 1A (DC) current was applied and magnetic flux density was measured across the length of the coil. A minimum current is applied to avoid thermal heating at the coil. Numerical simulation was performed in COMSOL Multiphysics using its AC&DC model, and experimental data were recorded with a gauss meter and moving robot. The comparison of the numerical and experimental data for the drive coil sensitivity is shown in Figure 8(a).

The middle section is almost equal to the outer sections (left and right) of the receive coil. To measure the sensitivity of the coil, 1A (DC) was applied and measurements were taken with 1 mm resolution along the x-axis. Numerical simulation and experimental data were compared, and their results are presented in Figure 8(b). The magnetic flux density of 1.10 mT was measured at the center of the drive coil at 1A direct current. The numerical and experimental data are in good agreement in terms of field homogeneity and efficiency (mT/A).

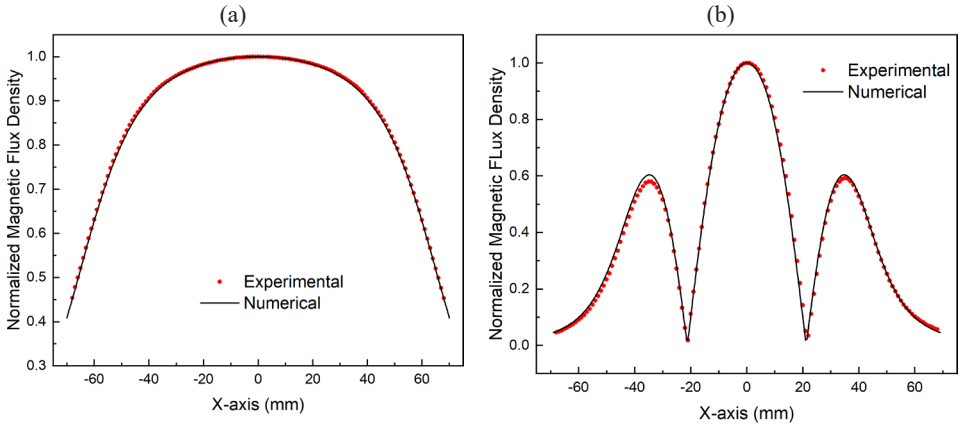

Figure 8. (a) Normalized magnetic flux density response of the drive coil at 1A direct current, (b) Normalized magnetic flux density response of the gradiometric receive coil at 1A direct current [33].

Field Free Point Movement

There is just one point where magnetic fields are zero as a result of the selection field. The FFP is moved non-mechanically by the superposition of an inhomogeneous selection field and a spatially homogeneous drive field. The FFP proceeds to the point where the drive and selection fields' magnitudes cancel each other out.

The drive field serves as both an excitation and driving field for the tracer agents (Perimag, Vivotrax, etc). Magnetic nanoparticles are excited at the excitation frequency by the sinusoidal form of the driving field. Inside the field of view (FOV), spatial information is provided by higher harmonics produced by the tracer material. It is possible to express the sinusoidal excitation field along the bore axis (x-axis) as;

$$B^D(t) = -A_x^D \cos(2\pi f^E t) e_x \tag{14}$$

At every spatiotemporal location, the superposition of the driving field and selection field can be represented as;

$$B_x(x,t) = -A_x^D \cos(2\pi f^E t) + G_x x \tag{15}$$

FFP linearly moves along the x-axis within $[\frac{-A_x^D}{G_x}, \frac{A_x^D}{G_x}]$ interval. The FFP moves at a maximum speed in the defined interval's midpoint and zero speed at its edges. This has an impact on the image quality as well, which is better towards the FOV's center. The movement of the FFP inside the FOV is shown in Figure 9. FFP is shown to move quickly at the center and slowly at the outside. The response on each side of the FFP is symmetric since the drive field is sinusoidal.

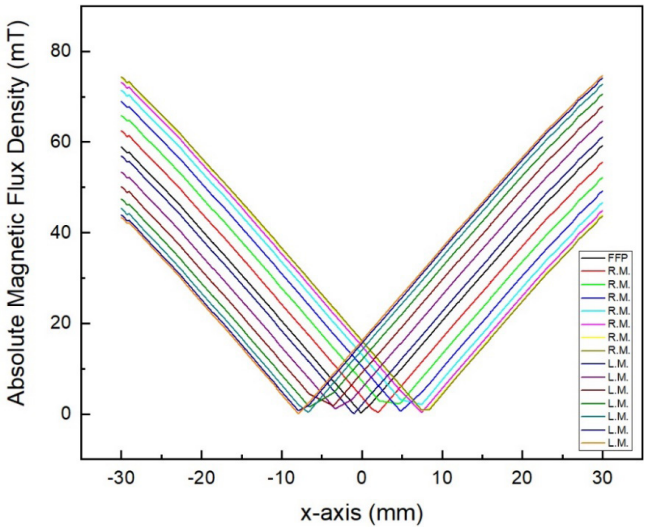

Figure 9. The selection field and the drive field's half-cycle (from the negative peak to the positive peak) are superimposed. Right moving is denoted by R.M., while left moving is denoted by L.M [33].

Signal Chain of MPI Scanners

The main components are the selection field, copper shielding, drive coil, receive coil, impedance matching circuit for the drive coil, and phantom setup. MATLAB-based control console (graphical user interface, GUI) can be used to operate and control MPI devices for imaging. The data acquisition card (DAQ) generates a sinusoidal signal, which is then amplified by a power amplifier (PA). SPIONs are scanned inside the field of view region of the MPI scanner. Before data recording by a DAQ device is performed for post-processing, the receive coil signal is processed through a low noise amplification (LNA). A general signal flow of MPI scanner is shown in Figure 10.

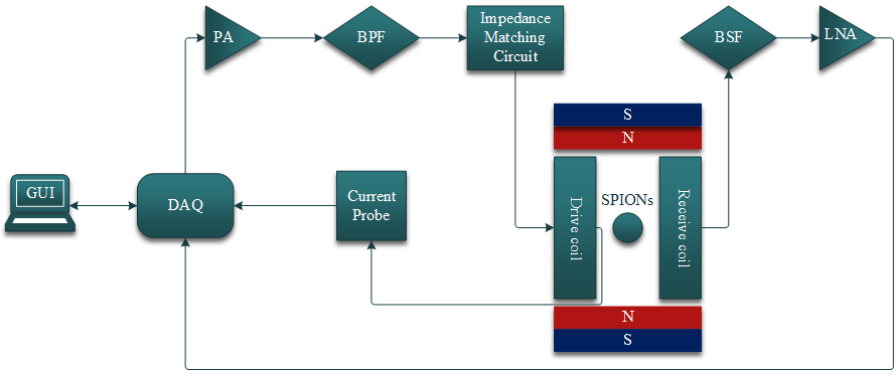

Figure 10. Generalized signal chain of MPI scanner [33,34]. The selection field is developed with permanent magnets. The drive and receive coils are implemented with co-axial solenoid coils. BPF demonstrate band pass filter and BSF demonstrate band stop filte**r.**

IMAGE RECONSTRUCTION

It is not possible to directly visualize an MPI signal without first converting the voltage signal to a particle concentration. The distinctive characteristics of post-processing technique includes image quality (resolution) and image scanning time. The fundamental presumption of the reconstruction methods applied to MPI systems is that there exists a linear relationship between recorded signal and particle concentration. Human tissues, bones, and other structures do not cause any signal generation in MPI. Due to inductive connection between the drive and receive coils, signals that are practically recorded without the placement of scanning objects (in-vivo, in-vitro sample, phantom) are referred to as background signals.

Two different techniques are used for MPI image reconstruction purposes. The system function (frequency-based) approach uses the higher harmonic response of the excitation field due to tracer material. The system function aims to establish the link between induced signals from SPIONs as a function of space (location dependent) [41]. The system function is calculated basically in two different ways: measurement-based, and model-based.

The second technique for image reconstruction of MPI is known as X-space (time-based). Instead of using frequency response, receive coil data is directly processed in the time domain. The linear and shift-invariant (LSI) feature of the recorded data is a key component of the X-space approach [42]. This approach works fine for rectangular trajectories, however, the Lissajous trajectory for three drive-receive channels is very challenging as fast scanning intervals violate the LSI property due to the relaxation behavior of the nanoparticles. A brief comparison of harmonic-space and X-space MPI imaging workflow is shown in Figure 11. MPI scanner with one drive-receive coil pair is considered enclosed in copper shielding. The selection field for FFP spatial encoding is represented with two pairs of NdFeB permanent magnets (N (north pole), S (south pole)). Although scanning procedures are different for both techniques, its scanner geometry is still identical.

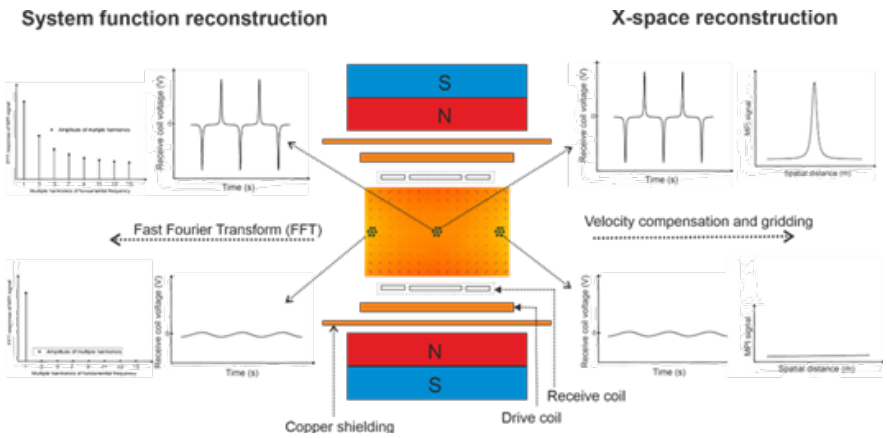

Figure 11. System function and X-space are fundamental image reconstruction methods for MPI. A simplified MPI scanner with one drive coil and one receive coil is demonstrated in the middle. System matrix utilizes the Fast Fourier Transform (FFT) of the particles' signal at each point in the field of view (FOV). However, X-space uses the same particle's signal for further processing. The tracer response becomes saturated at the outer edges of the FOV region which results in no MPI images [33,34].

X-space Reconstruction

The time-domain based X-space technique provides fast image reconstruction of the tracer agent concentrations. It is critical to highlight that the X-space technique's driving assumptions are applied field homogeneity and infinite rapid relaxation of the tracer agents. Initially, recorded signal is normalized with FFP movement. Finally, the griding of the MPI signal is carried out over the FFP scanning pattern.

The feedthrough effect at the excitation frequency is eliminated by the gradiometric design of the receive coils and band stop filter on the receive signal. Fortunately, the missing data simply introduces DC offset in the reconstructed signal, which can be recovered with continuity boundary conditions [42,43]. The receiving coil voltage was delayed compared to the excitation field by the magnetic nanoparticle's frequency-dependent relaxation behavior. In spatial mapping, relaxation-based delay causes the MPI signal to shift at the gridding stage [44]. Additionally, it is possible to model the relaxation behavior of the nanoparticles as an exponentially decaying function combined with the magnetization response of the magnetic nanoparticles [44]. Deconvolution techniques, such as Wiener filtering, can be used to remove blurring from the reconstructed image. The movement of the FFP can be mathematically expressed as based on equation (16);

$$x^{FFP}(t) = \frac{A_x^D}{G_x}\cos(2\pi f^E t) \tag{16}$$

FFP linearly moves along the x-axis over the line within $[\frac{-A_x^D}{G_x}, \frac{A_x^D}{G_x}]$ interval. Gx is gradient field strength along the x-axis, and Ax is the peak amplitude in the x-axis. The maximum limits of the FFP represent the FOV region along the x-axis. The velocity compensation of the received signal can be modeled as in equation (17);

$$u^N(t) := \frac{u^P(t)}{(B^D)'(t)} = (c * \acute{m})(\frac{B^D(t)}{G_x}) \tag{17}$$

where $\acute{m} := P^R m' G_x$

The spatial gridding of the particle signals can be performed with the coordinate transformation of the velocity compensated signals. The particle concentration across the FFP trajectory (instantaneous positions) can be expressed as;

$$u^x(x^{FFP}) = u^N(\frac{1}{2\pi f^E} cos^{-1}\left(\frac{G_x}{A_x^D} x^{FFP}\right) = (c * \acute{m}) x^{FFP} \tag{18}$$

Phantom Imaging

A single phantom of the Perimag sample was scanned as presented in the previous section inside FOV (-7 mm to 7 mm). A sinusoidal excitation field of 15 mT (peak amplitude) was generated from the drive coil. The phantom was attached to the 3D actuator and tracer agent induced signals were recorded with a step of 1 mm distance. Five lines were recorded for the Perimag sample and their MPI signals were presented in Figure 12(a). The recorded data of the 5 lines and 21 points on each line were mapped along the xz plane as shown in Figure 12(b). The spatial resolution of the MPI signal for the z=0 line was measured as 5.06 mm (FWHM). Phantom imaging of 40 µl in a diameter of 3.5 mm glass tube. Five lines were scanned along the z-axis (perpendicular to the bore axis). MPI signals for the z-axis were acquired by following the same procedure. The spatial resolution of the overall MPI signal is larger than the centered PSF (3.5 mm). This may be affected by the thick phantom of 4 mm in diameter. Theoretically, a single point source can be considered for imaging. However, an experimentally certain amount of the sample keeps significant area/volume which may affect spatial resolution. Therefore, phantoms made of Perimag SPIONs can be distinguished with a gap of 5 mm.

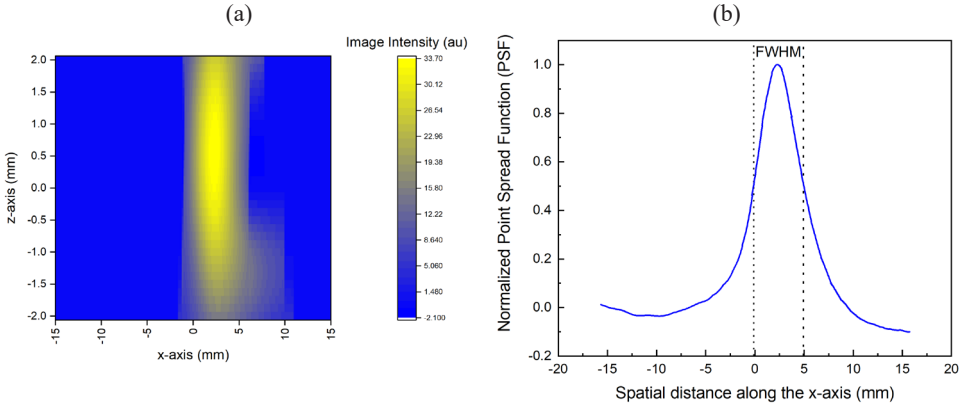

Figure 12. (a) MPI image of the Perimag tracer agent of 40 µl in a cylindrical phantom, (b) MPI signal of the Perimag sample at centered (z = 0) line [33,36].

APPLICATIONS OF MPI

Innovative biomedical applications are made possible by the real-time imaging capacity of the MPI approach with great spatial and temporal resolution. It does not include ionizing radiation and is free of iodine-based contrast agents. On the other hand, MPI employs SPIONs as tracer agents. Cell-based studies of tissue perfusion and stenosis are possible due to the MPI signal's quantitative relation with particle concentrations [45,39]. As demonstrated in Figure 13, MPI offers enormous potential for a variety of applications, including lung imaging, cancer imaging, vascular and perfusion imaging, and MPI-guided thermal therapy.

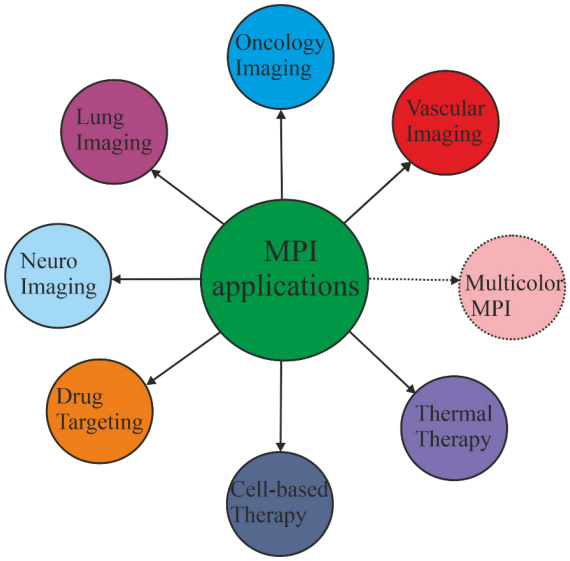

Figure 13. A brief review of intra-disciplinary biomedical applications of MPI [33,34]**.**

Excitation field and pickup systems, spatial encoding (FFP/FFL), image reconstruction, biomedical applications, tracer agents, and image reconstruction are all crucial components of the MPI methodology. Since its initial invention in 2005, the technical aspects of MPI such as gradient field, excitation fields, bore size, and pulse sequences have continuously improved. The research on scaling up the MPI technology is already in progress. Integration with other imaging modalities is inevitable since MPI lacks morphological characteristics. Few multimodal imaging methods, such MPI-CT and MPI-MRI, are thus also demonstrated at the pre-clinical level. Preliminary research in numerous domains including drug delivery, neuroimaging, cell tracking, cancer imaging, vascular imaging, functional imaging, and magnetic thermal therapy in MPI has produced outstanding results. Pre-clinical MPI scanners were successfully implemented, which raised high hopes for the pre-clinical (animal) to clinical (human) transition phase. The MPI is a remarkable imaging device with outstanding qualities that can be used as a diagnostic, drug administration, and monitoring device in medical imaging. With this groundbreaking imaging method for medical, cancer could be detected in its early stages.

REFERENCES

[1] Gleich, B., and J. Weizenecker, J. Tomographic Imaging using the Nonlinear Response of Magnetic Particles. Nature, 2005, 435:1214–17.

[2] Gleich, B. Principles and Applications of Magnetic Particle Imaging. Doctoral Thesis, University of Lübeck, 2013.

[3] Bauer, L.M. Magnetic Nanoparticle Characterization for Imaging and Therapeutic Applications. Doctoral Thesis, Case Western Reserve University, 2016.

[4] Bringout, G. Field Free Line Magnetic Particle Imaging Characterisation and Imaging Device Up-scaling. Doctoral Thesis, University of Lübeck, 2016.

[5] Pablico-Lansigan, M.H., Situ, S.F., Samia AC.S. Magnetic Particle Imaging: Advancements and Perspectives for Real-time in Vivo Monitoring and Image-guided Therapy. Nanoscale, 2013, 5:4040-4045.

[6] Massoud, T.F., Gambhir, S.S. Molecular Imaging in Living Subjects: Seeing Fundamental Biological Processes in a New Light. Genes and Development, 2003, 17:545–580.

[7] Weizenecker, J., Borgert, J., Gleich, B. A Simulation Study on the Resolution and Sensitivity of Magnetic Particle Imaging. Phys. Med. Biol., 2007, 52:6363-6374.

[8] Kherlopian, A.R., Song, T., Duan, Q., Neimark, M. A., Po, M.J., Gohagan, J.K., Laine, A.F. A Review of Imaging Techniques for Systems Biology. BMC Syst Biol., 2008, 2(74):18700030.

[9] Weissleder, R. Scaling Down Imaging: Molecular Mapping of Cancer in Mice. Nat Rev Cancer, 2002, 2:11–18.

[10] Cox, B., Beard, P. Imaging Techniques: Super-resolution Ultrasound. Nature, 2015, 527:451–452.

[11] Zheng, B., Vazin, T., Goodwill, P.W., Conway, A., Verma, A., Saritas, E.U. et al. Magnetic Particle Imaging Tracks the Long-term Fate of in Vivo Neural Cell Implants with High Image Contrast. Sci. Rep., 2015, 5:14055.

[12] Nguyen, P.K., Riegler, J., Wu, J.C. Stem Cell Imaging: from Bench to Bedside. Cell Stem Cell, 2014, 14:431–444.

[13] Zheng B., See, M.P.V., Yu, E., Gunel, B., Lu, K., Vazin, T. et al. Quantitative Magnetic Particle Imaging Monitors the Transplantation Biodistribution, and Clearance of Stem Cell In Vivo. Theranostics, 2016, 6:291–301.

[14] Weizenecker, J., Gleich, B., Rahmer, J., Dahnke, H., Borgert, J. Three-dimensional Real-time in Vivo Magnetic Particle Imaging. Phys. Med. Biol., 2009, 54: L1-L10.

[15] Knopp, T., Buzug, T.M. Magnetic Particle Imaging: An Introduction to Imaging Principles and Scanner Instrumentation. Springer Heidelberg New York Dordrecht London, 2012.

[16] Goodwill, P.W., Saritas, E.U., Croft, L.R., Kim, T.N., Krishnan, K.M., Schaffer, D.V., Conolly, S.M. X-space MPI: Magnetic Nanoparticles for Safe Medical Imaging. Adv. Mater., 2012, 24:3870-3877.

[17] Saritas, E.U., Good, P.W., Croft, L.R., Konkle, J.J., Lu, K., Zheng, B., Conolly, S.M. Magnetic Particle Imaging (MPI) for NMR and MRI Researchers. Journal of Magnetic Resonance, 2013, 229:116-126.

[18] Bauer, L.M., Situ, S.F., Griswold, M.A., Samia, A.C.S. Magnetic Particle Imaging Tracers: State-of-the-art and Future Directions. J. Phys. Chem. Lett., 2015, 6:2509–2517.

[19] Song, G., Chen, M., Zhang, Y., Cui, L., Qu, H., Zheng, X., Wintermak, M., Liu, Z., Rao, J. Janus Iron Oxides @ Semiconducting Polymer Nanoparticle Tracer for Cell Tracking by Magnetic Particle Imaging. Nano Lett., 2018, 18:182-189.

[20] Tay, Z.W., Chandrasekharan, P., Zhou, X.Y., Yu, E., Zheng, B., Conolly, S. In Vivo Tracking and Quantification of Inhaled Aerosol using Magnetic Particle Imaging towards Inhaled Therapeutic Monitoring. Theranostics, 2018, 8(13):3676-3687.

[21] Tay, Z.W., Chandrasekharan, P., Chiu-Lam, A., Hensley, D.W., Dhavalikar, R., Zhou, X.Y. et al. Magnetic Particle Imaging-guided Heating in Vivo using Gradient Fields for Arbitrary Localization of Magnetic Hyperthermia Therapy. ACS Nano, 2018, 12(4):3699–3713.

[22] Murase, K., Aoki, M., Banura, N., Nishimoto, K., Mimura, A., Kuboyabu, T., Yabata, I. Usefulness of Magnetic Particle Imaging for Predicting the Therapeutic Effect of Magnetic Hyperthermia. Open J. of Med. Imaging, 2015, 5(2):85-99.

[23] Lassenberger, A., Scheberl, A., Stadlbauer, A., Stiglbauer, A., Helbich, T., Reimhult, E. Individually Stabilized, Superparamagnetic Nanoparticles with Controlled Shell and Size Leading to Exceptional Stealth Properties and High Relaxivities. ACS Appl. Mater. Interfaces, 2017, 9 (4):3343–3353.

[24] Bae, K.H., Park, M., Do, M.J., Lee, N., Ryu, J.H., Kim, G. W. et al. Chitosan Oligosaccharide-stabilized Ferrimagnetic Iron Oxide Nanocubes for Magnetically Modulated Cancer Hyperthermia. ACS Nano, 2012, 6 (6):5266–5273.

[25] Kolen'Ko, Y.V., Banobre-Lopez, M., Rodriguez-Abreu, C., Carbo-Argibay, E., Sailsman, A., Pineiro-Redondo, Y. et al. Large-scale Synthesis of Colloidal Fe_3O_4 Nanoparticles Exhibiting High Heating Efficiency in Magnetic Hyperthermia. J. Phys. Chem. C, 2014, 118(16):8691–8701.

[26] Wang, Q., Chen, B., Cao, M., Sun, J., Wu, H., Zhao, P. et al. Response of MAPK Pathway to Iron Oxide Nanoparticles in Vitro Treatment Promotes Osteogenic Differentiation of HBMSCs. Biomaterials, 2016, 86:11–20.

[27] Son, B., Kim, H.D., Kim, M., Kim, J.A., Lee, J., Shen, H. et al. Physical Stimuli-induced Chondrogenic Differentiation of Mesenchymal Stem Cells using Magnetic Nanoparticles. Adv. Healthc. Mater., 2015, 4 (9):1339–1347.

[28] Huong, L.T.T., Nam, N.H., Doan, D.H., Nhung, H.T.M., Quang, B.T., Nam, P.H. et al. Folate Attached, Curcumin Loaded Fe_3O_4 Nanoparticles: A Novel Multifunctional Drug Delivery System for Cancer Treatment. Mater. Chem. Phys., 2016, 172:98–104.

[29] Zhang, D., Wang, J., Wang, Z., Wang, R., Song, L., Zhang, T. et al. Polyethyleneimine-coated Fe_3O_4 Nanoparticles for Efficient SIRNA Delivery to Human Mesenchymal Stem Cells Derived from Different Tissues. Sci. Adv. Mater., 2015, 7 (6):1058–1064.

[30] Lara, V.P., Caramelli, P., Teixeira, A.L., Barbosa, M.T., Carmona, K.C., Carvalho, M.G. et al. High Cortisol Levels are Associated with Cognitive Impairment No-dementia (CIND) and Dementia. Clin. Chim. Acta, 2013, 423:18–22.

[31] Kim, T., Momin, E., Choi, J., Yuan, K., Zaidi, H., Kim, J. et al. Mesoporous Silica-coated Hollow Manganese Oxide Nanoparticles as Positive T_1 Contrast Agents for Labeling and MRI Tracking of Adipose-derived Mesenchymal Stem Cells. J. Am. Chem. Soc., 2011, 133 (9):2955–2961.

[32] Palanisamy, S., Wang, Y.M. Superparamagnetic Iron Oxide Nanoparticulate System: Synthesis, Targeting, Drug Delivery and Therapy in Cancer. Dalt. Trans., 2019, 48 (26):9490–9515.

[33] Irfan, M. Design and Implementation of Magnetic Particle Imaging (MPI) Scanner for Medical Applications. Ph.D. dissertation, Dept. Electron. Eng., Gebze Tech. Univ., Gebze, Turkey, 2021.

[34] Irfan, M., Dogan, N. Comprehensive Evaluation of Magnetic Particle Imaging (MPI) Scanners for Biomedical Applications. IEEE Access, 2022, 10:86718-86732.

[35] Irfan, M., Dogan, O.M., Dogan, N., Bingolbali, A. Selection field Generation using Permanent Magnets and Electromagnets for a Magnetic Particle Imaging Scanner. Alexandria Engineering Journal, 2022, 61:7685-7696.

[36] Irfan, M., Dogan, N., Dogan, O.M., Bingolbali A. Development of Magnetic Particle Imaging (MPI) Scanner for Phantom Imaging of Tracer Agents. IEEE Transactions on Magnetics, 2022, 58:1-6.

[37] Cao, D., Li, H., Wang, X., Jing, P. et al. High Saturation Magnetization of γ-Fe2O3 Nanoparticles by a Facile One-step Synthesis Approach. Sci. Rep., 2016, 6, 32360.

[38] Chou, C.Y., Ferrage, F., Aubert, G., Sakellario, D. Simple Method for the Generation of Multiple Homogeneous Field Volumes inside the Bore of Superconducting Magnets. Sci Rep., 2015, 12200.

[39] Basharat, M., Ding, M., Cai, H., Li, Y., Fang, J. Design and Analysis of Multilayer Solenoid Coil for Faraday Modulator. In: MATEC Web of Conference, 2017, 114:1-9.

[40] Kuhlmann, C., Khandhar, A.P., Ferguson, R.M., Kemp, S., Wawrzik, T., Schilling, M. et al. Drive-field Frequency Dependent MPI Performance of Single-core Magnetic Nanoparticle Tracers. IEEE Trans. on Magnetics, 2015, 51(2):6500504.

[41] Rahmer, J., Weizenecker, J., Gleich, B., Borgert, J. Signal Encoding in Magnetic Particle Imaging: Properties of the System Function. BMC Med. Imaging, 2009, 9 (4):1–21.

[42] Lu, K., Goodwill, P.W., Saritas, E.U., Zheng, B., Conolly, S.M. Linearity and Shift Invariance for Quantitative Magnetic Particle Imaging. IEEE Trans. Med. Imaging, 2013, 32 (9):1565–1575.

[43] Lu, K., Goodwill, P.W., Zheng, B., Conolly, S. The Impact of Filtering Direct-feedthrough on the X-space Theory of Magnetic Particle Imaging. Medical Imaging: Biomedical Applications in Molecular, Structural, and Funcation Imaging, 2011, 79652I.

[44] Croft, L.R., Goodwill, P.W., Conolly, S.M. Relaxation in X-space Magnetic Particle Imaging. IEEE Trans. Med. Imaging, 2012, 31(12):2335-2342.

[45] Nikolo, M. Superconductivity: A Guide to Alternating Current Susceptibility Measurements and Alternating Current Susceptometer Design. Am. J. Phys., 1995, 63(1):57–65.

Chapter 2

IoT TECHNOLOGY AND ITS APPLICATIONS IN TURKEY

Fatma YAPRAKDAL[1], Onur AKTAS[2]

1 Kırklareli University, Engineering Faculty, Electrical and Electronics Engineering, Kırklareli, Türkiye
2 Kırklareli University, Graduate School of Science and Engineering, Electrical and Electronics Engineering, Kırklareli, Türkiye

INTRODUCTION

British researcher Kevin Ashton, who used the term IoT in 1999, is accepted as the father of the name by academics, researchers, and practitioners although there is no accepted general definition for the term IoT [1]. In its broadest definition, it is defined as a worldwide network created by uniquely addressed objects, and the objects in this network communicate with each other with a specific communication protocol [2].

Integrating IoT into renewable systems plays a key role in the optimization of energy use, energy transmission, and distribution [3]. Line failures can be prevented by estimating the maintenance times and component lifetimes of transformers, which are frequently used in transmission and distribution lines. In this way, the production continues uninterruptedly and the comfort of daily life can be maintained. As for the health sector, remote monitoring of patients, obtaining instantaneous physiological values and recording these values, making a diagnosis with the data obtained, many applications such as monitoring drug use and reporting allergic drugs to the patient have been carried out [4]. Image processing in the transportation industry, detecting driver fatigue with fuzzy logic and deep learning methods, fleet management, by adding innovations such as vehicle and driver tracking, supports many issues from unnecessary fuel consumption to the prevention of traffic accidents. It is seen that the studies carried out in the agriculture and livestock sector stand out compared to other fields. By monitoring the temperature and humidity of the soil and environment, the amount and quality of the product produced can be increased by automatic irrigation and monitoring processes. With the data taken from the soil, data about soil quality is collected and nutrient support processes can be kept at optimal values, thus preventing the accumulation of toxins in foods. Agricultural workers can control the designed system remotely and with weather data, the irrigation process is automatically postponed on days when rain is expected, and unnecessary use of water resources can be prevented. The widespread use of automatic irrigation systems transforms the agricultural sector into a dynamic and constantly developing technology area [5]. Early diagnosis of animal diseases, wildlife management and bee colony monitoring are IoT applications applied in the world in livestock applications. In the fields of smart homes and smart cities, IoT offers solutions to facilitate the life of elderly and disabled individuals. In addition, security and emergency notifications, regulation of ambient temperature and humidity, smart parking and traffic light systems are among the applications that make daily life easier [6]. In the Horizon Report published in 2017, it is thought that IoT will play an active role in efficiency and security in educational technologies within 2-3 years [7]. In studies in the field of education, applications such as applications made with smart phones-watches, wearable computer applications, and and increasing the focus level of students by controlling the physical characteristics of the classroom environment such as temperature and humidity are used.

Here, IoT applications for Turkey which is a developing country and a great candidate for IoT applications. The examined IoT applications have been categorized by sector and the technologies and application studies used in these application studies have been discussed in detail and their deficient and developed sides have been revealed. In the applications, the criteria by which hardware elements such as microprocessor and sensor are selected, software and cloud computing preferences are examined and presented to the researchers who will work. The remaining parts of the chapter are organized as follows: In section 2, the structure and layers of IoT technology are examined. In section 3, the historical development of IoT technology is briefly mentioned, and the expected situations today and in the future are emphasized. In section 4, the IoT technology reports and the location of Turkey are examined and the general situation in Turkey is compared with the world countries. Many different IoT application studies throughout Turkey, which have been obtained by a detailed literature review, are presented in section 5. In section 6, the chapter is concluded with a general evaluation.

IoT TECHNOLOGY AND STRUCTURE

In the most general definition, IoT creates a large ecosystem and there are three basic components in this ecosystem. These are devices, communication protocols and cloud structures where the obtained data is stored. The constant increase in the amount of data that needs to be stored also encourages continuous development in cloud technology. The smart devices can collect instant data from the environment with the help of their sensors and communicate with other devices with their communication unit. The last component of a smart device consisting of three main parts is microprocessors such as Raspberry and Arduino The last component, which has a very important place in this ecosystem, is the communication protocols, which can also be defined as web services, which enable the device to transfer data to the cloud environment and communicate with each other. There is no generally accepted architectural structure for IoT yet. In the ongoing process, a five-layer architecture has been proposed in order to contribute to the data storage and general security problems of the four-layer architecture. “Figure 1”, shows the IoT architecture layers.

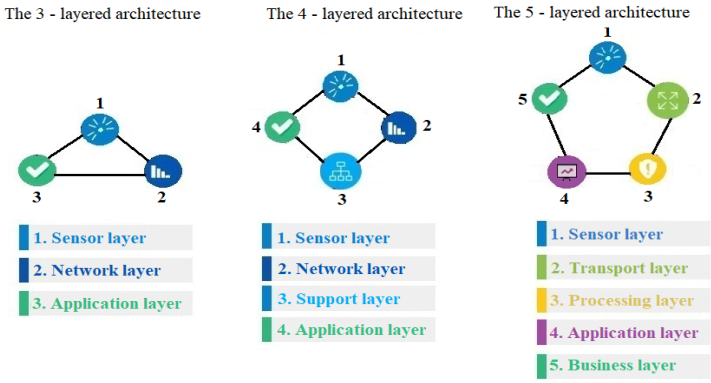

Figure 1. IoT architecture structures

Sensor Layer; captures data that can be perceived from the environment such as vibration, pressure, humidity, temperature, pulse rate, and respiration can be called the sensor layer. The sensors to be used are decisive in the operating conditions of the IoT device. *Network Layer*; is responsible for transferring the data collected from the sensors to the application layer without any processing. Here, the data received from the environment is converted into analog and digital signals. RFID, Zigbee, IEEE 802.15.4, Z-Wave, LTE, LoRa, NFC, and M2M communication protocols are included here. *Application Layer*; is the layer responsible for presenting the features expected from the device to the user. The operation of the device is provided from this layer. *Support Layer*; enables the data collected at the sensor layer to be processed through a number of processes before being sent to the network layer and the application layer, it is the layer that is basically created for security reasons, that analyzes and stores data. *Transport Layer*; is the layer between the processing and sensor layers in a 5-layer architecture. It undertakes the task of communication between the two layers. *Processing Layer*; is the layer that is added to clean up the unnecessary heaps by processing the data transmitted from the transport layer.

IoT APPLICATIONS DEVELOPMENT PERIOD

In the last twenty years, the increase in internet technology and the widespread use of IoT in the commercial field have supported the development of this technology. Although it has been twenty years since its first applications, it is seen as a technology that will shape the future with an increasing interest in recent years. The term “Internet of Things” was used for the first time in 1999 and the International Telecommunication Union presented its first IoT report in 2005 [8]. In the coming years, it is thought that paper documents, furniture, and even food will be connected to the network like other electronic devices [9]. Cisco’s report published in 2015, whose work is followed by researchers and practitioners of IoT technology, stated that the human population living on earth will be 7 billion people and the number of connected objects will be 50 billion in 2020. By 2022, it is seen that the world population is 7 billion 962 million [10]. It turns out that the number

of devices connected to the Internet is very close to the predicted target and has an increasing momentum.

IoT TECHNOLOGY APPLICATIONS REPORTS AND CURRENT STATUS OF TURKEY

A research website announced its report published in 2020 and this report has been carried out on approximately 1400 implemented projects in transportation, energy, and retail sales apart from industry [11]. In another report presented by The FT Omdia Digital Economic Index in September 2022, 51 countries are ranked according to 5 different technology areas and 16 digital economic criteria [12]. According to this report, China ranks first in the digital economy size and digital market size ranking in the field of IoT & Devices in 2022, with 17.6 points. It is followed by India with 8.8 points in second place and the top five countries are ranked as the USA, Indonesia, and Japan. In this ranking, Turkey is in 20th place with 2.1 points. On the same scale, it is predicted that in 2026, China, India, USA, and Indonesia will maintain their place, Brazil will take fifth place, and Turkey will move to 17th place by jumping 3 places. In the total scoring of the five selected technological fields, China ranks first with 85.22 points, while Turkey ranks 22nd with 13.24 points. It is seen that developed countries among the world states, have high economic power and have a scientific and technological say over other states that are investing in this technology, which are still in their infancy. The directly proportional effect of the digital economy on sustainable development becomes meaningful at this point and its importance emerges. In this respect, the studies of practitioners and researchers on IoT will support Turkey to rise to the top on a global scale.

IoT APPLICATIONS IN TURKEY

The literature study shows that there are many research studies in the field of IoT. However, the rapid development of this technology, the fact that it takes place more and more in daily life, and the increase in expectations in parallel with this have been the starting point for this chapter. It was built in Turkey in order to bring a solution to a certain problem within the scope of internet of things technology. Studies in the academic field of design are grouped under seven different sectors in total, including agriculture-livestock, education, smart cities, smart homes, industry, transportation, and health. In the following tables these studies are l”isted according to years.

Table 1. IoT application in Turkey – Farming and agriculture

Ref.	Hardware and Software Used	The Aim of the Study	Results of the Study
[13]	ESP 8266, Arduino Uno, LM 35 temperature sensor, LM 393 fire sensor, HL 69 humidity sensor	Developing a soil maintenance system to increase productivity in irrigation and fertilization systems.	Thanks to the sensors used in the created model, continuous data flow is provided from the soil, and in case of differences from the determined optimum values, the soil is fed automatically. With the ESP8266 Wi-Fi module, the sensor data is sent to the Cayenne cloud system, allowing the user to monitor data instantly.
[14]	Raspberry Pi 3, DHT 11 temperature and humidity sensor, BMP 180 Pressure sensor, 5 V Rain sensor, wind direction sensor, HMC5883L Compass sensor	To follow the changes in the weather conditions in a certain region with an IoT-based system.	With the designed station, the weather conditions are followed and at the same time, weather forecasts are made with the sensors used. It is also designed as a mobile platform so that the system can be used in different regions. In the test studies, it is stated that values such as wind direction, pressure, and temperature are consistent, but there are deviations in humidity and wind speed values.
[15]	Arduino Uno, ESP 8266, DHT22 temperature and humidity sensor, HL69 humidity sensor, Grove – UV sensor	More efficient operation and optimal use of resources by intelligently managing irrigation systems.	The data collected through the sensors in the system are compiled with the Arduino microcontroller and saved to the cloud, and instant user control and monitoring are provided via ThinSpeak. As a result of the study, it is stated that the humidity values work inversely with the temperature and UV radiation, and are directly proportional to the rain sensor.
[16]	Raspberry Pi 2, ESP 8266, Solenoid Valve, YL – 69 humidity sensor	To reduce the damage caused by heavy metals accumulating in the soil to humans and the environment in case of efficient use of water resources and fertilizing plants more than needed.	Soil demands are entered as input to the system and the data from the humidity sensor is used. Periodic irrigation and fertilization are carried out in line with the data obtained. With IoT technology, irrigation, soil moisture status, and soil analysis can be followed.
[17]	Raspberry Pi 3, Raspberry pi V2, ESP 8266, FC 28 soil moisture sensor, MQ-7 gas sensor, LDR, DHT 11 Temperature and humidity sensor	To be able to record the changes in climatic values in greenhouses where controlled crops are grown and to monitor them remotely.	Values such as indoor-outdoor temperature and humidity values, soil moisture, air quality, and light level obtained through sensors in the system are recorded and instantaneous monitoring is made possible. In addition, if the threshold values specified by the user are exceeded, the user is notified via SMS and e-mail.

[18]	Arduino Uno, Esp8266, SEN 13322Soil Moisture sensor	To assist the user in the amount of water required by different agricultural products and to control the irrigation process with remote access.	At the interface used in the created system, a list of plants whose humidity and temperature threshold values are processed into the database is created, and irrigation operations are carried out by comparison method after planting the selected plant.
[19]	Temperature and Humidity sensor, Acceleration Sensor, pressure sensor, Light Sensor	To be able to remotely monitor especially elderly agricultural workers working in open fields.	With the prototype produced, it can be monitored by elderly agricultural workers, their children, or their relatives. In this way, in the event of an accident (falling from a height, fainting, being beaten, etc.), it is ensured to reach the scene quickly.
[20]	Arduino Mega, SI7021 temperature-humidity sensor, Raspberry Pi	Monitoring indoor climate data and controlling ventilation, irrigation, and heating systems.	The data received from the sensors can be processed and monitored instantly. It is stated that the designed system can expand the use of technology in small businesses, especially since it has a modular structure.
[21]	Raspberry Pi 2, DS18 B20 Temperature Sensor	To be able to instantly monitor the air, soil, and water temperatures in the greenhouse.	A prototype has been realized that transfers the data taken from the sensors used for temperature measurement to the web environment. Thanks to the embedded web server in the nodes, it is advantageous to be used without an internet connection.
[22]	Raspberry Pi 2, DS18 B20 Temperature Sensor	To be able to instantly monitor the air, soil, and water temperatures in the greenhouse.	A prototype has been realized that transfers the data taken from the sensors used for temperature measurement to the web environment. Thanks to the embedded web server in the nodes, it is advantageous to be used without an internet connection.

Table 2. IoT application in Turkey – Education

Ref.	Hardware and Software Used	The Aim of the Study	Results of the Study
[23]	HM11 BLE Beacon module (Beacon), MIT App Inverter, Firebase cloud platform	To be able to instantly follow the duration of school bus vehicles, and therefore students, on the road.	From the moment students get on the bus (thanks to the pointer they carry with them), taking into account the location and time information, when the student gets on and off the bus and whether he is on the bus or not can be tracked instantly via the MIT App Invertor-based mobile application.
[24]	HM11 BLE Beacon module (Beacon), MIT App Inverter, Firebase cloud platform	To be able to instantly follow the duration of school bus vehicles, and therefore students, on the road.	From the moment students get on the bus (thanks to the pointer they carry with them), taking into account the location and time information, when the student gets on and off the bus and whether he is on the bus or not can be tracked instantly via the MIT App Invertor-based mobile application.
[25]	Arduino Uno Raspberry Pi Fingerprint Sensor RFID Card	Realizing Smart Classroom and Student Tracking System Design with the Internet of Things	The study was carried out in two parts Smart Classroom and Student Tracking System. In the smart classroom application, the control of the values such as the door and lighting of the classroom and the temperature, and in the student tracking system, the attendance of the students with a card or fingerprint was carried out.

Table 3. IoT application in Turkey – Smart homes

Ref.	Hardware and Software Used	The Aim of the Study	Results of the Study
[26]	Arduino Uno, esp 8266, DHT11 Temperature and humidity sensor, MQ2 Gas sensor, HC-SR501 Motion sensor, MongoDb database	To be able to design an IoT-based smart home system that reduces the human factor and increases energy, security,	In the study, IoT applications were carried out on the model house. The ventilation and lighting systems in the house can be controlled remotely and the data received from various sensors can be followed instantly with the developed mobile application. Theft, fire, etc. In such cases, a notification is sent to the landlord by e-mail. In addition, sensor data can be presented graphically within the entered date range.
[27]	Raspberry Pi PHP Web service	To realize an IoT-based door lock design in the Smart Home field.	Someone outside the house (child, caregiver) requests the owner to open the door with the mobile Android application. Then, the door image is sent to the host via Raspberry pi via e-mail, and the host can approve the opening of the door via the Android application.
[28]	ESP8266, MQ-4 gas sensor, 5V relay	Realizing an IoT-based smart socket design.	In the study, a smart socket design was carried out with a 3D printer. Gas MQ4, which is located on the prototype, constantly monitors the gas level. It sends a warning notification when a certain level is exceeded
[29]	Raspberry Pi, Pi Camera, ultrasonic range sensor, DHT11 Temperature-Humidity sensor	Designing an IoT-based refrigerator.	The system can monitor instantaneously the temperature-humidity data, whether the cooling continues or not, and whether the refrigerator door is open or closed.

Table 4. IoT application in Turkey – Smart cities

Ref.	Hardware and Software Used	The Aim of the Study	Results of the Study
[30]	ESP8266, DHT 11 sıcaklık-nem duyargası, ThinSpeak, Arduino Uno	System design that performs IoT-based data collection and sharing operations.	In the study, humidity and temperature data in a certain environment were collected via sensors, and the data was shared on the social media platform Twitter. In addition, when the specified limit values are exceeded, a notification is sent via the mobile application.
[31]	Arduino Mega, ESP 8266, infrared sensor, Servo-motor, 16x2 LCD Display	To solve the problem of car parking by developing an IoT-based parking system	Drivers can see whether there is an empty parking space via a mobile application and can make a reservation if there is no space. It is thought that the system will also benefit problems such as traffic congestion and fuel costs.
[32]	Arduino Uno, Geared DC Motor, Eplan Electric P8 program, wifi module	To realize IoT-based vehicle entry and exit control system design.	In the study, a barrier system using electric motors instead of the pneumatic supported bollards actively used in the market was developed and in addition to this, the internet of objects technology was applied to the barrier system, and the system was remotely controlled.

[33]	Raspberry Pi, Mifare card reader, MIT Appinverter	Performing IoT-based bus stop design.	In the study, a stop system is presented as an alternative to the stops that allow unilateral communication, which is currently in use. The travel information of the passengers waiting at the bus stop is obtained and the buses that are not waiting for the passengers are prevented from entering the stops unnecessarily.

Table 5. IoT application in Turkey – Transport/Healt

Ref.	**Hardware and Software Used**	**The Aim of the Study**	**Results of the Study**
[34]	The microcontroller and sensor model information used is not shared.	To design a system for tracking IoT-based convoy vehicles.	In the study, the problem for the services belonging to the transportation architecture, convoy vehicles has been expanded, and the node service definition has been added to the existing architecture.
[35]	The microcontroller and sensor model information used is not shared.	Realization of IoT-based driver fatigue detection system.	In the study, driver fatigue is determined by processing the images from the mobile device camera. If fatigue is detected with the processed images, a notification message is sent to the server via the mobile application. It is reported that the developed model has 95.65% accuracy and 95.86% accuracy rates and has better data than previous studies.
[36]	Raspberry Pi Unspecified	To design a system that enables remote monitoring of IoT-based medical device data.	In the study, a solution was presented to the problem that the measurements of laser devices used in the field of dermatology are made instantly with IoT, but the need for preprocessing due to the size of the data available. Thanks to the prototype created, the data collected from the device can be evaluated and an early maintenance message can be sent to the user.
[37]	pulse oximeter Android-based mobile smartphone	Developing an IoT-based remote patient monitoring system.	In the study, a system that works according to the data of oxygen saturation and pulse values, which can help physicians especially in diagnosing sleep apnea, was developed and compared with the data set used in the literature.

Table 6. IoT application in Turkey – Industry

Ref.	Hardware and Software Used	The Aim of the Study	Results of the Study
[38]	Delta DVP-12se PLC, 50/5 A current transformer, Raspberry pi3, Microsoft Azure	Monitoring of generators located in remote and difficult areas.	Conditions such as water-oil pressure and temperatures of the generator, connected to the system, instant mains-generator voltages and produced power values, operation, and air temperature can be monitored.
[39]	DHT 11 temperature sensor, heart rate sensor, GPS module ESP8266, LDR	To design an IoT-based wearable system for soldiers.	The instantaneous pulse rate of a soldier in the field, the humidity, temperature, and brightness of the environment can be followed instantly. In addition, location information can be tracked with the GPS module used.
[40]	Arduino Uno ESP8266, DHT-11 heat and humidity, Magnetic field, LDR, gas sensors	To be able to control the optimum parameters determined in the field of OHS in an industrial production enterprise.	The data received from the sensors used in the developed model can be monitored and recorded instantly via thing speak. In addition, the system can give an audible warning in case the determined optimum values are exceeded.
[41]	Raspberry Pi, BME680 multisensor, gas sensor, fire detection sensor	Realization of IoT-based smart factory management information system design.	In the study, values such as humidity, temperature, and pressure are obtained from the bme680 sensor. The data received together with the fire detection and gas sensors used in the system are collected with the firebase database and can be monitored instantly and graphically via the mobile application.

Table 7. IoT application in Turkey – Energy

Ref.	Hardware and Software Used	The Aim of the Study	Results of the Study
[42]	Arduino Uno, ESP 8266, DHT11 Temperature and Humidity sensor, LM 35 temperature sensor, TA12-200 current transformer, Ubidots cloud computing	Design of an IoT-based substation modeling.	In the study, a 50VA transformer model was created and the transformer was loaded with 40% - 80% - 120% load and data were obtained. The current and temperature values obtained at each load level are transferred to the cloud system and monitored as a blank. It is stated that it is an alternative to the widely used SCADA systems.
[43]	Arduino Mega, DHT22 Temperature and Humidity Sensor, MQ-135 Gas Sensor, LDR, VTB30-200 voltage transformer, ESP8266	Realization of system design that collects remote environment data for transformers.	Transformer data is collected by temperature, humidity, light, and gas sensors and transferred to the cloud environment. The collected data can be followed instantly and this data set is created. The obtained data set can be processed with artificial learning algorithms and fault prediction, remaining life estimation, and predictive maintenance suggestions can be presented.
[44]	ESP8266, Arduino Idea, The sensor models used are not specified.	To realize the design of the IoT-based transformer monitoring system.	In the study, the instantaneous control and intervention of important values such as high voltage situations, high temperature, high current, overload, and oil level is provided with IoT. In addition, the scenario of switching on and off the street lamps according to the sundial was added to the system. It is stated that it is an alternative to the widely used SCADA systems.

In the studies examined, it is seen that there are differences in hardware sensor selections and microprocessors according to the problem to be solved and the purpose of the subject in an IoT-based application. While pulse, acceleration, and temperature sensors are prominent in the health sector, gas, temperature, motion, and smoke sensors are frequently used in smart home applications. Raspberry and Arduino's microprocessors come to the fore in the microprocessor preference of the researchers. Since Raspberry Pi has higher processing power than Arduino, it is preferred in wide-ranging applications. While programming types such as Phyton, Java, and C/C++ can be used with Raspberry Pi, which operates as a Linux-based mini-computer, Arduino is programmed in C-based languages. Technologies such as RFID, LoRa, Z-Wave, LTE, and NFC are generally preferred as communication technology.

It is seen that Z-Wave, a low-power wireless protocol, is generally used in smart home applications and small commercial areas. RFID is one of the most frequently used communication technologies in IoT applications. It usually consists of a tag and a reader. Labels are applied to objects by addressing and data is transferred by radiofrequency electromagnetic fields. Labels containing data stored with their

electronic code are read when they come near the reader [48]. LoRa protocol is generally used in rural and remote areas, in applications such as chain management, intercontinental logistics, and mining.

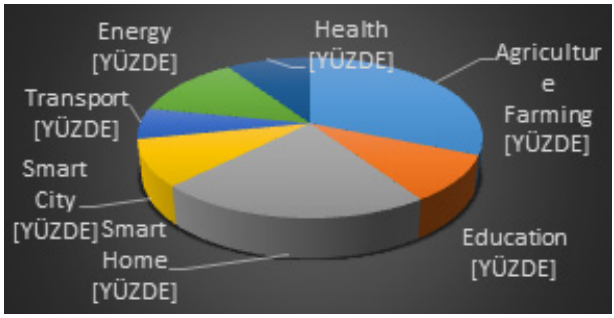

Figure 3. Graphical representation of examined IoT application studies on the sectoral basis

The ratio of each area where IoT technology is applied, in which the examined studies are carried out, within all sectors is presented in "Fig 5". Among the studies conducted here, it is seen that the studies carried out in the agriculture and livestock sectors have the highest rate with 31%, followed by the studies in the field of smart home with a high rate of 22%. While the IoT technology application rates of energy, education, health, and smart cities are around 10%, the rates of transportation have the lowest share with 6%.

CONCLUSION

In this study, academic studies conducted in Turkey in the field of internet of things technology were examined. This technology, which is estimated to create a technological revolution, continues to grow rapidly day by day with the motto "anytime from anywhere to any object". Although there are hesitations due to cyber security vulnerabilities, it is thought that its use will become more common with the emergence of new protocols and network technologies.

When we look at the internet-based studies in our country, the agriculture and livestock sectors are more common compared to the others. Considering that the contribution of the agricultural sector to the country's economy is around 40%, it is of great importance that young agriculture and livestock workers can continue to work in this sector, which requires intensive labor. As a solution to this, it is necessary to increase the living standards and incomes of the employees by applying the "internet of things technology" in the sector in a cheaper, safe, and more effective way. The fact that the intensity of the studies examined in this sector is taking the lead is considered to be positive for the future of the sector.

Secondly, with a rate of %22, smart home applications are seen as technologies integrated with the Internet of Things to increase the comfort of life in all environments. In our country, IoT devices produced based on various scenarios have started to appear in the market. It is thought that increasing the studies in

this field will contribute to the country's economy if energy efficiency is taken into account, as well as increase the comfort of the environment. In addition, it is thought that increasing the studies to be done in the health, transportation, energy, and retail sectors together with the studies already done for smart homes will accelerate the way to "smart cities".

In addition to the ever-increasing energy need, IoT-based technological devices accelerate this increase. Every technological device offered in all sectors also increases the need for energy as a consumer. Turkey is preparing to launch a new electric vehicle into the automobile market. Electric vehicles emerging with the rapidly growing industry are also expected to cause a large increase in energy consumption and force grid capacities in the long run. In this context, a reliable network structure will be needed to overcome the problems that may arise [49].

In addition to being an environmentally friendly technology, smart grids play an active role in fixed and mobile energy storage and distributed renewable energy sources [50]. With the smart grid studies to be carried out by analyzing the production and consumption data, energy supply and demand will be balanced and the storage systems will be more active and energy problems will probably be prevented.

Due to the virus epidemic that emerged in the past years and its ongoing effects, there have been worldwide disruptions in the field of traditional education. In similar situations, it is necessary to integrate new technologies into this field in order to continue education uninterruptedly and continuously. It is thought that internet-based studies will increase interaction in the field of education and support mastery of learning situations. In addition, with smart classroom environments to be made similar to smart home studies, the features of the environment such as temperature, humidity and lighting will be kept under control and will help students and teachers continue their educational activities in healthy and comfortable classroom environments.

REFERENCES

[1] J. López-De-Armentia, D. Casado-Mansilla, and D. López-De-Ipiña, "Fighting against vampire appliances through eco-aware things," in Proceedings - 6th International Conference on Innovative Mobile and Internet Services in Ubiquitous Computing, IMIS 2012, 2012, pp. 868–873. doi: 10.1109/IMIS.2012.112.

[2] M. Z. Gündüz and R. Daş, "Internet of things (IoT): Evolution, components and applications fields," Pamukkale University Journal of Engineering Sciences, vol. 24, no. 2, pp. 327–335, 2018, doi: 10.5505/pajes.2017.89106.

[3] N. H. Motlagh, M. Mohammadrezaei, J. Hunt, and B. Zakeri, "Internet of things (IoT) and the energy sector," Energies, vol. 13, no. 2. MDPI AG, 2020. doi: 10.3390/en13020494.

[4] Aktaş, F. , Çeken, C. & Erdemli, Y. E. Nesnelerin İnterneti Teknolojisinin Biyomedikal Alanındaki Uygulamaları . Düzce Üniversitesi Bilim ve Teknoloji Dergisi , 4 (1) (2016), 37-54 .

[5] E. Lichtenberg, J. Majsztrik, and M. Saavoss, "Profitability of Sensor-based Irrigation in Greenhouse and Nursery Crops." Dec 2013, DOI:10.21273/HORTTECH.23.6.770

[6] G. Demiris et al., "Older adults' attitudes towards and perceptions of 'smart home' technologies: A pilot study," Med Inform Internet Med, vol. 29, no. 2, pp. 87–94, Jun. 2004, doi: 10.1080/14639230410001684387.

[7] S. , C. M. , D. A. , F. A. , H. G. C. , and A. Adams Becker, "NMC Horizon Report: 2017 Higher Education Edition," Austin, Texas, 2017.

[8] D. Mondal, "The Internet of Thing (IOT) and Industrial Automation: a future perspective Power System and PID Controller Parameters via SCA algorithm View project Application of nonlinear control on Power system stability Improvement View project The internet of thing (IOT) and industrial automation: a future perspective," 2019. [Online]. Available: www.rcciit.org,

[9] M. Centenaro, L. Vangelista, A. Zanella, and M. Zorzi, "Long-range communications in unlicensed bands: the rising stars in the IoT and smart city scenarios," IEEE Wirel Commun, vol. 23, no. 5, pp. 60–67, Oct. 2016, doi: 10.1109/MWC.2016.7721743.

[10] https://www.cisco.com/c/en/us/solutions/collatera l/executive-perspectives/annual-internet-report/white-paper-c11-741490.html, "Cisco Annual Internet Report (2018–2023) White Paper," Mar. 09, 2020.

[11] IoT Analytics Market Insıght for The Internet of Things, "IoT Platforms Company Landscape 2020" Hamburg Germany, Dec. 2019.

[12] https://omdia.tech.informa.com/OM021617/FT-Omdia-Digital-Economies-Index-202226, "FT Omdia Dijital Ekonomiler Endeksi 2022–26," Sep. 19, 2022.

[13] Yenikaya, Muhammed Akif, Erdal Güvenoğlu, And Süleyman Kondakci. "Nesnelerin İnterneti (IoT) Tabanlı Akıllı Sulama ve Gübreleme Sistemi." Türkiye Bilişim Vakfı Bilgisayar Bilimleri ve Mühendisliği Dergisi 15.1 (2022): 14-23.

[14] Üçgün, Hakan, Zeynep Kübra Kaplan, and Uğur Yüzgeç. «Akıllı Hava İstasyonu ile IoT Tabanlı Hava Durumu İzleme Sistemi.» Avrupa Bilim ve Teknoloji Dergisi 23 (2021): 563-571.

[15] Babayiğit, Bilal, And Belkıs Büyükpatpat. "Nesnelerin İnterneti Tabanlı Sulama ve Uzaktan İzleme Sisteminin Tasarımı ve Gerçekleştirimi." Türkiye Bilişim Vakfı Bilgisayar Bilimleri ve Mühendisliği Dergisi 12.2 (2019): 13-19.

[16] Gücük, Murat. Hassas tarım uygulamalarında nesnelerin interneti teknolojilerinin kullanımı. MS thesis. Sakarya Üniversitesi, 2019.

[17] Baysal, Kenan, et al. "Nesnelerin İnterneti Tabanli Bir Sera Takip Sistemi." Ejovoc (Electronic Journal of Vocational Colleges) 8.2 (2018): 49-56.

[18] Taşkesen, Meryem. Wi-Fi ve nesnelerin interneti teknolojileri kullanılarak güncel hava durumu verileri ile tarla sulama sisteminin gerçekleştirilmesi. MS thesis. Kırıkkale Üniversitesi, 2018.

[19] Çakmak, Bülent, And Emrah Mercan. «Tarimsal Üretimde Örnek Bir IoT Uygulamasi Ve Yaşli Tarim Çalişanlarinin İzlenebilirliği.» Yaşlı Sorunları Araştırma Dergisi 10.1 (2017): 29-42.

[20] Çaylı, Ali, et al. «Sera çevre koşullarının nesnelerin interneti tabanlı izleme ve analiz sistemi ile denetlenmesi.» (2017).

[21] Türker, Ufuk, Uğur. Furkan, And Mehmet Ali Dayioğlu. "Seralarda Nesnelerin İnterneti Teknolojisinin Uygulanması: Tasarım ve Prototip Geliştirme." Gaziosmanpaşa Üniversitesi Ziraat Fakültesi Dergisi 33.Ek Sayı (2016): 52-60.

[22] M. et al. Abdel-Basset, "Internet of things in smart education environment: Supportive framework in the decision-making process.," Concurr Comput, Oct. 2019.

[23] Tamer, Murat Adnan. Mesleki Eğitimde Teknolojiye Bağlı Yeterliliklerin Geliştirilmesinde Nesnelerin Interneti (IoT) Eğitimi. Diss. Marmara Universitesi (Turkey), 2021.

[24] Küçük, Kerem, Buse Çelik, And Cüneyt Bayilmiş. "Nesnelerin İnterneti Teknolojileri ile Gerçek Zamanlı Okul Servisi ve Öğrenci Takip Sistemi Tasarımı." Düzce Üniversitesi Bilim ve Teknoloji Dergisi 6.4 (2018): 1211-1223.

[25] Ayşegül, Uçar, And Melih Hilmi Uludağ. "Nesnelerin İnterneti (IoT) ile akıllı sınıf ve öğrenci takip sistemi tasarımı." Dicle Üniversitesi Mühendislik Fakültesi Mühendislik Dergisi 9.2 (2018): 591-600.

[26] Erzi, Haki Mehmet. "Nesnelerin interneti teknolojisi ile akıllı ev kontrolü için uygulama geliştirilmesi." (2021).

[27] Kalyoncu, Ayşegül, and Metin Turan. "IoT teknolojisi kullanan pratik ve güvenilir akıllı kapı kilidi tasarımı." Avrupa Bilim ve Teknoloji Dergisi 36 (2020): 316-316.

[28] Ayyildiz, Mustafa, and Mustafa Denizli. "Nesnelerin İnterneti ile Akıllı bir Priz Prototipi." Düzce Üniversitesi Bilim ve Teknoloji Dergisi 7.1 (2019): 722-728.

[29] Şimşek, Muhammet Sait. IOT teknolojisinin buzdolabı üzerinde uygulanması. MS thesis. Konya Teknik Üniversitesi, 2019.

[30] Çeltek, Seyit Alperen, et al. «Nesnelerin İnterneti Tabanlı Yangın Alarm Sistemi Tasarımı ve Uygulaması.» Gaziosmanpaşa Bilimsel Araştırma Dergisi 6.3 (2017): 66-72.

[31] Sazak, Tayfun, and Yalçın Albayrak. "Nesnelerin İnterneti (IoT) Üzerine Ortam Verilerini Toplayan ve Uzaktan Takibini Sağlayan Bir Sistem Tasarımı, 19." Akademik Bilişim Konferansı, Aksaray, Türkiye (2017).

[32] Mohammed, Mohammed Sufyan. Akıllı şehirler için merkezi otopark yönetim sistemi tasarımı ve uygulaması. MS thesis. Fen Bilimleri Enstitüsü(2018).

[33] Arda, İbrahim. Araç giriş ve çikiş kontrolü için IOT tabanli çalişan trafik bariyerinin geliştirilmesi ve prototip üretimi. Diss. Marmara Universitesi (Turkey), 2019.

[34] Satar, Burak. "Nesnelerin Interneti Tabanlı Bir Otobüs Durak Sistemi Tasarımı An IoT Based Bus Stop System Design." National Conference on Electrical and Electronics Engineering. 2016.

[35] Can, Ö. Z., and Yasemin Topaloğlu. "Nesnelerin İnterneti Yaklaşımıyla Konvoy Araçların Yönetimi." Türkiye Bilişim Vakfı Bilgisayar Bilimleri ve Mühendisliği Dergisi 15.1(2022): 33-37.

[36] Yıldız, Ömer. Akıllı sağlık uygulamaları için bir uzaktan hasta takip sistemi tasarımı ve gerçeklenmesi. Diss. Bursa Uludag University (Turkey), 2019.

[37] Cicioğlu, Murtaza, And Ali Çalhan. "Bulut Destekli Medikal Nesnelerin İnterneti Tabanli Uzaktan Sağlik İzleme Sistemi." Uludağ Üniversitesi Mühendislik Fakültesi Dergisi 26.3(2021): 1083-1096.

[38] Ersin, Çağatay, Y. A. Z. Mustafa, and Mustafa Karhan. "Savunma Sanayi İçin Örnek Bir IoT Uygulaması." Electronic Letters on Science and Engineering 15.3 (2019): 66-73.

[39] Ersin, Çağatay, and Ö. Z. Ali. "İş sağlığı ve güvenliği için IoT tabanlı gömülü sistem tasarımı ve uygulaması." Avrupa Bilim ve Teknoloji Dergisi 18 (2020): 494-504.

[40] Dulluç, Sinem, İsmail Akdağ, And Merih Palandöken. “Akilli Fabrika Yönetim Bilişim Sistemi Tasarimi.”, International Antalya Scientific Research Innovative Studies Congress, Antalya/ Turkey, 2021.

[41] Duan, Kang-Kang, and Shuang-Yin Cao. “Emerging RFID technology in structural engineering–A review.” Structures. Vol. 28. Elsevier, 2020.

[42] Ateş, Salih Berkan. Akıllı şebekeler uygulamalarına yönelik nesnelerin interneti (IoT) tabanlı prototip transformatör merkezi tasarımı ve uygulaması. Diss. Necmettin Erbakan University (Turkey), 2018.

[43] ASIR Mehmet, Dağırım transformatörlerinin parametrelerinin nesnelerin interneti kullanarak uzaktan izlenmesi (Yüksek Lisans Tezi, İstanbul Üniversitesi) 2020.

[44] AYGÜN, Sercan, and Abdullah SEVİN. “Trafo Merkezleri İçin Nesnelerin İnterneti Tabanlı Kontrol Sistemi Tasarımı Ve Uygulaması.” Avrupa Bilim ve Teknoloji Dergisi 29, 2021, pp. 30-35.

[45] Güleydin, Murat, Serdar Ekinci, and Davut İzci. “YER ALTI ELEKTRİK DAĞITIM HATLARINDA MEYDANA GELEN ENERJİ KAYIPLARININ TESPİTİ İÇİN IOT TABANLI MODÜLER SİSTEM TASARIMI, “ Batman, Turkey International Informatics Congress (IIC2022) 17-19 February 2022.

[46] Demircan, Batın. Endüstriyel tabanlı sistem için bulut bilişim tabanlı nesnelerin interneti uygulaması. MS thesis. Balıkesir Üniversitesi Fen Bilimleri Enstitüsü, 2019.

[47] Vural, Arif. Fotovoltaik panellerde güç üretiminin nesnelerin interneti tabanlı gerçek zamanlı uzaktan izlenmesi ve verilerin saklanması. MS thesis. 2022.

[48] Centenaro, Marco, et al. “Long-range communications in unlicensed bands: The rising stars in the IoT and smart city scenarios.” IEEE Wireless Communications 23.5.2016, pp.60-67.

[49] Yilmaz, Musa. “The Prediction of Electrical Vehicles’ Growth Rate and Management of Electrical Energy Demand in Turkey.” 2017 Ninth annual IEEE green technologies conference (GreenTech). IEEE, 2017.

[50] Dinçer, H., F. Mutlu, and M. Kuzlu. “Sayısal Teknolojinin Elektrik Şebeke Ağına Katılması: Akıllı Şebeke, EMO IV.” Enerji Verimliliği ve Kalitesi Sempozyumu, 2011.

Chapter 3

HEART FAILURE PREDICTION WITH MACHINE LEARNING ALGORITHMS

Omer Faruk SOYLEMEZ[1]

1 Dicle University, Engineering Faculty, Department of Computer Engineering, Diyarbakir, Türkiye

INTRODUCTION

One of the leading cause of death around the globe is cardiovascular diseases (CVD). In 2019, nearly 18 million people died from CVD, that accounts for 32% of global deaths. Heart attack and stroke cases contributes to 85% of these deaths. 38% of the 17 million premature deaths (under 70 years old) due to non-communicable diseases in 2019 are due to CVDs [1].

CVDs consist of a number of diseases with complications of the vessels of heart and blood. They include coronary heart disease (related to the blood vessels that feed the heart muscle), cerebrovascular diseases (related to the blood vessels feeding the brain), rheumatic, peripheral and congenital heart diseases. Heart attacks and strokes are often caused by a blockage that prevents blood from flowing to the heart or brain [2]. The most common reason for this is when fatty deposits build up on the inner walls of the blood vessels that feed the heart or brain and block the vascular pathways. Likewise, bleeding of a blood vessel in the brain or a blood clot can cause cerebral palsy.

Unhealthy diet, tobacco and alcohol use, physical inactivity are the leading behavioral risk factors for heart disease and stroke [3]. These behavioral risk factors may show themselves as obesity, elevated blood pressure and blood sugar. These risk factors can be measured in primary health care facilities and actions can be taken regarding the risks of heart attack, stroke, heart failure and other complications [4].

Early diagnosis is an important preventive and protective practice for CVD as in many diseases. Many screening tests have been recommended for CVD [5,6]. In general, these tests examine internal and lifestyle factors such as body mass index, cholesterol level, blood pressure, blood sugar level, dietary habits, smoking and physical activity. In addition to screening tests, specialists can request electrocardiogram, echocardiogram, Holter monitoring, cardiac catheterization, computed tomography and magnetic resonance imaging for patients when detailed examination is deemed necessary [7,8].

Artificial intelligence and related technologies are spreading rapidly considering the past few years. In recent years, these technologies have also found a place for themselves in applications in the field of health [9,10]. By using artificial intelligence technologies in the field of healthcare, significant progress has been made in areas such as medical image analysis, diagnosis and treatment, drug discovery and remote assistance [11,12]. It is possible to benefit from artificial intelligence and machine learning methods for the early diagnosis of patients at risk of CVD.

In recent years, there has been an increasing amount of studies on heart failure prediction with machine learning approaches. Cheon et al. [13] used a deep neural network to detect stroke on 15099 patients. Authors employed PCA to extract relevant background features and used this features to predict stroke. They have

compared their approach with five other machine learning approaches and achieved .8343 AUC. Chun et al. [14] predicted the risk of stroke on a dataset consisting of half million adults. They have compared Cox models, machine learning algorithms and ensemble methods in their study. Their results shows that gradient boosted tree achieved .833 AUC in men and .836 AUC in women for 9-year stroke risk prediction. Sailasy and Kumari [15] used various machine learning models to predict the possibility of stroke in the brain. They have used various machine learning algorithms and achieved an accuracy of 82% with naïve Bayes approach.

In this study, heart failure prediction was performed with the help of machine learning methods. The data set of the study consists of 918 observations [16]. Logistic regression, naive bayes, support vector machines, K nearest neighbor, decision tree, random forest algorithms were used for heart failure prediction. The performances of the algorithms were measured by 5-fold cross-validation with equal numbers of positives and negatives in each fold.

The rest of this study is organized as follows: Theoretical background on used machine learning algorithms are given in section 2. Material is presented in section 3. Performed experiments are given in section 4. Result and discussion is carried in section 5. Final conclusions are narrated in section 6.

THEORETICAL BACKGROUND

Logistic Regression

Logistic regression is a statistical analysis method for predicting a binary outcome based on previous observations of a distribution. A logistic regression model attempts to predict a dependent data variable by analyzing the relationship between one or more available independent variables. Logistic regression has an important place in machine learning methods. Logistic regression is frequently used to make a basic assessment on many problems due to its ease of use and low cost of operation. Logistic regression uses historical data for forecasting. Therefore, it tends to perform better as more samples are added to the observation set.

The output of the logistic regression is between 0 and 1. Therefore, it is a suitable function for binary classification. The formulation of the logistic regression is given in eq. (1). Here, Θ is the parameter to be optimized and X is the input. A loss function should be used to optimize this process. Log-likelihood function is used in logistic regression eq. (2). Here m is the number of samples in the training data, y^i is the label of ith sample, and p^i is the predicted value of ith sample.

$$h_\Theta(X) = \frac{1}{1 + e^{-\Theta x}} \tag{1}$$

$$J(\Theta) = -\frac{1}{m}\sum_{m}^{i=1}(y^i log(p^i) + (1 - y^i) log(1 - p^i)) \tag{2}$$

Naive Bayes

Named after Mathematician Thomas Bayes, Naïve Bayes is a classification and categorization algorithm. Naïve Bayes aims to find the category or class of the data given to the system with a series of calculations characterized according to principles of probability.

Naïve Bayes theorem can be formulated as shown in eq. (3). Here $\boldsymbol{x}$ represents a feature from the feature set, $p(C_k)$ is the possible class outcomes or prior probability, $p(C_k \mid \boldsymbol{x})$ is the posterior probability, $p(\boldsymbol{x} \mid C_k)$ is likelihood of the event and $p(\boldsymbol{x})$ is the evidence of the occured events.

$$p(C_k \mid \boldsymbol{x}) = \frac{p(C_k)\, p(\boldsymbol{x} \mid C_k)}{p(\boldsymbol{x})} \tag{3}$$

Support Vector Machines

Support Vector Machines (SVM) is a supervised learning methods generally used in classification problems. SVM tries to find a hyperplane that separates instances into two classes. It particularly aims to position this hyperplane with the maximum possible margin distance for the points of both classes. It performs better when the margin is higher and lower when margin is minimal. With $\hat{y}$ as the target class, $\boldsymbol{w}$ as the weight vector, $\boldsymbol{x}$ as the input vector and b as the bias, a general equation for SVM can be formulated as in eq. (4).

$$\hat{y} = \begin{cases} 0 \; if \; \boldsymbol{w}^T \cdot \boldsymbol{x} + b < 0, \\ 1 \; if \; \boldsymbol{w}^T \cdot \boldsymbol{x} + b \geq 0 \end{cases} \tag{4}$$

SVM works well on small to medium data, but on complex datasets, low dimensions may not be sufficient to explain. For handling high dimensional computations, different kernel functions are used with SVMs. These kernels create different perspectives for solving complex problems. Examples to some of these kernels are given in Figure 1.

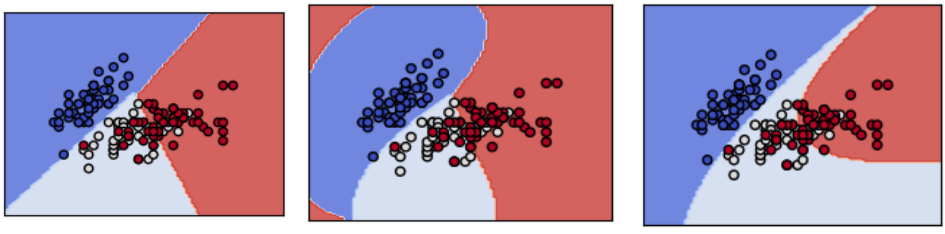

(a) (b) (c)

Figure 1. Different kernels for SVM. (a) Linear kernel (b) RBF kernel (c) Polynomial kernel

K-Nearest Neighbors

K-nearest neighbors (KNN) is one of the supervised machine learning algorithms that is used for both classification and regression tasks. The KNN classifier determines

the class of an element in a dataset using the principle of majority voting. Here, K denotes the number of nearest neighbor data points to be used for classification or regression task. Figure 2 shows an example of KNN classification with different k values. For different k values, assigned class of the datapoint changes.

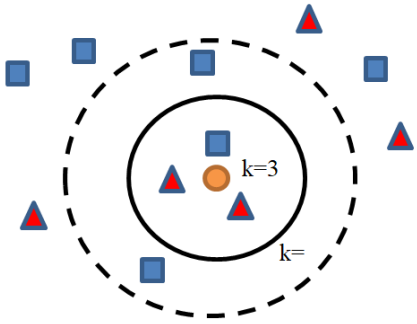

Figure 2. An example for KNN classification. Yellow circles' class is red if k=3, blue if k=5.

The measure of the neighborhood of the points to each other is calculated with different geometric distances. The most common distance used for KNN is Euclidean distance. There also other distance metrics used for KNN specific to various tasks, such as, Manhattan distance, cosine distance, Jaccard distance and Hamming distance

Decision Trees

Decision trees are a type of supervised machine learning algorithms that are used for both classification and regression tasks. As the name suggests, decision trees are the one of tree-based algorithms. A tree-based algorithm is formed of nodes, branches and leaves, that aims to facilitate the selection process. Nodes serves as decision makers by evaluating a single or multiple features of the data. Branches denotes the outcome of nodes. Leaves on the other hand, holds a class label for the selected path. In a classification scenario, decision trees are traversed in a top-down fashion through nodes ending up on leaves.

Random Forest

Random forest is a popular machine learning algorithm that can be applied to both regression and classification problems, which yields satisfying results even without hyper param evaluation. Random forest is an ensemble of large number of decision trees. Each decision tree is trained with a random subset of both dataset and feature set. In a classification problem, predicted class is found with majority voting. In a regression problem, the average of all models is taken as the target.

In random forest, the training takes place on different data sets and feature sets. This adds variance to the selection process, therefore reducing the chance of overfitting. It also reduces the chance of finding outliers in the subsets that are created with the bootstrap method. A random forest classification example is given

on Figure 3. Majority voting scheme is used for classification task.

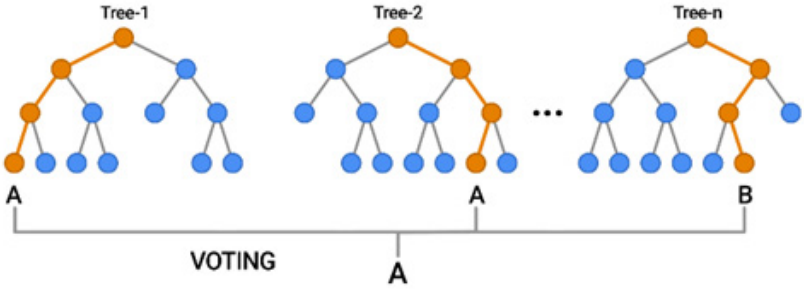

Figure 3. A random forest example. Classification is done with majority voting. Source [17]

MATERIAL

Dataset

We have used publicly available heart failure prediction dataset in this study [16]. The dataset was created by combining publicly available datasets, yet those datasets were never combined before. A total of 5 heart datasets from different sites are combined over 11 common features. Combined datasets are available under UCI Machine Learning Repository [18] There are 1190 total observations in the dataset. Removing 272 duplicated entries, final dataset composes of 918 observations. Attribute information of observations are given in Table 1.

Correlated variables do diminish the performance of the model by overfitting. Therefore, we computed a pairwise correlation for the numerical attributes of the dataset. Figure 4 shows the correlation plot of the heart failure prediction dataset. Heart disease has a high negative correlation with "MaxHR" and small negative correlation with "Cholesterol". It has positive correlations with "Oldpeak", "FastingBS" and "RestingBP". Correlation of all features are in plausible range so we did not drop out any features.

Table 1. Attribute information for observations.

Attibute	Information	Value
Age	age of the patient	Years
Sex	sex of the patient	M: Male, F: Female
ChestPainType	chest pain type	TA: Typical Angina, ATA: Atypical Angina, NAP: Non-Anginal Pain, ASY: Asymptomatic
RestingBP	resting blood pressure	mm Hg
Cholesterol	serum cholesterol	mm/dl
FastingBS	fasting blood sugar	1: if FastingBS > 120 mg/dl, 0: otherwise
RestingECG	resting electrocardiogram results	Normal: Normal, ST: having ST-T wave abnormality (T wave inversions and/or ST elevation or depression of > 0.05 mV), LVH: showing probable or definite left ventricular hypertrophy by Estes' criteria

MaxHR	maximum heart rate achieved	Numeric value between 60 and 202
ExerciseAngina	exercise-induced angina	Y: Yes, N: No
Oldpeak	oldpeak = ST	Numeric value measured in depression
ST_Slope	the slope of the peak exercise ST segment	Up: upsloping, Flat: flat, Down: downsloping
HeartDisease	output class	1: heart disease, 0: Normal

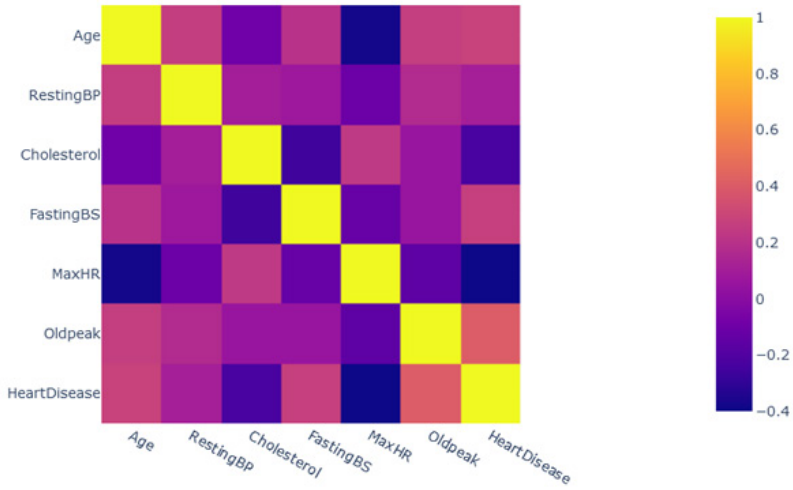

Figure 4. Pairwise correlation plot for numerical attributes of the dataset.

Metrics

We used five metrics for evaluation in this study. TP (True Positive) denotes the number of correctly predicted heart disease and TN (True Negative) denotes the number of correctly predicted no heart disease. FP (False Positive) and FN (False Negative) denotes the number of incorrectly predicted heart diseases and no heart diseases, respectively. By employing these confusion matrix parameters, we have calculated precision, recall, f1-score and accuracy as evaluation metrics. Equations for these metrics are given in eq. (5) to eq. (8). We employed AUC (Area Under receiving operating Characteristic) score as the main classification metric. ROC curve is a probability curve, plotted with TPR against FPR. The area under the curve is denoted as AUC score and is an interpreter for model performance. AUC is more robust and reliable metric for classification since focuses on more than one aspect of classification.

$$Precision = \frac{TP}{TP + FP} \tag{5}$$

$$Recall = \frac{TP}{TP + FN} \tag{6}$$

$$F1 - Score = \frac{2 \times TP}{2 \times TP + FP + FN} \quad (7)$$

$$Accuracy = \frac{TP + TN}{TP + TN + FP + FN} \quad (8)$$

EXPERIMENTS

We have conducted experiments with stratified k-fold cross validation setting. Stratification is made according to target labels, thus each fold had same number of positive and negative samples. K value is selected as 5 and same seed is used for all experiments.

The following algorithms are used for heart failure prediction: Logistic regression, naïve Bayes, support vector machines, k nearest neighbor, decision trees and random forest. Parameters for each of the algorithms are given in Figure 5.

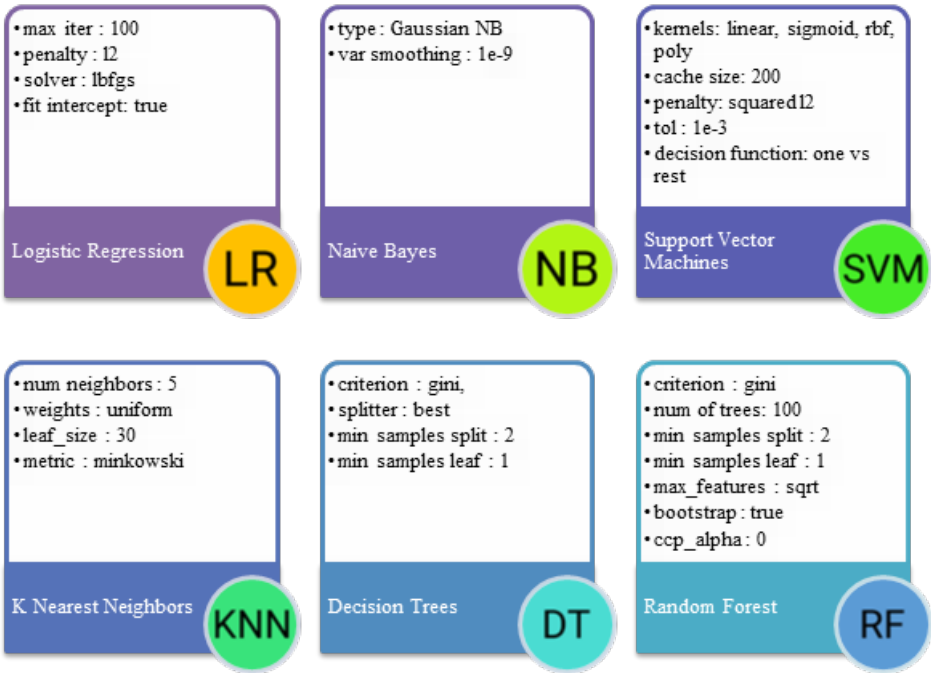

Figure 5. Parameters for used algorithms in the study.

RESULTS AND DISCUSSION

The following 9 classifiers are used in the study: Logistic regression, Naïve Bayes, SVM-Linear, SVM-sigmoid, SVM-rbf, SVM-poly, K nearest neighbors, decision trees and random forest. By conducting each configuration 5 times, a total of 45 sessions were held in the study. Experimental results for heart failure prediction with the mentioned classifiers are given in Table 2. AUC is used as primary metric in the study. AUC is given for each fold along with a weighted overall average. Precision, recall, f1-score and accuracy are calculated by taking the mean of all folds.

Table 2. Experimental results for heart failure prediction. AUC is given for fold wise and overall. Other metrics are average for all folds.

Algorithms	AUC						Precision	Recall	F1	Accuracy
	F1	F2	F3	F4	F5	overall	%	%	%	%
LR	.880	.853	.813	.857	.739	.828	83.9	82.8	82.7	83.1
NB	.860	.883	.807	.813	.815	.836	84.7	83.6	83.4	83.7
SVM-linear	.869	.849	.813	.846	.733	.822	83.3	82.2	82.1	82.4
SVM-sigmoid	.852	.756	.811	.804	.711	.787	78.8	78.7	78.6	78.8
SVM-rbf	.910	.843	.813	.816	.735	.823	83.2	82.3	82.4	82.7
SVM-poly	.897	.843	.797	.817	.735	.818	82.8	81.8	81.7	82.1
KNN	**.923**	**.848**	**.835**	**.829**	**.776**	**.842**	**84.9**	**84.2**	**84.2**	**84.5**
DT	.756	.777	.771	.745	.689	.747	75.5	74.7	74.2	74.5
RF	.883	.839	.810	.815	.767	.814	82.8	81.4	81.3	78.0

Evaluating Table 2, KNN algorithm found as the best achieving algorithm with .842 AUC score. It is followed by naïve bayes (.836 AUC) and logistic regression (.828 AUC) by a small margin. SVM kernels displayed similar AUC performance (rbf - .823, linear - .822, poly - .818) except sigmoid kernel. Sigmoid kernel displayed relatively low performance with .787 AUC. Tree-based algorithms showed somewhat inferior performance to non-tree-based algorithms. Especially, decision tree was the algorithm with the lowest performance of all with .747 AUC. However, random forest algorithm showed somewhat similar performance to non-tree-based algorithms. Random forest approach with the given configurations achieved .814 AUC.

We believe poor achievement of the decision tree algorithm is due to their several shortcomings. Firstly, decision trees can be sensitive to distribution of the data. That means a small change in distribution may yield an exceptionally different tree. Secondly, they are prone to overfitting. This is more evident if trees are too deep then in should be. Pruning, validation and early stopping can be used to overcome this. Finally, they face difficulties when predicting out of sample observations. Indeed, correct prediction is a coin toss in such situations. However, random forest approach overcomes these shortcomings. Random forest works with subsets of data, thus reducing overfitting. Ensembling nature also helps to alleviate bias and variance issues. We believe success of random forest approach is due to advantages of bootstrapping and ensembling.

Random forest feature importance is given in Figure 6. The feature importance outlines relevant and important features. It gives an insight about the features and prioritizes features that could be employed in some other classification techniques. A higher value means more important feature.

ST_Slope is found as the most important feature for assessing heart failure prediction with .554 importance. It is followed by Sex - .088, ChestPainType - .068, and FastingBS – .066. The rest are ExerciseAngina - .049, Cholosterol - .046,

OldPeak - .034, RestingECG - .027, RestingBP - .022, MaxHR - 022, and Age - .019.

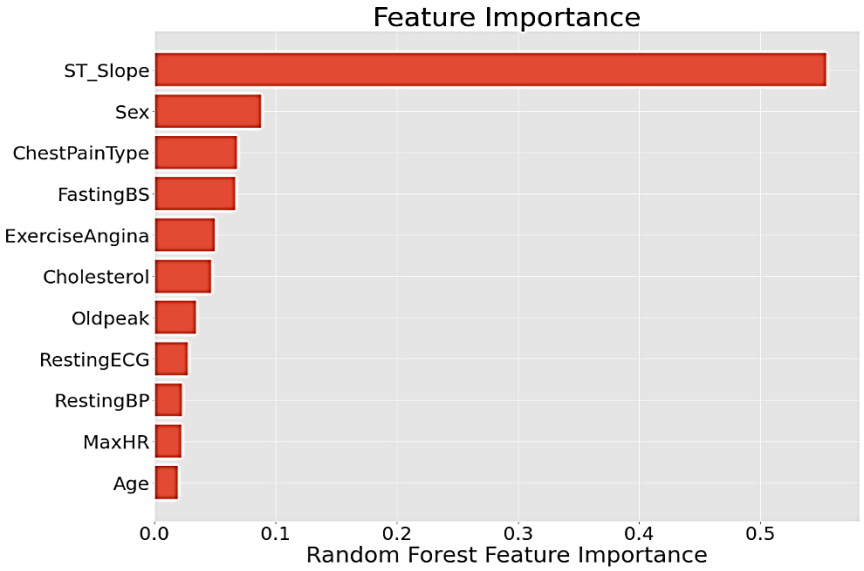

Figure 6. Random forest feature importance.

Comparison with existing studies on heart failure prediction is given in Table 3. Cheon et al. [13] used several different algorithms for heart failure prediction on KHNDS dataset [19]. They found DNN as the best achieving classifier with .8343 AUC and SVM as the worst achieving classifier with .7151 SVM. We believe this large gap is due to inefficient parametrization of the proposed algorithms. Chun et al. [14] used CKB dataset [20] for heart failure prediction. Authors found the GBT as the best achieving algorithm with .8345 AUC and RSF as the least performing algorithm with .8290 AUC. Their study sample composes of half million patients, so we believe all of the algorithms found robust enough features for classification. Sailasya and Kumari [15] used the same dataset [16] as we used in this study. They didn't present AUC scores but present accuracies in their study. Their best and worst performing algorithms were naïve bayes with 82% accuracy and decision trees with 66% accuracy, respectively. Our decision trees approach also showed the worst performance as in their study but with a higher accuracy as 74.50% and AUC as .8420. Meanwhile, our KNN approach performed better than other approaches with .8450 AUC.

Table 3. Comparison with existing studies on heart failure prediction (ADB: AdaBoost, DNN: Deep Neural Network, DT: Decision Trees, GBT: Gradient Boosted Tree, GNB: Gaussian Naive Bayes, LR: Logistic Regression, MLP: Multi Layer Perceptron, KNN: K nearest neighbor, RF: Random Forest, RSF: Random Survival Forest, SVC: Support Vector Machine)

Study	Dataset	Algorithms	Metric				
			Precision	Recall	F1	Acc	AUC
Cheon et al. [13]	KNHDS [19]	RF	18.85	60.27	-	78.44	.7759
		ADB	20.14	63.24	-	79.28	.7925
		GNB	15.6	69.73	-	70.63	.7808
		KNN	19.71	59.19	-	79.68	.7211
		SVC	13.8	59.73	-	70.22	.7151
		DNN	25.7	64.32	-	84.03	.8348
Chun et al. [14]	CKB [20]	RSF	-	-	-	-	.8290
		LR	-	-	-	-	.8315
		SVM	-	-	-	-	.8305
		GBT	-	-	-	-	.8345
		MLP	-	-	-	-	.8315
Sailasya and Kumari [15]	Kaggle [16]	LR	77.5	77.5	77.6	78	-
		DT	77.5	77.5	77.6	66	-
		RF	72	73.5	72.7	73	-
		KNN	77.4	83.7	80.4	80	-
		SVM	78.6	83.8	81.1	80	-
		NB	79.2	85.7	82.3	82	-
Proposed	**Kaggle** [16]	LR	83.9	82.8	82.7	83.1	.828
		NB	84.7	83.6	83.4	83.7	.836
		SVM-linear	83.3	82.2	82.1	82.4	.822
		SVM-sigmoid	78.8	78.7	78.6	78.8	.787
		SVM-rbf	83.2	82.3	82.4	82.7	.823
		SVM-poly	82.8	81.8	81.7	82.1	.818
		KNN	**84.9**	**84.2**	**84.2**	**84.5**	**.842**
		DT	75.5	74.7	74.2	74.5	.747
		RF	82.8	81.4	81.3	78.0	.814

CONCLUSION

In this study, we performed heart failure prediction with the help of machine learning algorithms. The data set of the study consists of 918 observations. Logistic regression, naive bayes, support vector machines, K nearest neighbor, decision trees, random forest algorithms were used for heart failure prediction. K nearest neighbor algorithm was found as the most efficient algorithm with .842 AUC score. Meanwhile decision tree classifier was the worst performer with .747 AUC score.

CVDs are a leading cause of death worldwide. Therefore, early diagnosis of CVD is important for preventive measures. More accurate predictions may assist experts and save lives. We proposed several different machine learning algorithms for heart failure prediction in this study. Further research may use larger databases with diverse machine learning algorithms for heart failure prediction.

REFERENCES

[1] WHO. Cardiovascular diseases (CVDs) 2021. https://www.who.int/news-room/fact-sheets/detail/cardiovascular-diseases-(cvds) (accessed October 10, 2022).

[2] Piché ME, Tchernof A, Després JP. Obesity Phenotypes, Diabetes, and Cardiovascular Diseases. Circ Res 2020:1477–500. https://doi.org/10.1161/CIRCRESAHA.120.316101.

[3] Clark AM, DesMeules M, Luo W, Duncan AS, Wielgosz A. Socioeconomic status and cardiovascular disease: Risks and implications for care. Nat Rev Cardiol 2009;6:712–22. https://doi.org/10.1038/nrcardio.2009.163.

[4] National Center for Chronic Disease Prevention and Health Promotion. Heart Disease and Stroke | CDC. Natl Cent Chronic Dis Prev Heal Promot 2022. https://www.cdc.gov/chronicdisease/resources/publications/factsheets/heart-disease-stroke.htm (accessed October 10, 2022).

[5] Søgaard R, Diederichsen ACP, Rasmussen LM, Lambrechtsen J, Steffensen FH, Frost L, et al. Cost effectiveness of population screening versus no screening for cardiovascular disease: the Danish Cardiovascular Screening trial (DANCAVAS). Eur Heart J 2022. https://doi.org/10.1093/eurheartj/ehac488.

[6] Wong ND, Budoff MJ, Ferdinand K, Graham IM, Michos ED, Reddy T, et al. Atherosclerotic cardiovascular disease risk assessment: An American Society for Preventive Cardiology clinical practice statement. Am J Prev Cardiol 2022;10:100335. https://doi.org/10.1016/j.ajpc.2022.100335.

[7] Flores N, Reyna MA, Avitia RL, Cardenas-Haro JA, Garcia-Gonzalez C. Non-Invasive Systems and Methods Patents Review Based on Electrocardiogram for Diagnosis of Cardiovascular Diseases. Algorithms 2022;15. https://doi.org/10.3390/a15030082.

[8] Abubaker M, Babayigit B. Detection of Cardiovascular Diseases in ECG Images Using Machine Learning and Deep Learning Methods. IEEE Trans Artif Intell 2022:1–1. https://doi.org/10.1109/tai.2022.3159505.

[9] Sun L, Gupta RK, Sharma A. Review and potential for artificial intelligence in healthcare. Int J Syst Assur Eng Manag 2022;13:54–62. https://doi.org/10.1007/s13198-021-01221-9.

[10] Nguyen DC, Pham Q-V, Pathirana PN, Ding M, Seneviratne A, Lin Z, et al. Federated Learning for Smart Healthcare: A Survey. ACM Comput Surv 2023;55:1–37. https://doi.org/10.1145/3501296.

[11] Kumar R, Saha P. A Review on Artificial Intelligence and Machine Learning to Improve Cancer Management and Drug Discovery. … J Res Appl Sci … 2022.

[12] Rajpurkar P, Chen E, Banerjee O, Topol EJ. AI in health and medicine. Nat Med 2022;28:31–8. https://doi.org/10.1038/s41591-021-01614-0.

[13] Cheon S, Kim J, Lim J. The use of deep learning to predict stroke patient mortality. Int J Environ Res Public Health 2019;16. https://doi.org/10.3390/ijerph16111876.

[14] Chun M, Clarke R, Cairns BJ, Clifton D, Bennett D, Chen Y, et al. Stroke risk prediction using machine learning: A prospective cohort study of 0.5 million Chinese adults. J Am Med Informatics Assoc 2021;28:1719–27. https://doi.org/10.1093/jamia/ocab068.

[15] Sailasya G, Kumari GLA. Analyzing the Performance of Stroke Prediction using ML Classification Algorithms. Int J Adv Comput Sci Appl 2021;12:539–45. https://doi.org/10.14569/IJACSA.2021.0120662.

[16] Fedesoriano. Heart Failure Prediction Dataset. Kaggle 2020. https://www.kaggle.com/datasets/fedesoriano/heart-failure-prediction (accessed October 3, 2022).

[17] Guillame-Bert M, Bruch S, Gordon J, Pfeifer J. Introducing TensorFlow Decision Forests — The TensorFlow Blog 2021. https://blog.tensorflow.org/2021/05/introducing-tensorflow-decision-forests.html (accessed October 10, 2022).

[18] UCI Machine Learning Repository. Heart Disease Databases. Cent Mach Learn Intell Syst 1988. https://archive.ics.uci.edu/ml/machine-learning-databases/heart-disease/ (accessed October 3, 2022).

[19] Lee WK, Lim D, Park H. Disability-adjusted life years (DALYs) for injuries using death certificates and hospital discharge survey by the Korean burden of disease study 2012. J Korean Med Sci 2016;31:S200–7. https://doi.org/10.3346/jkms.2016.31.S2.S200.

[20] Chen Z, Lee L, Chen J, Collins R, Wu F, Guo Y, et al. Cohort profile: The Kadoorie Study of Chronic Disease in China (KSCDC). Int J Epidemiol 2005;34:1243–9. https://doi.org/10.1093/ije/dyi174.

Chapter 4

ANALYSIS OF DIFFERENT FREQUENCIES GPR ANTENNES FOR ASSESSING THE HEALTH OF STRUCTURES

Gokhan KILIC[1], Diaa E. FAWZY[2], A.M.M.A. ALLAM[3]

1 Izmir University of Economics, Engineering Faculty, Civil Engineering Department, Izmir, Türkiye
2 Izmir University of Economics, Engineering Faculty, Department of Aerospace Engineering, Izmir, Türkiye
3 German University in Cairo, Faculty of Engineering, Department of Electrical and Telecommunication Engineering, Cairo, Egypt

INTRODUCTION

Assessment and inspection of tunnels are crucial and should be prioritized by structural engineers and tunnel owners. In order to preserve and track the structure's health currently, and throughout its life cycle, regular inspection is required. Early detection of structural problems can help to ensure that the structure maintains its integrity over the duration of its life. Examples of these flaws include corrosion and the development of cracks within the internal sections of the building. Other problems that may be identified earlier with the outline inspection are delamination of the tunnel surface and rebar corrosion. The early identification of flaws is a key benefit of modern technologies including Ground Penetrating Radar (GPR). The effective functioning of society is dependent on tunnel structures, which have environmental, social, and economic aspects. Since tunnel structures play a vital role in society, it is essential that they are well-maintained and improved, which requires accurate analysis. This demands the creation of robust mechanisms to facilitate such assessments. Engineers and researchers have dedicated much time to find the most accurate analysis and inspection mechanisms. In recent years, developments in NDT (Non-Destructive Testing) techniques have brought major advances in testing the structural integrity of structures. NDT is the most favoured option because of its cost-effectiveness reliability and effectiveness. In addition, these non-invasive methods have increased the knowledge of engineers conducting the analysis, allowing a more detailed insight into defects. The development of NDT mechanisms of assessment led to further improvement and development, parallel to an improved understanding of the internal structures of tunnels.

NDT is essentially a method of testing for defects and faults without causing harm to structures. It has become one of the most preferred methods for monitoring tunnel health because it allows remedial repairs without the need for extracting samples. According to [1], rather than the assessment or survey of the overall structure, NDT is the investigation of certain aspects, focused on a particular goal [2]. Also known as the impulse radar method, NDT is particularly crucial for measuring and evaluating masonry and tunnels. As a result, engineers and scientists working with NDT are now widely referred to as 'geophysicists'. GPR is a system implemented in superficial geology, facilitating the mapping of shallow structures using radio wave energies. It may also be implemented in civil engineering for the imaging of features invisible to the naked eye, such as foundations, pipes, land mines, and geological layers. GPR is a key instrument utilized in modern advanced NDT of structures [3-5].

The assessment and monitoring of structures using GPR, however, is not a new approach. GPR has previously been shown to be effective in monitoring of tunnel surfaces [6-9] in the context of:

- Cover length of Rebar
- Rebar Assessment
- Crack depth
- Moisture ingress
- Delamination
- Location of beams and columns
- Cavities
- Tunnel Abutments

The antennas used in GPR technology may receive or transmit signals and can be used for creating images of a structure's subsurface by emitting electromagnetic waves. The wide band signals are emitted from high power pulse generators [9]. The technology may also make use of different frequencies for a more accurate image of the subsurface [10-14]. Low frequency signals, although able to reach deeper into the structure, cannot deliver high-resolution images. High frequency signals, on the other hand, produce high quality images but are unable to penetrate deeply. An effective combination of these therefore can improve the accuracy of imaging. The GPR technique makes use of electromagnetic pulses, which interact with the subsurface of the object after being transmitted via a source antenna. After interception by a receiving antenna, the reflected signal is then analysed and used to construct an image of the underlying features [14-20].

This study will describe case studies focused on the application of different GPR methods, using various antennae systems in the assessment of conditions of tunnels. This description forms part of a wider study assessing the effectiveness of a range of NDT methods in the analysis of the current health of tunnels. This research also provides a demonstration of and discussion of the technique's success with GPR for determining the structural integrity of an extensively utilized tunnel. Various antennas are utilized with different frequencies and application methods for GPR (2 GHz and 500 MHz GPR antennas). The goal of the study is to improve knowledge of structural faults and to identify the most appropriate instrument for such work. This research will show how GPR mapping functions and how it can provide valuable information on rebar position (lower and upper reinforcement). Additionally, it will demonstrate how such methods may reveal structural details that may otherwise go unnoticed, as well as moisture intrusion.

THEORETICAL BACKGROUND

Visual Inspection

Initially, a visual inspection was completed using a high-definition camera, a hammer, crack gauges, a torch, and a ladder. Defects observed on the structure included exposed rebars in multiple locations, due to deterioration. Substantial concrete repair was required for the surface spans and piers. Due to the very poor

condition of the Span at the west end, intensive assessment is required before carrying out any repair or remedial work.

The initial visual inspection involved no subsurface assessments or the investigation of the structure. The GPR survey was carried out in order to detect the upper and lower rebar location and cover depth, and to identify locations of moisture entry, as well as other structural flaws.

The GPR System and Survey

Electromagnetic pulses are used as the basis for the basic operation of GPRs, with some of the energy being reflected at subsurface contacts and some being transported into deeper layers. To demonstrate how GPR works, Figure 1 shows data processing for an electromagnetic wave [21,23].

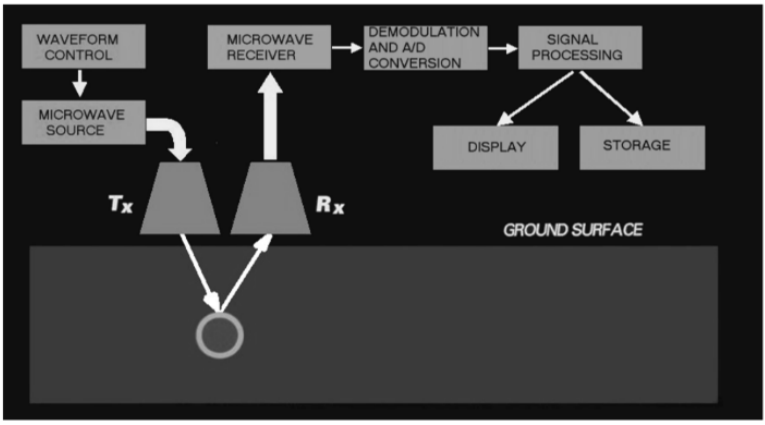

Figure 1. GPR operating principles [19,20]

Radargrams and time slices are two ways that GPR data may be shown on a computer screen in various combinations. The radargrams acquisition position is depicted in Figure 2(a), in which the GPR antenna is surveyed in the x-way while the returned signals are continually recorded on a computer. The time slice in Figure 2 (b) shows the data that was collected on a shallow lengthways on the computer screen. Radargrams are recorded in the x-way and shown in the data in Figure 2(c). Figure 2(d) shows slices taken at various periods and various depths after the completion of the survey on the designated region with all parallel lines.

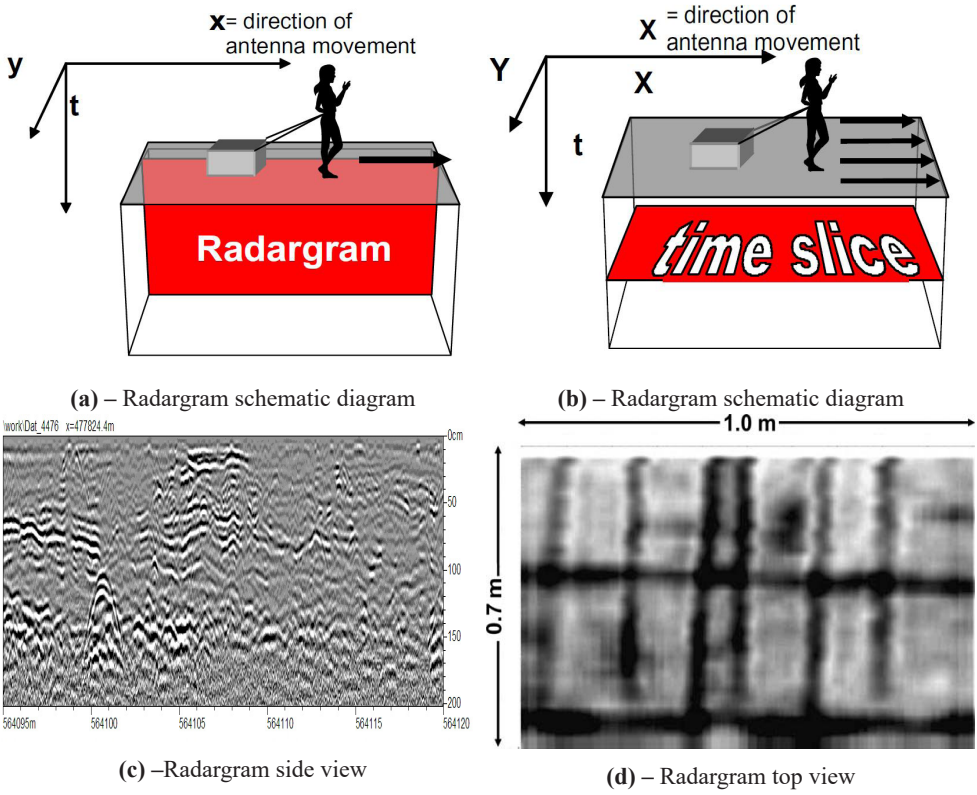

(a) – Radargram schematic diagram

(b) – Radargram schematic diagram

(c) –Radargram side view

(d) – Radargram top view

Figure 2. Radargram schematic diagram [21, 23]

In both low- and high-frequency GPR antenna, Figure 3 depicts the connection between resolution and penetration depth. Higher frequencies produce more resolution, which reduces penetration depth, and are a direct function of antenna frequency.

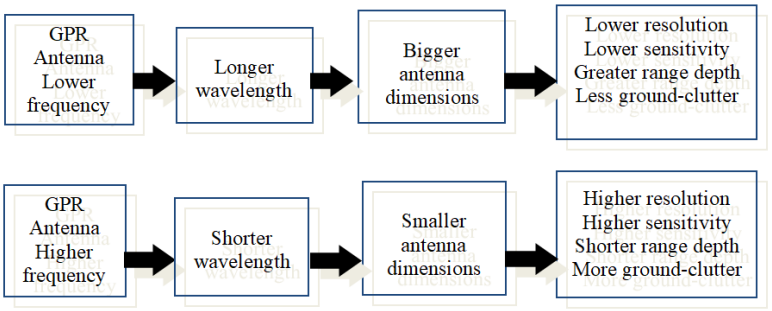

Figure 3. Summary of GPR antenna frequency [23]

The first antenna was the Conquest (2 GHz), specifically designed to inspect structure surfaces, providing high quality results with easy manoeuvrability. The lightweight antenna provides dense sample data, allowing the production of high-quality tomography along with 3D images which are effective in the interpretation

and analysis of results. For the in-line survey depicted in Figure 4, two antenna types were used, each resonating a different frequency.

(a) **(b)**

Figure 4. (a) GPR Installation on the Site, (b) Case Study Survey Area

Figure 5. GPR different antennas: with Conquest (2 GHz) Antenna (left); Noggin (500 MHz) Antenna (right) [22]

The Survey

The GPR was then positioned and moved along grid lines. The grid location was referenced through the recording of coordinates relative to a fixed location. This was acted upon with extreme care to ensure the greatest possible accuracy. Care was taken to move the GPR along both T and L axes. The surface area of the structure surface used in the survey spanned approximately (3m x 2m) x 4 (Figure 6).

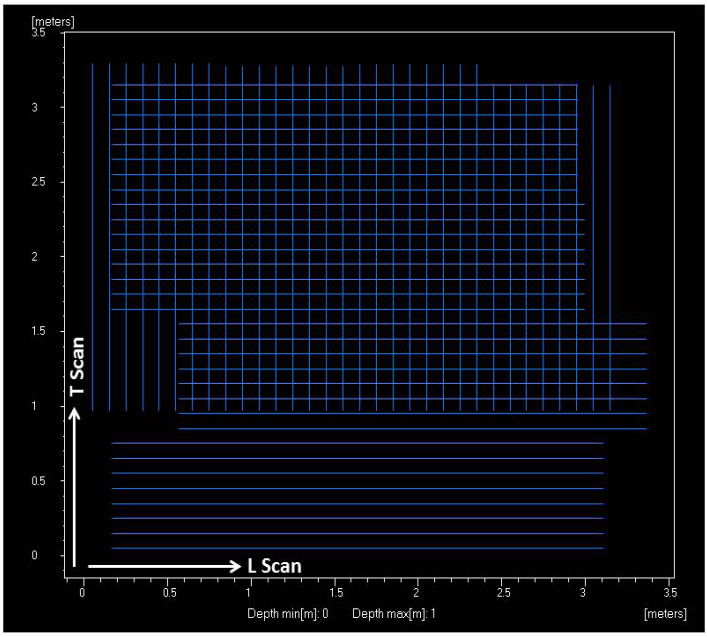

Figure 6. View of the survey area in a plan

RESULTS AND DATA PROCESSING

Data processing procedure

The data files derived from the survey were then processed using View data software provided by Conquest, which showed data in the form of 2D tomography of internal structure layers, along with 3D views of volume. The results derived from transversal and longitudinal axes were merged on the same tomographic plane to increase the reliability of results.

The analysis entailed filtering data, estimating the measure of the propagation's speed of EM waves over hyperbolic fitting, and finally, focusing. The shallower rebar layer was automatically extracted through the processed data sets. These sets also facilitated the examination of the backscattered sign of the rebar, and the guide removal of rebar at the shallower layers. The data derived from the GPR was processed and displayed as B-scan, representing a top-down view of the surveyed region.

The surface was divided into 4 interconnected zones in order to scale down the operation, and to increase the accuracy of results. Another reason for this division was to prevent disruption to the flow of traffic across the structure during testing. The suggested zone layout of the building for survey purposes is shown in Figure 7.

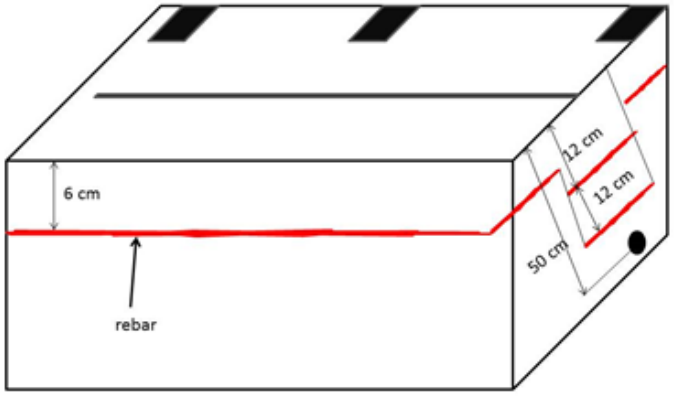

Figure 7. Cross section of the GPR survey

It is possible that the appearance of the highlighted characteristics was caused by moisture seeping through the surface. This can be attributed to the exterior cracks noticed during the initial visual examination of the structure. A recommendation made to the structure owners was that one of the highlighted areas should be exposed for the verification of the presence of moisture and concrete delamination in the lower part of the structure.

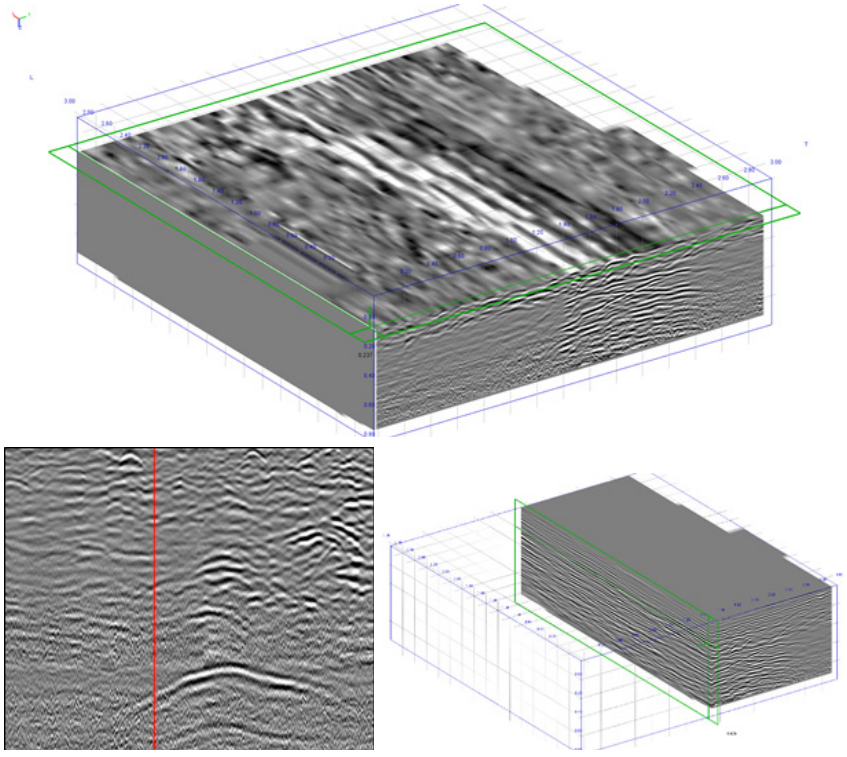

Figure 8. 3D and 2D GPR processed data

The above Figure 8 display the vertical sliced data derived from the surveyed area with 2GHz antennae from the surface to the surface. Notable features have been highlighted.

CONCLUSIONS

For the objectives of this study, it was necessary to gather and analyse a sizable amount of raw data from different GPR antennas applied to assess the depth position, rebar spacing, and shotcrete thickness. Both systems revealed two layers of rebar beneath the concrete cover layer, whose existence was not indicated in the accessible design drawings. Two separate antenna frequencies were employed to identify all the remains in order to maximize penetrative depth. Therefore it was possible to create a more detailed 3D visualization of the survey area using the GPR data. First time slices were used, however it was seen that these were insufficient to give a clear image to those unfamiliar with GPR images. It was therefore decided to use image processing to create a detailed image of the remains. Due to the scope and limitations of this study, it is not possible to display the complete data here. The data provided has been selected for its ability to show the effectiveness of GPR, as the preferred technique in structure analysis and inspection for defects which would otherwise be undetectable using other methods. In spite of this achievement, caution should be exercised in utilizing this antenna to locate lower-lying supports, due to its relative lack of penetrative depth compared to a lower-frequency antenna.

REFERENCES

[1] McCann D.M., Forde M.C., Review of NDT methods in the assessment of concrete and masonry structures, NDT & E International, Volume 34, Issue 2, 2001, Pages 71-84, ISSN 0963-8695, https://doi.org/10.1016/S0963-8695(00)00032-3

[2] Kilic G., Wavelet analysis and NDT for condition assessment of historic Masonry Bridge, Structures, Volume 45, 2022, Pages 275-283, ISSN 2352-0124, https://doi.org/10.1016/j.istruc.2022.09.008.

[3] Jol, H.M. (2009) Ground Penetrating Radar: Theory and Applications. Elsevier, Amsterdam, 509 p. Daniels D.J., Chapter 4 - Antennas, Editor(s): Harry M. Jol, Ground Penetrating Radar Theory and Applications, Elsevier, 2009, Pages 99-139, ISBN 9780444533487, https://doi.org/10.1016/B978-0-444-53348-7.00004-1.

[4] Kilic G., Eren L., Neural network based inspection of voids and karst conduits in hydro–electric power station tunnels using GPR, Journal of Applied Geophysics, Volume 151, 2018, Pages 194-204, ISSN 0926-9851, https://doi.org/10.1016/j.jappgeo.2018.02.026.

[5] Parrillo R. and Roberts R., "Tunnel Surface Condition Assessment using Ground Penetrating Radar", [ECNDT, 2006]

[6] Benmokrane B., El Salakawy E.F., El Ragaby A., Desgagné G. and Lackey T., "Design, construction and monitoring of four innovative concrete tunnel surfaces using non corrosive FRP composite bars", Proceedings on CD ROM, Annual Conference & Exhibition of the Transportation Association of Canada, Québec, September 19-22, 2004

[7] Rhazi J., Dous O., Ballivy G., Laurens S. and Balayssac J.P., "Non destructive health evaluation of concrete tunnel surfaces by GPR and half cell potential techniques", in Proceedings of 6th International Conference on Nondestructive Testing in Civil Engineering", Berlin, September 2003

[8] Lubowieckaa I., Armestob J., Arias P., Lorenzo H., "Historic tunnel modelling using laser scanning, ground penetrating radar and finite element methods in the context of structural dynamics" [Engineering Structures 31, 2009, p2667 2676]

[9] M. Scotta, A. Rezaizadeha, A. Delahazab, C.G. Santosc, M. Moored, B. Graybeale, G. Washerf, "A comparison of non-destructive evaluation methods for tunnel surface assessment", [NDT&E International 36, 2003, p245-255]

[10] F Soldovieri, R Persico, E Utsi, V Utsi, "The application of inverse scattering techniques with ground penetrating radar to the problem of rebar location in concrete" [NDT&E International 39, 2006, p602-607]

[11] N Fujun, L Zhanju, L Jiahao, L Hua, X Zhi-ying, "Characteristics of roadbed settlement in embankment-tunnel transition section along the Qinghai-Tibet Railway in permafrost regions" [Cold Regions Science and Technology 65, 2011, p437-445]

[12] S.M.B. Helwany, J.T.H. Wu, B Froess 1, "GRS tunnel abutments – an effective means to alleviate tunnel approach settlement" [Geotextiles and Geomembranes 21, 2003, p177-196]

[13] A. P. Annan, S.W. Cosway, and T. De Souza, "Application of GPR to map concrete to delineate embedded structural elements & defects", Ninth International Conference on Ground Penetrating Radar, Koppenjan, S.K., Lee, H., eds., [Vol. 4758, SPIE, Santa Barbara, 2002, p358-354]

[14] Dujardin J.-R., Bano M., Topographic migration of GPR data: Examples from Chad and Mongolia, Comptes Rendus Geoscience, Volume 345, Issue 2, 2013, Pages 73-80, ISSN 1631-0713, https://doi.org/10.1016/j.crte.2013.01.003.

[15] Ruffell A., Under-water Scene Investigation Using Ground Penetrating Radar (GPR) in the Search for a Sunken Jet ski, Northern Ireland, Science & Justice, Volume 46, Issue 4, 2006, Pages 221-230, ISSN 1355-0306, https://doi.org/10.1016/S1355-0306(06)71602-1.

[16] Tinelli C., Ribolini A., Bianucci G., Bini M., Landini W., Ground penetrating radar and palaeontology: The detection of sirenian fossil bones under a sunflower field in Tuscany (Italy), Comptes Rendus Palevol, Volume 11, Issue 6, 2012, Pages 445-454, ISSN 1631-0683, https://doi.org/10.1016/j.crpv.2012.04.002.

[17] Bano M., Loeffler O., Girard J.-F., Ground penetrating radar imaging and time-domain modelling of the infiltration of diesel fuel in a sandbox experiment, Comptes Rendus Geoscience, Volume 341, Issues 10–11, 2009, Pages 846-858, ISSN 1631-0713, https://doi.org/10.1016/j.crte.2009.08.002.

[18] Akarsu, G.; Taher, H.; Zengin, E.B.; Nakmouche, M.F.; Fawzy, D.E.; Allam, A.M.M.A.; Cleary, F., "Development of Ultra-Wideband Textile-Based Metamaterial Absorber for mm-wave Band Applications", 2022, 16TH European Conference On Antennas And Propagation (EUCAP), 2022, Madrid, Spain.

[19] Akarsu, G.; Nakmouche, M.F.; Fawzy, D.E.; Allam, A. M. M. A., "A Novel Ultra-Wideband Metamaterial-Based Perfect Absorber for 5G Millimeter-Wave Applications", 2022, 9TH International Conference on Electrical and Electronics Engineering (ICEEE 2022), Alanya – Turkey

[20] EUROGPR. www.eurogpr.org. 2010

[21] Kilic, G., (2012). "Application of advanced non-destructive testing methods on bridge health assessment and analysis." Thesis (PhD). University of Greenwich, London, UK.

[22] Kilic G., Unluturk M. S., 2016, Using Wavelet Analysis with Different Frequency GPR Antennas for Bridge Health Assessment, Journal of Testing and Evaluation, 0090-3973, DOI: 10.1520/JTE20140321

[23] HIGHWAYS AGENCY UK Highways Agency, design manual for roads and bridges, Part 7, BA86/06, Available: www.highways.gov.uk, 2011.

Chapter 5

UWB METAMATERIAL TEXTILE-BASED ABSORBERS FOR MM-WAVES APPLICATIONS

Diaa E. FAWZY[1], A.M.M.A. ALLAM[2], Gokhan KILIC[3]

1 Izmir University of Economics, Faculty of Engineering, Department of Aerospace Engineering, Izmir, Türkiye
2 German University in Cairo, Faculty of Engineering, Department of Electrical and Telecommunication Engineering, Cairo, Egypt.
3 Izmir University of Economics, Engineering Faculty, Civil Engineering Department, Izmir, Türkiye

INTRODUCTION

Perfect electromagnetic (EM) wave's absorbers are the main components in many developments. For example EM energy harvesting systems rely on perfect absorbers in a specified frequency range. Wearable applications based on smart textiles also require the development of perfect absorbers [1]. These requirements can be met by employing metamaterials (MM) and taking advantage of their numerous applications at various operating frequencies.

MMs are artificially engineered materials formed by combining conductive resonant cells arranged in periodic or aperiodic geometries [2]. MMs with their extraordinary capabilities have emerged as candidates for the development of perfect absorbers [3, 4]. However, up to now most of the suggested studies and designs of metamaterial absorbers (MMA) are not fulfilling the needs for the aforementioned applications in terms of the operation bandwidth, compactness, stability, lightness, size, absorption rate, cost, ease of manufacture and flexibility in integration.

Smart textiles or electronic textiles are fabrics that allow electronic system components such as sensors, antennas, and electric circuits to be integrated within their structures. They are being used in many new developments, such as smart clothing, wearable health monitoring technologies, and wearable computing projects [5]. Passive and active system components can be easily implemented within the structure of the textile substrates. For example, electronics such as diodes, and solar cells, conductors and resistors or transistors can be merged within the structure [6]. Possible applications include health monitoring, smart cars, energy harvesting, and military protective clothing, antennas, sensors, wireless power transfer and electromagnetic cloaking [7-12].

The flexibility offered by smart textiles in terms of low profile, lightweight, and easy integration presents an opportunity to design competitive systems and especially electromagnetic absorbers. Recently obtained results of textile-based absorbers play an important role in the development of future systems.

The aims of the current study are three folds: (1) to review and compare our developed MMS based on symmetric and asymmetric cells in terms of bandwidth and absorptivity rates, (2) to compare the behavior of metamaterials absorbers on different PCB- and textile- based materials, (3) presenting a technique for bandwidth enhancement of narrow band metamaterials with the use of lumped elements approach.

In section 2, the theoretical background of metamaterials is illustrated. In section 3, the designs of different MMA cells are presented. Section 4 focuses on the obtained results and the analysis of the proposed designs. Section 5 concludes the current work.

THEORETICAL BACKGROUND

MMs can be classified into four different groups according to their permittivity and permeability values as shown in Fig. 1. The MM effective medium is characterized by a complex permittivity ε and magnetic permeability μ as given by Eqs. 1-2. The permittivity and permeability define the refractive index of the material *n*, the characteristic impedance η, and the wave number *k* as given in Eqs. 3-5.

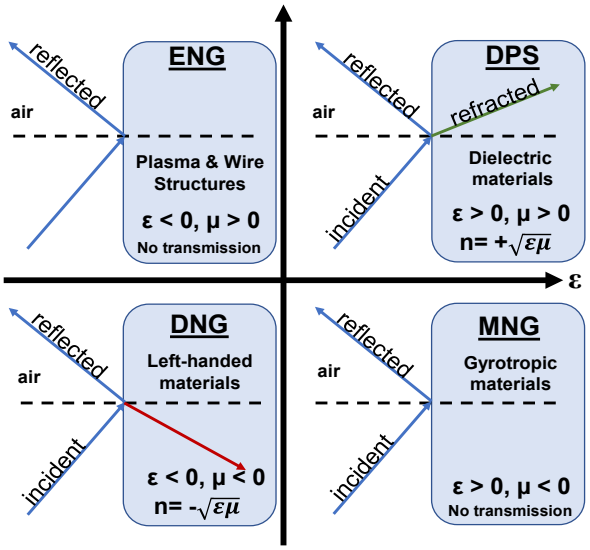

Figure 1. Electric and magnetic classification of materials Source [13]

$$\varepsilon(w) = \varepsilon_1 + j\,\varepsilon_2 \quad (1)$$

$$\mu(w) = \mu_1 + j\,\mu_2 \quad (2)$$

$$\mathrm{n} = \pm\sqrt{\varepsilon\mu} \quad (3)$$

$$\eta = \sqrt{\frac{\mu}{\varepsilon}} \quad (4)$$

$$k = k_0\sqrt{\varepsilon\mu} \quad (5)$$

where ε_1 and μ_1 ,k_0 are the real components of the permittivity, permeability, and the free-space wave number, respectively. The values ε_2 and μ_2 correspond to the imaginary parts, they define the dielectric losses of energies. Both, the permittivity and permeability are functions of the frequency w. The dielectric losses are increasing with the increase in the frequency w. It is important to note that, the signs of the real values ε_1 and μ_1 indicate whether the metamaterials are left-handed or right-handed material [14].

Materials with positive permittivity and permeability values ($\varepsilon_1 > 0$, $\mu_1 > 0$) are considered as double-positive (DPS) materials. Materials with permittivity values less than zero and permeability value greater than zero ($\varepsilon_1 < 0$, $\mu_1 > 0$) are termed as epsilon negative (ENG) metamaterials. Materials with permittivity value greater

than zero and permeability values less than zero ($\varepsilon_1 > 0$, $\mu_1 < 0$) are termed as mu-negative (MNG) metamaterials. As aforementioned, materials with both negative electric permittivity and magnetic permeability are termed as double-negative (DNG) metamaterials. Natural materials cannot exhibit both negative permeability and permittivity values and this class is only possible with artificially tailored engineering methods. Silver, gold, and aluminum display negative ε_1 only and resonant ferromagnetic systems display negative μ_1 at optical frequencies with narrow bandwidths.

The first ENG materials at the microwave frequencies were experimentally verified by J. Pendry and his colleagues [15]. They periodically placed an array of thin wires with radius r and a unit cell side length a. Furthermore, they explained that if the incident electromagnetic wave's wavelength coming through the structure is larger than the unit cell side length ($\lambda >> a$), where the behavior of the material gains its properties from the developed structure not from the constituent materials. Electromagnetic waves can be manipulated by adjusting the cell geometry, size, orientation and distribution. With these parameters, extraordinary behaviors can be developed, for example, perfect absorbers, perfect reflectors or perfect transmitters.

The performance of the MM absorber is subjected to the incoming plane waves and their divisions into reflection, transmission and absorption coefficients. A MM structure of periodically arranged metallic elements is responsible to provide the Ohmic losses for an effective medium that matches the impedance of the free space. In addition, traditional bulky absorbers prevent the transmission of electromagnetic waves, they either absorb or reflect waves. On contrary, MM with a ground load behaves as an absorber or reflector or transmitter based on the frequency of operation and the equivalent circuit of the unit cell of its structure.

The EM absorption rate is related to the reflection and transmission coefficients as given by Eq. 6. The absorption rate $A(\omega)$ is computed as:

$$A(\omega) = 1 - R(\omega) - T(\omega) = 1 - |S_{11}|^2 - |S_{21}|^2 \quad (6)$$

where, $R(\omega) = (|S_{11}|^2)$ and $T(\omega) = (|S_{21}|^2)$ represent the power reflection and transmission coefficients. If the reflection coefficient and transmission coefficient are equal or close to zero, the absorption rate will be very close to 100%.

PROPOSED DESIGNS

The current work is based on previously developed designs by Akarsu 2022 [13]. Several PCB- and textile-based MMAs are proposed and discussed for UWB applications. For the sake of detailed comparison, we consider both symmetric and asymmetric unit cell geometries.

Symmetric Cell Geometries

Textile-based absorbers are suggested and optimized for energy harvesting applications in the frequency range from 16.4 GHz to 22.6 GHz. The design consists

of a top ground layer of Copper annealed, a felt dielectric layer and beneath it a ground layer. On the top of the substrate, the Copper is etched to form an air-filled structure of two resonators, the first resonator is a Jerusalem cross surrounded with a second square ring resonator as shown in Fig. 2 with the parameters listed in table 1.

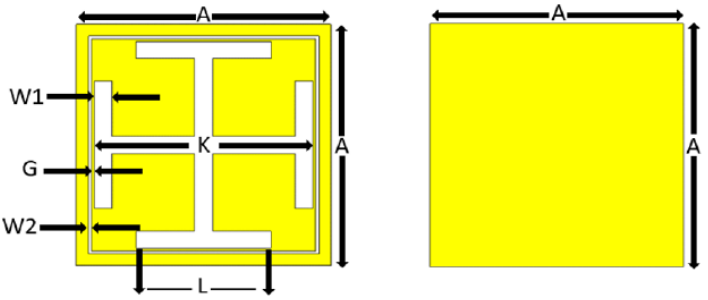

Figure. 2. The proposed unit cell (a) front view (b) back view

Table 1. Dimensions of the cell design

Parameter	A	K	L	W1	W2	G
Value (mm)	17	14.6	9	1.2	0.2	0.2

Asymmetric Geometries

In this part, an asymmetric MMA's unit cell as taken from [13] is considered and used for a comparison with other designs. The cell design is depicted in Fig. 3 and the parameters are listed in Table. 2. Maximum electromagnetic wave absorption rates can be achieved when the impedance of the developed MMA structure is perfectly matched with that of the free space. The reflection coefficients and the absorption rates are computed according to Eq. 3. The design of the unit cell consists of three layers of an optimized geometry of patch structure; a substrate layer is placed between the patch and the ground layer. The ground layer is Copper with a thickness of 0.04 mm and with a conductivity value of 5.96 x10^7 S/m.

In this study, the following different substrates are considered with the following physical properties:

(1) PCB-based FR-4 with a thickness of 1.2 mm, a relative dielectric constant of ε_r = 4.4, and a dielectric loss tangent of tan δ = 0.02.

(2) Rogers RT5880 substrate with a thickness of 1.575 mm, a relative dielectric constant of ε_r = 2.2 with a dielectric loss tangent of tan δ= 0.0009.

(3) Three different textile fabrics, namely, Felt (ε_r =1.22,*tan* δ= 0.016), Denim (ε_r =1.7,*tan* δ= 0.025), and Polyster (ε_r = 1.9,*tan* δ= 0.0045).

The unit cell of the design is depicted in Fig. 3 and the optimized design parameters are listed in Table 2. The Finite Difference Time Domain (FDTD) method

is employed to perform the numerical plane wave simulation and the optimization for the considered designs.

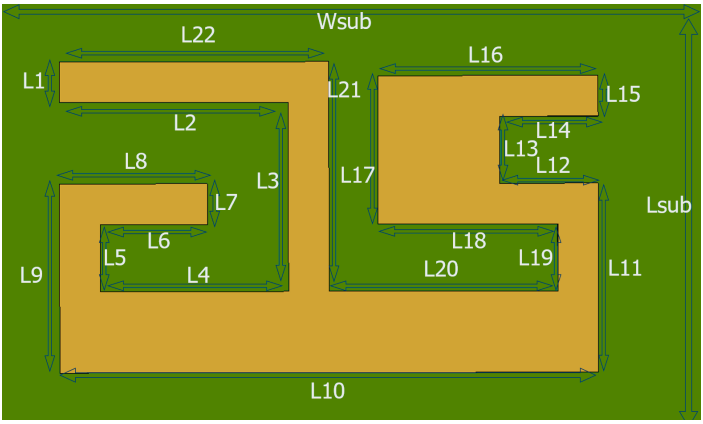

Figure 3. The proposed G&S MMA design

Table 2. The optimized design parameters of the design

Parameter Name	**L1**	**L2**	**L3**	**L4**	**L5**
value (mm)	0.26	1.46	1.20	1.20	0.43
Parameter Name	**L6**	**L7**	**L8**	**L9**	**L10**
value (mm)	0.69	0.26	0.94	1.20	3.44
Parameter Name	**L11**	**L12**	**L13**	**L14**	**L15**
value (mm)	1.20	0.63	0.43	0.63	0.26
Parameter Name	**L16**	**L17**	**L18**	**L19**	**L20**
value (mm)	1.41	0.94	1.15	0.43	1.46
Parameters	**L21**	**L22**	**Wsub**	**Lsub**	**Hsub**
Value (mm)	1.461	1.719	4.540	2.771	1.575

Bandwidth Enhancements

It is widely accepted that symmetric unit cells resonate within narrow band ranges but they are easier to fabricate and reproduce in addition to their good efficiencies at different polarization angles and different angles of incidence [16, 17] compared to the asymmetric designs.

Akarsu [13] has developed a symmetric unit cell-based metamaterial absorber for mm-wave applications. The geometry of the unit cell is developed by combining symmetrical octagonal cut rings and octagonal ring patch geometry printed on a 10 x 10 mm grounded layer with a Rogers RT5880 substrate (relative permittivity $\varepsilon_r \varepsilon_r$ = 2.2 and dielectric loss tangent of tan δ = 0.0009). The copper layer has a 0.035 mm thickness and conductivity of 5.96 x 10^7 S/m. The enhancement of the absorption bandwidth of the MMA design is achieved by the use of a technique based on lumped elements. The proposed MMA design can be seen in Fig 4 with the dimensions listed in Table 3.

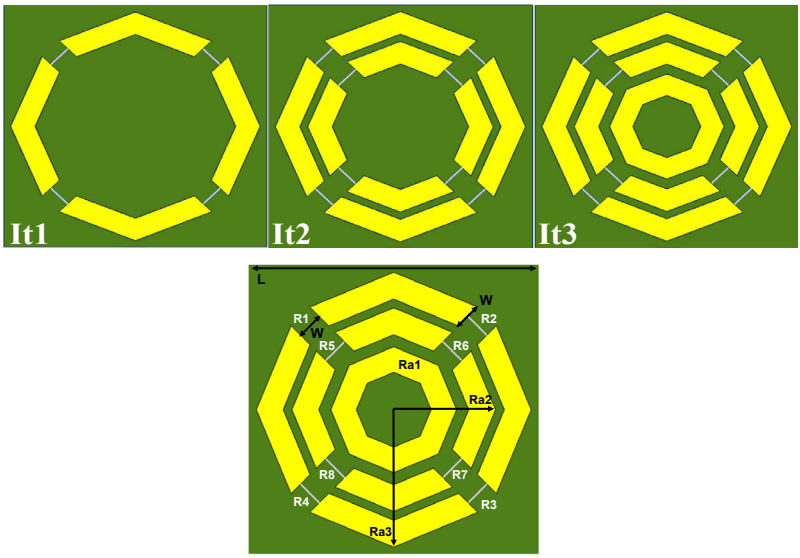

Figure 4. The developed octagonal absorber. Design iterations (top) and the final design iteration with parameters (bottom)

Table 3. Dimensions of the proposed octagonal MMA.

Parameters	Ra1	Ra2	Ra3	W	L
Value (mm)	2.161	3.500	4.725	0.919	10.000

RESULTS AND DISCUSSIONS

Symmetric Cell Geometry

This section is devoted to exploring the results for the symmetric design as depicted in Fig. 2. As shown in Fig. 5, maximum absorption rates are achieved at three different frequency bands, namely, (16.54-17) GHz, (18.36-18.85) GHz and (22.32-22.6) GHz. The absorption rates are about 99.8%, 96.5, and 99.7% at 16.7 GHz, 18.6 GHz, and 22.4 GHz, respectively. The developed absorber is designed on Felt material and is very suitable for integration into wearable applications. It is important to note here that the obtained absorption bandwidth is not as wide as that obtained from asymmetric cell geometries.

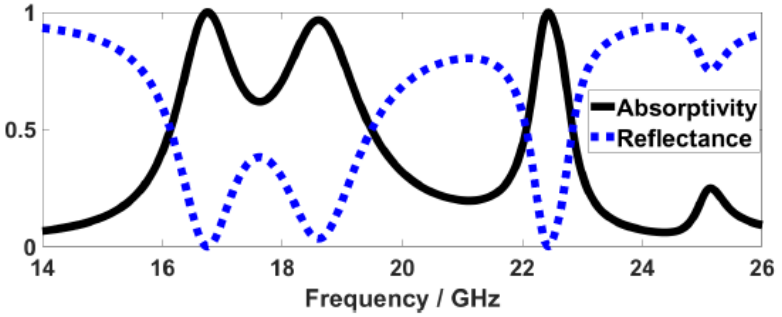

Figure 5. Absorptivity and reflectivity of the proposed cell

Asymmetric Cell Geometry

Concerning the asymmetric absorbers depicted in Fig. 3, the responses of different textile-based fabrics are shown in Fig. 6. The reflections and normalised absorptions are presented. The obtained absorption bandwidths from all fabrics are the ultra-wideband. The obtained fractional bandwidths of the three Fabrics are 42.834%, 43.65%, 42.828% for Polyester, Denim and Felt, respectively.

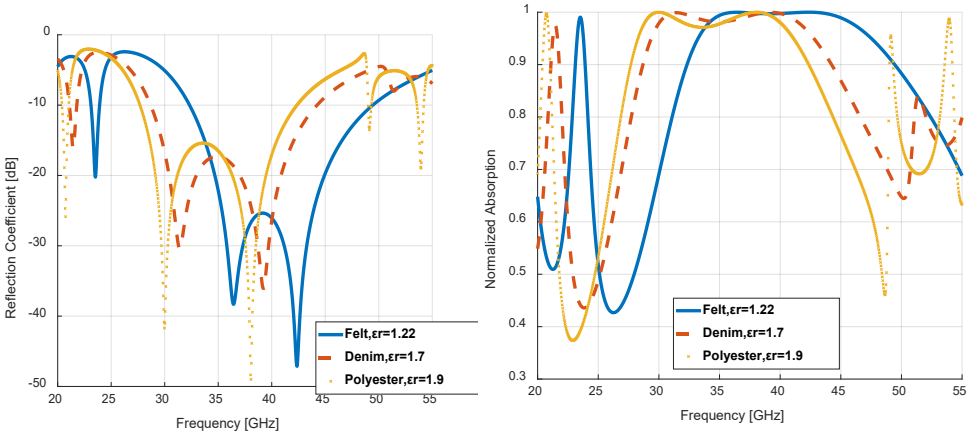

Figure 6. The reflection coefficients (left) and normalized absorption rates (right) of different textile Fabrics [13]

A comparison with other studies as shown in Table 4 depicts that the asymmetric cell-based designs on Felt fabric can achieve an absorption fractional bandwidth of about 43%. In addition, the current design is more compact in size and the average absorption rates reach about 99%.

It can be shown that asymmetric cell geometries can offer a more compact size. The currently optimized geometry offers about 2.77 wider bandwidth compared to the design in the first study and about 13.34 times wider bandwidth in comparison to the second study as listed in table 4.

Table 4. A comparison with related previous studies for the Felt material.

Frequency Band (GHz)	Absorption Fractional Bandwidth	Absorptivity (%)	Unit Cell Size (mm^3)	References
9.00–10.50	15.43 %	≈ 90	30 x 30 x 1.0	[18]
4.90 -5.06	3.21 %	≈ 99	18 x 18 x 2.0	[19]
23.11-23.92 32.32-49.44	3.44 % & 42.828 %	≈ 99	4.5 x 2.7 x 1.0	Current Design

Moreover, different substrate types are considered in the current work, namely, conventional rigid PCB-based and textile-based MMA. Table 5 illustrates a comparison between traditional PCBs (FR-+ and RT-5880) and a Felt material as a textile fabric.

Table 5. Absorption bandwidth, absorptivity rates, cell size and substrate thickness for different dielectric materials.

Substrate	Resonance Frequency (GHz)	Absorption Fractional Bandwidth	Absorption rates (%)	Cell Size (mm^2)	Substrate Thickness (mm)
FR-4	18-26	36.36 %	≈ 96	4.5x2.7	1.2
RT-5880	21-30	35.29 %	≈ 99	4.5x2.7	1.575
FELT	32.32-49.44	41.87 %	≈ 99	4.5x2.7	1.0

The obtained fractional bandwidths from the three different dielectric materials are 36.4%, 35.30%, 41.87% for FR-4, Rogers RT5880 and Felt, respectively. It is clearly seen that all substrates are wideband, this is due to the fact that the cell geometry is asymmetric. The Felt fabric provides an ultra-wideband feature compared to other dielectrics. As stated in Table 5, average absorption rates of about 99% are achieved with the Rogers and Felt substrates while for the FR-4 substrate, an average value of 96 % is obtained. This is due to the higher dielectric losses of the FR-4 material. But it is important to indicate that even with a thin structure of Felt, the achieved absorption bandwidth is higher than others. With the target to achieve stable absorptivity rates and common bandwidth over different angles of incidence. The reaction of one of the developed designs (asymmetric design) is examined against oblique angles range in the range of θ = 0°-15°-30°. In this part. As shown below in Fig. 7, the increase in incident angles affects the reflection coefficients and average absorption rates.

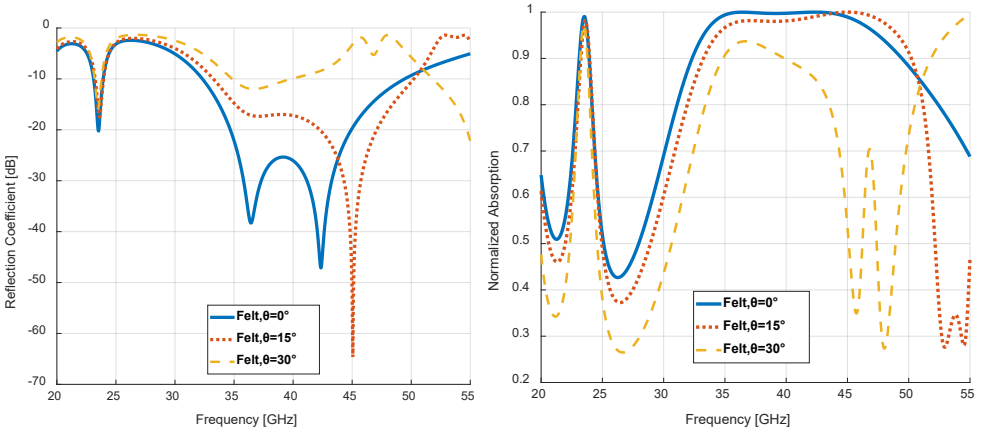

Figure 7. The effect of the incident angles on the reflection coefficients (left) and normalized absorption rates (right) for a textile-based G&S MMA

The average absorption rate is about 99% for an incident angle of θ = 0°. The absorption rates are slightly decreasing but still above 95% for incident angles in the range between θ = 0 – 15 degrees. A noticeable decrease is obtained for an angle

of 30°. It is important to note that a common bandwidth of approximately 5 GHz is achieved with an average absorptivity rate of about 95%.

Bandwidth Enhancement of Symmetric Design

For the case of bandwidth enhancement of a symmetrical unit cell as depicted in Fig. 4, the computed reflection and absorption coefficients are illustrated in Fig. 8. Two cases are considered for a textile material with and without lumped resistors. As shown in Table 6, one can achieve a noteworthy enhancement in the absorption rate and the bandwidth of symmetric cell geometries by the use of lumped elements. A Parametric sweep of the resistive values showed that values of R1 = R2 = R3 = R4 = 220 Ω and R5=R6=R7=R8 = 370 Ω are optimal to achieve the widest band width with maximum absorption rates. The use of lumped resistors enhances the fractional bandwidth by a factor of about 187. The consideration of resistive lumped elements also increases the absorption rates to values on the average of about 98%. The proposed approach is vital for much structural health monitoring and inspection applications [20, 21].

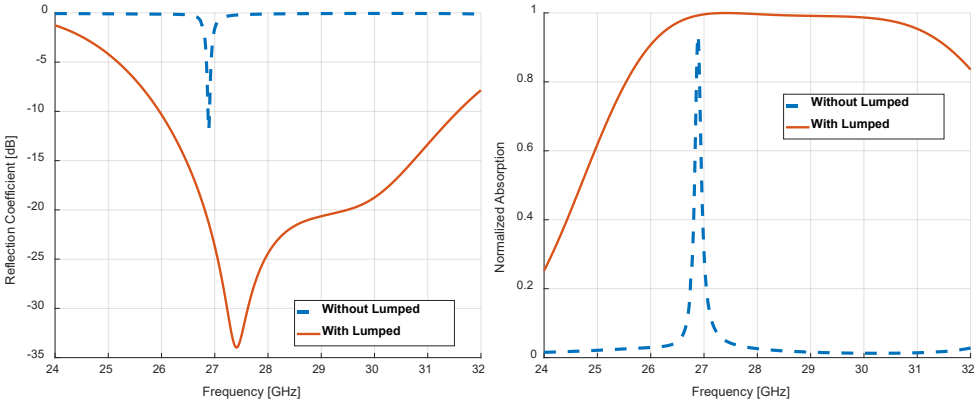

Figure 8. Reflection coefficients (left) and normalized absorption rates (right) of an MMA with and without consideration of lumped elements [8].

Table 6. The fractional bandwidth, absorptivity rates and unit cell size of an MMA with and without consideration of lumped elements [8].

MMA Type	Frequency Range (GHz)	Fractional Bandwidth	Absorptivity (%)	Unit Cell Size (mm^3)
Without Lumped	26.872-26.90	0.104 %	≈ 93.5	10 x 10 x 1.575
With Lumped	25.959-31.57	19.50 %	≈ 98	10 x 10 x 1.575

CONCLUSIONS

Different MMA absorbers are developed based on PCB- and textile dielectrics for 5G and mm-wave applications. Different cell geometries are considered, they are mainly symmetric and asymmetric in shape. Moreover, the effect of the angle of incidence of the upcoming plane wave is considered. The design parameters are

optimized for maximum absorptivity rates and maximum bandwidths. The following points conclude our study:

- Asymmetric textile-based designs have been shown to possess the widest bandwidth property with average absorptivity rates of around 98%. The achieved -10 dB reflective fractional bandwidths are about 42.828%, 43.65%, and 42.834% for Felt, Denim and Polyester, respectively.
- A symmetric design based on Jerusalem cross and square ring exhibit three resonance bands, (16.54-17) GHz, (18.36-18.85) GHz and (22.32-22.6) GHz. The achieved absorption peaks are 99.8%, 96.5% and 99.7%, respectively.
- The narrow bandwidths of symmetric cell geometries can be enhanced in terms of absorption bandwidths and rates by the use of lumped elements. Nearly a factor of 187 increase in the fractional bandwidth is obtained with average absorption rates of about 98%.
- The effect of the angle of incidence on the MMA absorption rates is studied for the asymmetric design. The absorption rates are on average around 99% for incident angle $\theta = 0^{o}$. A common bandwidth of approximately 5 GHz is achieved with an average absorptivity rate is about 95%.

REFERENCES

[1] Yu, L., Yu, L., Dong, Y. et al., Compressible polypyrrole aerogel as a lightweight and wideband electromagnetic microwave absorber, Journal of Materials Science: Materials in Electronics volume 30, pages5598–5608, 2019. https://doi.org/10.1007/s10854-019-00853-9

[2] Cui, T. J. ,"Microwave metamaterials", Natl. Sci. Rev. 5, 134–136, 2018.

[3] Akarsu, G.; Taher, H.; Zengin, E.B.; Nakmouche, M.F.; Fawzy, D.E.; Allam, A.M.M.A.; Cleary, F., "Development of Ultra-Wideband Textile-Based Metamaterial Absorber for mm-wave Band Applications", 2022, 16TH European Conference on Antennas And Propagation (EUCAP), 2022, Madrid, Spain.

[4] Akarsu, G.; Nakmouche, M.F.; Fawzy, D.E.; Allam, A. M. M. A., "A Novel Ultra-Wideband Metamaterial-Based Perfect Absorber for 5G Millimeter-Wave Applications", 2022, 9TH International Conference on Electrical and Electronics Engineering (ICEEE 2022), Alanya – Turkey

[5] Cherenack, Kunigunde; Pieterson, Liesbeth van (2012-11-01). "Smart textiles: Challenges and opportunities" (PDF). Journal of Applied Physics (published 7 November 2012). 112 (9): 091301–091301–14. Bibcode:2012JAP...112i1301C. doi:10.1063/1.4742728. ISSN 0021-8979. S2CID 120207160. Archived from the original (PDF) on 2020-02-13

[6] Weng, W., Chen, P., He, S., Sun, X., & Peng, H. (2016). Smart electronic textiles. Angewandte Chemie International Edition, 55(21), 6140-6169.https://doi.org/10.1002/anie.201507333

[7] Lund, A., Wu, Y., Fenech-Salerno, B., Torrisi, F., Carmichael, T. B., & Müller, C. (2021). Conducting materials as building blocks for electronic textiles. MRS Bulletin, 1-11. https://doi.org/10.1557/s43577-021-00117-0

[8] Almoneef, T.S. and Ramahi, O.M. (2013), Harvesting electromagnetic energy using metamaterial particles, IEEE Antennas and Propagation Society, AP-S International Symposium (Digest), IEEE, pp. 1046–1047.

[9] Amer, A.A.G., Sapuan, S.Z., Nasimuddin, N., Alphones, A. and Zinal, N.B. (2020), A comprehensive review of metasurface structures suitable for RF energy harvesting, IEEE Access, Vol. 8, pp. 76433–76452.

[10] Chambers, B. and Tennant, A. (2006), Active Dallenbach radar absorber, 2006 IEEE Antennas and Propagation Society International Symposium, IEEE, pp. 381–384.

[11] Chen, T., Li, S. and Sun, H. (2012), Metamaterials application in sensing, Sensors, Vol. 12, No. 3, pp. 2742–2765.

[12] Cheng, Y.Z., Fang, C., Zhang, Z., Wang, B., Chen, J. and Gong, R.Z. (2016), A compact and polarization-insensitive perfect metamaterial absorber for electromagnetic energy harvesting application, 2016 Progress in Electromagnetics Research Symposium, PIERS 2016 - Proceedings, IEEE, Vol. 1, pp. 1910–1914.

[13] Akarsu, G., Master Thesis, 2022, the Izmir University of Economics., Turkey

[14] Smith, D. R., et al. "Determination of Effective Permittivity and Permeability of Metamaterials from Reflection and Transmission Coefficients." Physical Review B, vol. 65, no. 19, 2002.

[15] Pendry, J.B., Holden, A.J., Robbins, D.J. and Stewart, W.J. (1998), "Low-frequency plasmons in thin-wire structures", Journal of Physics Condensed Matter, Vol. 10, No. 22, pp. 4785–4809.

[16] Huang, C. Lu, C. Rong, Z. Hu and M. Liu, "Multiband Ultrathin Polarization-Insensitive Terahertz Perfect Absorbers With Complementary Metamaterial and Resonator Based on High-Order Electric and Magnetic Resonances," in IEEE Photonics Journal, vol. 10, no. 6, pp. 1-11, Dec. 2018, Art no. 4600811.

[17] S. R. Thummaluru, N. Mishra and R. K. Chaudhary, "Design of double negative ultrathin metamaterial absorber using an array of electric field resonators," 2016 11th International Conference on Industrial and Information Systems (ICIIS), 2016, pp. 182-184.

[18] Tak, J. and Choi, J. (2017), A Wearable Metamaterial Microwave Absorber, IEEE Antennas and Wireless Propagation Letters, IEEE, Vol. 16, pp. 784–787.

[19] Bait-Suwailam, M.M., Almoneef, T.S. and Alomainy, A. (2019), A wearable reconfigurable electromagnetic metamaterial absorber using artificial magnetic inclusions, 2019 IEEE International Symposium on Antennas and Propagation and USNC-URSI Radio Science Meeting, APSURSI 2019 - Proceedings, Vol. 1, pp. 1623–1624.

[20] Kilic G., Wavelet analysis and NDT for condition assessment of historic Masonry Bridge, Structures, Volume 45, 2022, Pages 275-283, ISSN 2352-0124, https://doi.org/10.1016/j.istruc.2022.09.008.

[21] Kilic G., Eren L., Neural network-based inspection of voids and karst conduits in hydroelectric power station tunnels using GPR, Journal of Applied Geophysics, Volume 151, 2018, Pages 194-204, ISSN 0926-9851, https://doi.org/10.1016/j.jappgeo.2018.02.026.

Chapter 6

INVESTIGATION OF THE EFFECTS OF ELECTRICAL VEHICLE CHARGING STATIONS ON POWER SYSTEMS AND INTEGRATION OF PV+ESSs

Fatma YAPRAKDAL[1], Omer Ramazan TASKIN[2], Gulhan TASKIN[3]

1 Kirklareli University, Engineering Faculty, Electrical and Electronics Engineering Department, Kirklareli, Türkiye
2 Kirklareli University, Graduate School of Science and Engineering, Electrical and Electronics Engineering Department, Kirklareli, Türkiye
3 Kirklareli University, Graduate School of Science and Engineering, Electrical and Electronics Engineering Department, Kirklareli, Türkiye

INTRODUCTION

As the living standards of human beings increase with the developing technology in our world, an increase is observed in the damage to nature. The most obvious consequences of this are global warming, air pollution in big cities, pollution of groundwater, etc. Mankind has identified this damage to increase the level of welfare and has developed approaches to protect nature, especially in recent years. Undoubtedly, one of the most important basic needs of human beings is energy. Various types of energy are needed for many actions such as the operation of machines, heating of houses, and lighting of streets. Electrical energy is indispensable for our age. Fossil fuels have been used for centuries to obtain electrical energy, and a negative result has been encountered, leading to global warming. Studies have shown that carbon emissions do not occur only during energy production. Billions of internal combustion and fossil fuel-powered vehicles in the world emit carbon to nature. In [1], the consequences of fuel use and the effects of CO2 emissions on the environment have been evaluated in detail.

The fossil fuel reserves in the world are rapidly depleting and the number of internal combustion engine vehicles continues to increase with the increasing world population. With this increasing number of vehicles, serious risks have emerged, especially in terms of the environment. According to the study by [2], considering passenger cars in China, the level of greenhouse gases emitted from internal combustion engines will increase to 810 megatons of carbon dioxide (CO2) by 2027.

Researchers have researched the types of vehicles that can replace fossil fuel vehicles by revealing the harms of fossil fuel vehicles to the environment. According to current technology and economic parameters, it has been seen that the most suitable vehicle model is electric vehicles (EVs). With the focus on electric vehicles, it was necessary to produce many technologies in this field. Based on this, some studies have been conducted on the safety of electric vehicles, including better acceleration and braking, driver safety, comfort, and reduced power usage [3]. The use of EVs, whose price has decreased with the developing technology, has become widespread in many countries. For example, the EVs vehicle market has already reached 28.8% in Norway, 6.4% in the Netherlands, and 1.4% in China [4].

Net CO2 emissions are decreasing as the transition from internal combustion engines to EVs accelerates. In addition, with the replacement of internal combustion fossil fuel vehicles by EVs, the number of nitrogen oxides released into the environment will decrease [5]. According to Michaelides' study [6], it is estimated that the average CO2 avoidance will be around 16,24% in the whole world with the transition to EVs under current conditions.

The spread of EVs is especially encouraged by developed countries. However, considering the economic indicators and charging station infrastructures in

developing countries, it is seen that there are some obstacles in front of the transition to EVs. Some regulations have been published in developing countries to accelerate the transition to EVs and to remove the barriers to the spread of EVs. The price tariffs to be applied for EV charging are also an issue that supports the spread of EVs and needs to be emphasized. Supportive charging tariffs will minimize refueling and grid retrofit costs [7]. However, it is important to determine a suitable charging station location to address the concerns of EV users about charging and range [8].

In the positioning of charging stations; Considering the behavior of EV users, it should be aimed to reduce the total construction cost, eliminate the range anxiety of EV users, and reduce the amount of energy consumed on the road by shortening the road to the charging station [9].

With the significant increase in the EV market, the amount of greenhouse gases decreases, but the amount of energy demanded from the grid increases at the same rate. The proliferation of EVs will have a greater impact on the electricity grid, the environment, and the economy [10]. Charging stations established for the charging of EVs cause problems such as voltage fluctuations in the electricity distribution network, problems in peak time, increases in power losses, and transformer loading [11]. The widespread use of EVs provides a reduction in CO2 emissions and more environmentally friendly urbanization. However, the reduction of internal combustion vehicles on highways alone is not sufficient to reduce CO2 emissions, and the electricity grid, where the energy demand of EVs, which replace fossil fuel vehicles, is met, must be fed from renewable energy sources [12]. The photovoltaic (PV) systems that are foreseen to be used in charging stations support the grid by meeting some of the load demanded by the charging units, especially during the hours when solar radiation is high [13]. A case study by Mowry and Mallapragada for 2033 and 3 million EV users in [14] revealed that the system increased the annual operating cost by 8% or $2 per MWh. It has been observed that energy storage systems (ESSs) reduce these costs. The energy produced from PV systems not only supports ESSs but also significantly reduces the cost of charging at charging stations [15]. Today, due to the high costs of ESSs, integration into charging stations is not economically preferred. When the efficiency of electric vehicle batteries decreases, they can be designed to be used as second-life batteries in ESSs. Research on this subject has shown that the use of low-efficiency EV batteries in ESSs has reduced the installation costs of ESSs. Thus, within the framework of the Kyoto protocol, the CO2 footprint is reduced and its waste is prevented. Some EV companies have adopted this practice. Some of these companies are Nissan, Renault, and BMW [16]. The use of retired EV batteries in storage systems will prevent new battery demands. According to a Chinese-scale study by Geng et al. in [17], more than 16 TWh of Li-ion batteries are expected to be retired from EVs by 2050. A 73-100% reduction in new battery demand can be achieved in different scenarios as a result of the second use of these out-of-use batteries in storage systems.

In the second part of this study, which focuses on the effect of electric vehicle charging stations (EVCSs), which is a new field and has many effects on society, on the electricity distribution network, basic information about EVCSs will be given. In Section 3, the negative effects of EVCSs on the electricity distribution network will be discussed. In Section 4, it will be discussed to what extent and how the Photovoltaic system and energy storage systems (PV+ESSs) integrated into EVCSs play a corrective role in the negative effects of EVCSs in the electricity distribution network.

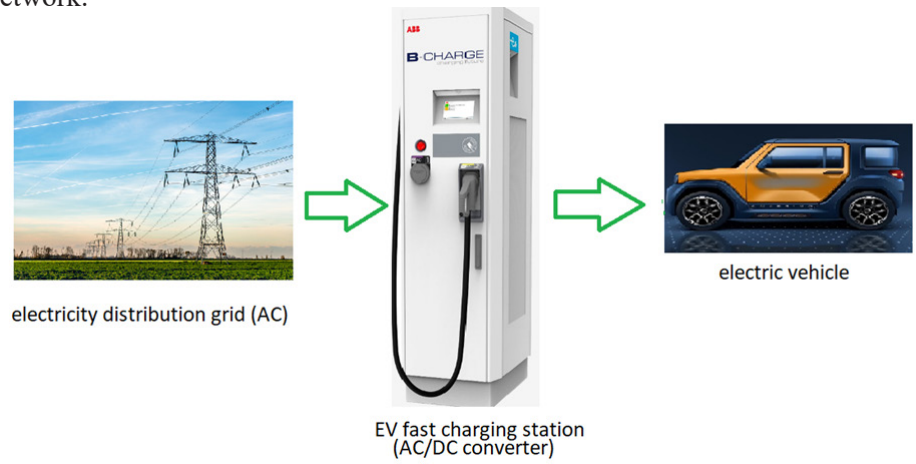

Figure 1. EV fast charging station model

DC charging units, on the other hand, are expected to be used mostly in public areas and are produced for commercial purposes and are defined as fast charging by vehicle users. DC charging units, which are defined as fast charging with the developing technology, can charge an electric vehicle in less than 20 minutes [18]. Current charging power and time information of fast charging stations are given in Table 1.

Table 1. Basic technical information about the EV fast charging station from the ABB catalog [19]

Station Type	Power	Time
AC Type-2	3-22 kW	4-20 h
DC	20-25 kW	1-4 h
DC Fast	50 kW	20-90 min.
DC High Power	150-350 kW+	5-30 min.

Considering the economic conditions, it may be possible to expand electric vehicle charging stations in three stages. To encourage the charging of vehicles at night when the mains electricity price is low, by using the existing infrastructure in the house with a first-phase domestic charging station. In parallel with the significant increase in the number of second-phase EVs, it is recommended to commission public and smart charging stations. It is essential that investors who will install

charging stations be supported with incentives in the transition to the second phase. In the third stage, a system can be established in which more controllable vehicle fleets are included and this is an application that can be done in the long term [20].

According to the study by Lim et al. in [21], since AC-level charging stations will generally become widespread in detached houses, DC-level charging stations are expected to be used on highways when user behaviors and urban planning are taken into account. However, 10% of the energy cost used in charging EVs with increased battery capacities and extended range is expected to be met only from fast charging stations on these highways. For this reason, governments should plan incentives for the expansion of DC-level fast charging stations.

EV driver behaviors are taken into account in the design of fast charging stations. In a study by Zhou et al. in Beijing on the scale of passenger electric vehicles in [22], the profile of the energy demand from the electricity distribution network was simulated in parallel with the frequency of use of a charging station in 24 hours. According to this, between 09:00 and 16:00, the charging station shows the highest demand power, and between 03:00 and 06:00 the lowest demand power. The peak usage time of the charging station and the peak energy consumption is at 13:00.

It should also be considered whether renewable energy sources or ESSs will be used in the design of the charging station. Rapid charging station design and storage systems including renewable energy sources can be realized by using a Genetic Algorithm (GA) [23]. Similarly, optimal placement and sizing of Renewable Energy Sources and EVCSs can be done using hybrid optimization techniques such as Genetic Algorithm-Particle Swarm Optimization (PSO) [24].

EFFECTS OF EV CHARGING STATIONS ON POWER SYSTEMS

EVs are charged with alternating current and direct current charging units. Since AC charging units appeal to individual users, they do not affect the electricity grid as much as DC charging units, since they are expected to be used in residences or the parking areas of workplaces and due to low current draw. Since DC charging units are used for commercial purposes and draw high currents in a short time, they cause serious effects on the electricity grid.

The electricity grid is adversely affected as DC charging units are fed with alternating current from the grid and transfer this alternating current to EVs via AC/DC converters.

Due to the uncertainties in the demand forecasts of DC charging units, which we define as fast charging, the effects of DC charging stations on the electricity grid should be considered by considering controlled and uncontrolled charging situations. The effects of DC charging stations on the electricity distribution network are mainly; voltage instability, increased peak power demand, power quality problems, increased power losses, and transformer overloads.

Voltage Instability

The demand for electrical energy at DC charging stations contains great uncertainty due to the behavior of EV users and uncontrolled charging processes. As a result of these uncertainties, fluctuations in the grid voltage are experienced. Due to the high current draw of the fast-charging stations in a short time, the demand load in the electricity distribution network will increase and instantaneous decreases will be recorded in the grid voltage due to the constant electricity generation. Kelly et al. in [25] examined the estimated voltage drop caused by uncontrolled charging in three types of distribution networks (urban, suburban and rural). To bring the voltage to the nominal value, after the voltage step adjustment in the distribution transformers or an increase in electrical energy production, the network voltage will increase as a result of the decrease in the load with the decrease in the demand at the DC charging station. This situation will be repeated according to the DC charging station usage behavior of EV users at different times during the day. For this reason, voltage instability will be experienced in the electricity distribution network and grid operators will have great difficulty in grid operation.

Increasing Peak Power Demand

The hours with the highest power demand in electricity distribution networks are noon and evening hours. Considering the behavior of EV users, it is known that the highest energy demands of DC charging stations are in these hours [26]. When the current grid power demand and the demand of DC charging stations are combined, the power demand during the day will increase and the difference between the lowest power demand and the highest power demand during the day will increase significantly. According to a study by Qian et al. in the UK [27], a 10% market penetration of EVs will result in 17.9% of peak daily load demand and a 35.8% increase in daily peak demand with 20% market entry.

Power Quality Issues

Fast charging of EVs is via DC charging units. DC charging units cause power quality problems in the electrical network because they contain AC/DC converters and many powers electronic devices.

Ppower quality refers to a system operation that does not distort the sinusoidal waveform and does not exceed the harmonic values determined by the standards. With the integration of the EV into the grid, harmonics occur in the grid voltage. According to IEEE standard 519, if the total harmonic distortion (THD) value exceeds 5% at a mains voltage of up to 69 kV, it is defined as a deterioration in power quality. According to the study of Karmaker et al.in [28], THD values will be observed in the network by 4.82% by connecting 1 EVCS, by 12.35% by connecting 3 EVs, and by 16.69% by connecting 5 EVs.

The study by Gomez et al. in [29] showed that the total harmonic distortion of the current (THDc) affects the lifetime of the transformer. This study revealed

that THDc should not exceed 25-30% for the transformer life to be affected at an acceptable level. In the study of Zhou et al. in [30], it was determined that the cables in the electrical network were overloaded due to THDc. Harmonics caused by EVCSs also affect the service life of other devices in the system.

Increased Power Losses

Power losses will occur in cables and transformers at the rate of load that EVCSs will draw from the network. Various studies have been carried out to examine the power losses in the system due to the charging of EVs. In the study of Fernandez et al., the power losses caused by uncontrolled charging on two large-scale distribution systems at three different penetration levels (35%, 51%, and 62%) were examined and it was revealed that uncontrolled charging caused high power losses [31]. Deb et al. [32] investigated the energy losses resulting from the rapid charging of electric vehicles in the IEEE 33 bus distribution system. Accordingly, it has been concluded that establishing fast charging stations far from the transformer will increase power losses in the network.

New investments will be needed in the electricity distribution network due to the unplanned increase in DC charging stations and increased power losses as a result of uncontrolled charging processes. Investments that cannot be made on time will cause interruptions and restrictions in the electricity distribution network.

Transformer Overloads

With the connection of EV fast charging stations to the electricity distribution network when the power losses in the cables and transformers feeding these stations are taken into account in addition to the DC charging station power demands of electric vehicles, a serious load will occur in the existing transformers. In systems where careful planning is not done or the concurrency factors are not calculated correctly, transformer overloads will be inevitable. While determining the transformer capacity, it should be noted that EVCSs will draw more reactive power compared to residential and commercial loads, and this should not be neglected while determining the transformer capacity [33]. In [34], the effects of 50% penetration of EVs on the electricity distribution network in a system containing 25 kVA and 50 kVA distribution transformers are investigated. As a result of the study, it was determined that 50% of 25 kVA transformers and 35% of 50 kVA transformers were overloaded at a 50% penetration level.

INTEGRATION OF PV SYSTEMS AND ESSS FOR EV FAST CHARGING STATIONS

To reduce the negative effects of EV fast charging stations on the electricity distribution network, many methods have been developed, such as optimizing charging stations by taking into account the network structure, developing various control methods at charging stations, and integrating PV+ ESSs into charging

stations. Among these methods, one of the methods that offer a comprehensive solution to the effects of charging stations on the electricity distribution network is to integrate a renewable power source, especially a PV+ ESSs, into fast charging stations as can be seen in fig.2. In this section, firstly, some information about the application of this method will be given, and then the extent to which fast charging stations can reduce the negative effects on the network will be mentioned by showing references from the literature.

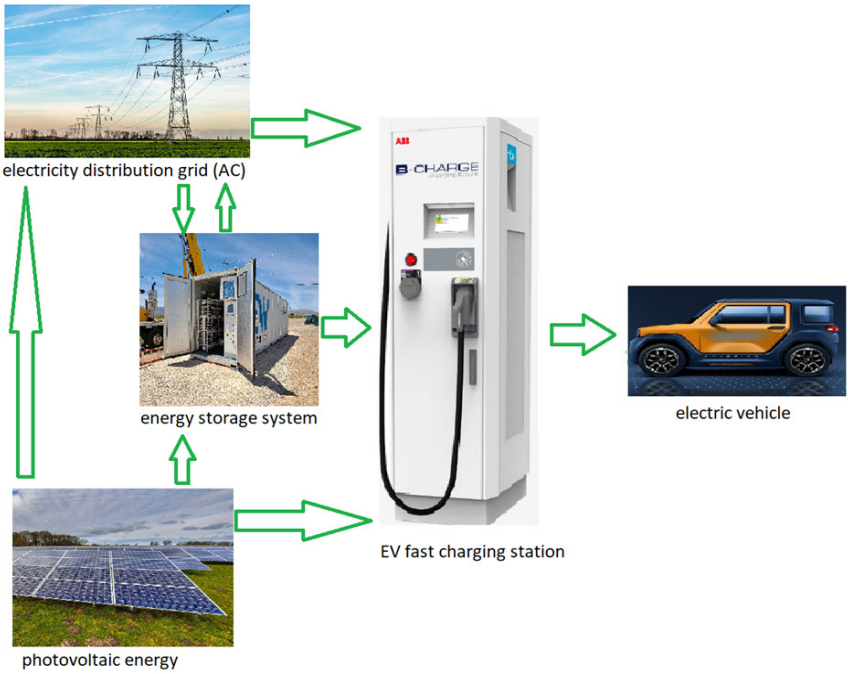

Figure 2. PV+ ESSs integrated EV fast charging station

Since PV systems are systems that obtain electrical energy from solar energy, they can produce electrical energy during daylight hours. However, it cannot produce energy at full capacity on cloudy days or during cloud transitions during the day. Because of this uncertainty, PV systems alone are not sufficient to support fast charging stations. Considering this situation, it is predicted that the use of ESSs will support fast charging stations in many ways.

According to the results of the case study conducted at a charging station supported by PV+ ESSs in Beijing, China, uncertainty occurs in the PV system according to certain months of the year and weather conditions during the day. In terms of the operator, it is seen that it facilitates system management by eliminating uncertainties in the system [35].

To prevent damage to the PV+ ESSs that meet the energy demanded by the charging units at the charging stations, some restrictions should be made. As an

example system, a microgrid design application connected to the PV-based electricity grid of the University of Trieste (ITALY) can be given. Sonnen hybrid single-phase inverter with 9.5/10, 3.3 kW maximum power converts DC power from a 3.9 kWp PV array and 10 kWh lithium iron phosphate battery into AC power. In the application of the charging station indicated in the figure, it has a maximum power of 22 kW per EVC and 400 W for electric bicycles per socket [36]. A PV+ ESSs, which will be optimized considering the constraints on the transformer capacities to which some charging stations will be connected, will reduce the power loss in the system. This issue should also be considered in the design of PV+ ESSs-supported charging stations [37].

Different control methods applied in the integration of PV+ ESSs to fast charging stations have led to different results on power outages, voltage instability, harmonic pollution, and voltage fluctuations. In this type of hybrid system, control methods are also important in terms of reducing the effects on the electricity distribution network [38]. The types of batteries used in ESSs reduce the power demand of charging stations at different levels. In a case study by Calise et al. in [39] at a taxi rank in Italy, it is presented how lead-acid and lithium-ion batteries used in ESSs can reduce the energy drawn from the grid. Accordingly, it has been revealed that the total energy demand drawn by the taxi rank from the grid is reduced by 12% when lead-acid batteries are used and 19% when lithium-ion batteries are used. As a result of reducing the high-power demand of the charging station by using the ESS, transformer overload was prevented and power losses were also reduced.

In the study by Recife et al. [40], a proposed PV+ESSs design for EVCSs in Campinas, Brazil was formulated and optimized using HOMER grid software. According to the results obtained, while the demand load of EVCSs is met with the energy supplied from the PV system during the day, ESS is activated at night or when the amount of radiation obtained from the sun cannot meet the entire demand of the charging stations, reducing the increase in energy demand. In the study of Yan et al. [41], it has been demonstrated by simulating experimental methods that PV systems designed using game theory support the charging station, but because it is not a stable power source, ESS will make positive contributions to the electricity distribution network at the point of the problems to be experienced in the grid voltage and the increase in the demand power.

In the study of Grande et al. [42]; Considering the amount of sunshine in Madrid, Spain, it has been observed that PV systems designed with HOMER grid software reduce the increased load demand due to charging stations when used with ESSs at EVCSs. In the study of Cahndrakar et al. [42], [43], simulation results in the modeling of a PV+ ESSs integrated EVCS using a solar tracking system showed that high-demand power was reduced and voltage stability was ensured, especially during peak hours of use of the charging stations. In the study of Jain and Singh [44],

the experimental results of the EVCS with integrated PV+ ESSs in the laboratory environment showed that; The photovoltaic and EVCSs integrated into the charging stations have reduced the negative effects such as voltage instability and current harmonics caused by the charging stations in the grid. In the study of Singh and Sharma [45], an EVCS is modeled, for which demand load from the grid is estimated using Monte Carlo simulation. Renewable energy sources and ESSs are integrated to reduce the demand load of the EVCS. This integrated hybrid system not only reduced the demand peak load but also reduced the daily energy loss by 30.085 percent and minimized the voltage deviation by 1.165 percent. The study by Kasturi and Nayak [46] has shown that a PV+ ESSs integrated charging station, which is optimized using the whale optimization algorithm, reduces the power losses in the electricity distribution network. In the study by Nguyen and Byrne [47], in a case study for the city of Los Angeles, it is revealed that the peak power demand of fast charging stations is reduced from 79.7 kW to 33.21 kW, supported by the PV system and ESS. With the decrease in peak power demand, transformer overload is prevented and power losses are reduced. In the study by Salama and Vokony [48], simulation results have shown that the power quality problems (power losses, voltage fluctuation) to be created by the charging station on the grid can be reduced and reactive power support can be provided by using a whole coordinated system based on fuzzy logic control PV+ ESSs. In the study of Tayyab et al., it was observed that PV+ ESSs minimized voltage deviation in a fast-charging station modeled using Monte Carlo simulation considering the model of travel and charging behavior in real traffic [49]. In the study of Liu et al. [50], simulation results in a fast-charging station with integrated PV+ ESSs designed using the Non-determined Sorting Genetic Algorithm-II algorithm showed that the load fluctuation could be reduced by more than 21%. The large-size ESSs integrated into the fast-charging stations reduce the sudden loads demanded from the network, prevent the transformer from being overloaded, and prolong its life. In the study of Datta et al. [51], it has been shown that it is possible to reduce transformer overloads by up to 138%, according to simulation results in fast charge modeling with integrated PV+ ESSs.

Affonso and Kezunovic's study, in a case study they conducted by considering Texas weather conditions, as a result of uncontrolled charging processes in fast charging stations, overloading in the transformer in the distribution network fed by the charging station reduces the life of the transformer, but by integrating PV+ ESSs into the fast-charging station, the overload in the transformer is reduced. The results showed that transformer life is extended [52].

CONCLUSION

With the increase in the number of EVs, the widespread use of EVCSs has brought along many problems. Fast charging stations have many negative effects on the electricity distribution network such as voltage instability, increased peak power

demand, power quality problems, power losses, and transformer overloads. In the global world, where energy crises have begun to emerge, it is of great importance to use electrical energy with less loss and without compromising power quality. In this direction, many methods have been developed to reduce the mentioned negative effects. Among these methods, the PV+ESSs integration model to charging stations offer a solution to the majority of the negative effects of charging stations on the grid.

Within the scope of this chapter, many studies in the literature about the effects of fast charging stations on the electricity grid and the role of PV+ESS integration in reducing the negative effects of charging stations on the grid were examined. As can be seen in Table 2, 14 studies showing the effects of fast charging stations on the electricity grid and 16 studies showing that PV+ESSs have a mitigating role in these effects were examined.

Table 2. Literature review summary table on the effects of charging stations on the grid and PV+ESS integration

Effects of Fast EV Charging Stations	**Studies Involving the Identification of Problems**	**Studies Proposing Solutions**
Voltage Instability	[11],[24],[25]	[38],[43],[44],[45][49]
Increased Peak Power Demand	[11],[14],[21],[26],[2]	[13],[39],[40],[41],[42] [43],[45],[47]
Power Quality Issues	[28],[29],[30]	[38],[41],[44],[48]
Increased Power Losses	[11],[31],[32]	[37],[45],[46]
Transformer Overloads	[11],[33],[34]	[51],[52]

Fast charging stations have negative effects on the electricity distribution network such as voltage instability, increased peak power demand, power quality problems, power losses, and transformer overloads. Many methods have been developed to eliminate these negative effects. Among these methods, the PV+ESSs integration model for charging stations offer a solution to most of the negative effects of charging stations on the grid. In the related studies examined, it has been seen that PV+ESSs, which are integrated into fast charging stations, play a role as two new power sources in the system, apart from the mains. In this way, it was emphasized that the increasing peak power demand of charging stations could be reduced. In a study examined, in parallel with the decrease in the amount of load demanded from the network, power losses were reduced by about 31%. Thus, transformer overloads will be prevented and the service life of the transformer will be extended. In another study examined, this situation was calculated and it was seen that it was possible to reduce transformer overloads by up to 138%. In addition, in these studies, it has been shown that the voltage instability and power quality problems in the electricity

grid, which are caused by the uncertainties of the charging demand at fast charging stations and the production profile of PV systems, can be significantly reduced with the introduction of ESSs.

It is planned that future work on this subject will be the positioning and sizing of the charging stations. Because in every country, it is necessary to position and size the charging stations by making realistic plans on the scale of cities, and the use of PV+ESSs should not be avoided due to commercial concerns while making these plans. The positioning and sizing of fast charging stations, especially in public areas, have gained great importance in terms of the electricity distribution network. The fact that zoning plans have not been prepared considering the charging stations in many cities of the world and that the electricity distribution network infrastructures are not at a level to meet the load demands of the fast charging station facilities will be among the biggest problems of local and central governments in the near future. Therefore, local and central governments are required to enact and implement laws that will require the use of the PV+ESSs integration model in public and commercial EVCSs, but which will support the investor who will establish a charging station facility economically.

REFERENCES

[1] G. Fontaras, N. G. Zacharof, and B. Ciuffo, "Fuel consumption and CO2 emissions from passenger cars in Europe – Laboratory versus real-world emissions," *Progress in Energy and Combustion Science*, vol. 60. Elsevier Ltd, pp. 97–131, 2017. DOI: 10.1016/j.pecs.2016.12.004.

[2] H. Hao, Z. Liu, F. Zhao, W. Li, and W. Hang, "Scenario analysis of energy consumption and greenhouse gas emissions from China's passenger vehicles," *Energy*, vol. 91, pp. 151–159, Nov. 2015, DOI: 10.1016/j.energy.2015.08.054.

[3] L. Yuan, H. Zhao, H. Chen, and B. Ren, "Nonlinear MPC-based slip control for electric vehicles with vehicle safety constraints," *Mechatronics*, vol. 38, pp. 1–15, Sep. 2016, DOI: 10.1016/j.mechatronics.2016.05.006.

[4] D. Meyer and J. Wang, "Integrating ultra-fast charging stations within the power grids of smart cities: A review," *IET Smart Grid*, vol. 1, no. 1. Institution of Engineering and Technology, pp. 3–10, 2018. doi: 10.1049/iet-stg.2018.0006.

[5] F. Li *et al.*, "Regional comparison of electric vehicle adoption and emission reduction effects in China," *Resour Conserv Recycl*, vol. 149, pp. 714–726, Oct. 2019, DOI: 10.1016/j.resconrec.2019.01.038.

[6] E. E. Michaelides, "Thermodynamics and energy usage of electric vehicles," *Energy Convers Manag*, vol. 203, Jan. 2020, DOI: 10.1016/j.enconman.2019.112246.

[7] C. King and B. Datta, "EV charging tariffs that work for EV owners, utilities and society," *Electricity Journal*, vol. 31, no. 9, pp. 24–27, Nov. 2018, DOI: 10.1016/j.tej.2018.10.010.

[8] B. Csonka and C. Csiszár, "Determination of charging infrastructure location for electric vehicles," in *Transportation Research Procedia*, 2017, vol. 27, pp. 768–775. DOI: 10.1016/j.trpro.2017.12.115.

[9] S. Zu and L. Sun, "Research on location planning of urban charging stations and battery-swapping stations for electric vehicles," *Energy Reports*, vol. 8, pp. 508–522, Jul. 2022, DOI: 10.1016/j.egyr.2022.01.206.

[10] O. Sadeghian, A. Oshnoei, B. Mohammadi-ivatloo, V. Vahidinasab, and A. Anvari-Moghaddam, "A comprehensive review on electric vehicles smart charging: Solutions, strategies, technologies, and challenges," *Journal of Energy Storage*, vol. 54. Elsevier Ltd, Oct. 01, 2022. doi: 10.1016/j.est.2022.105241.

[11] H. Shareef, M. M. Islam, and A. Mohamed, "A review of the stage-of-the-art charging technologies, placement methodologies, and impacts of electric vehicles," *Renewable and Sustainable Energy Reviews*, vol. 64. Elsevier Ltd, pp. 403–420, Oct. 01, 2016. doi: 10.1016/j.rser.2016.06.033.

[12] A. Ajanovic, "Promoting environmentally benign electric vehicles," in *Energy Procedia*, 2014, vol. 57, pp. 807–816. DOI: 10.1016/j.egypro.2014.10.289.

[13] W. Khan, F. Ahmad, and M. S. Alam, "Fast EV charging station integration with grid ensuring optimal and quality power exchange," *Engineering Science and Technology, an International Journal*, vol. 22, no. 1, pp. 143–152, Feb. 2019, DOI: 10.1016/j.jestch.2018.08.005.

[14] A. M. Mowry and D. S. Mallapragada, "Grid impacts of highway electric vehicle charging and role for mitigation via energy storage," *Energy Policy*, vol. 157, Oct. 2021, DOI: 10.1016/j.enpol.2021.112508.

[15] X. Han, Y. Liang, Y. Ai, and J. Li, "Economic evaluation of a PV combined energy storage charging station based on cost estimation of second-use batteries," *Energy*, vol. 165, pp. 326–339, Dec. 2018, DOI: 10.1016/j.energy.2018.09.022.

[16] E. Martinez-Laserna *et al.*, "Battery second life: Hype, hope or reality? A critical review of the state of the art," *Renewable and Sustainable Energy Reviews*, vol. 93. Elsevier Ltd, pp. 701–718, Oct. 01, 2018. doi: 10.1016/j.rser.2018.04.035.

[17] J. Geng, S. Gao, X. Sun, Z. Liu, F. Zhao, and H. Hao, "Potential of electric vehicle batteries second use in energy storage systems: The case of China," *Energy*, vol. 253, Aug. 2022, DOI: 10.1016/j.energy.2022.124159.

[18] P. Sadeghi-Barzani, A. Rajabi-Ghahnavieh, and H. Kazemi-Karegar, "Optimal fast charging station placing and sizing," *Appl Energy*, vol. 125, pp. 289–299, Jul. 2014, DOI: 10.1016/j.apenergy.2014.03.077.

[19] M. Nurmuhammed and T. Karadağ, "Elektrikli Araç Şarj İstasyonlarının Konumlandırılması ve Enerji Şebekesi Üzerine Etkisi Konulu Derleme Çalışması A Review on Locating the Electric

Vehicle Charging Stations and Their Effect on the Energy Network." [Online]. Available: http://dergipark.gov.tr/gujsa

[20] T. G. San Román, I. Momber, M. R. Abbad, and Á. Sánchez Miralles, "Regulatory framework and business models for charging plug-in electric vehicles: Infrastructure, agents, and commercial relationships," *Energy Policy*, vol. 39, no. 10, pp. 6360–6375, Oct. 2011, doi: 10.1016/j.enpol.2011.07.037.

[21] K. L. Lim, S. Speidel, and T. Bräunl, "A comparative study of AC and DC public electric vehicle charging station usage in Western Australia," *Renewable and Sustainable Energy Transition*, vol. 2, p. 100021, Aug. 2022, DOI: 10.1016/j.rset.2022.100021.

[22] R. Zhou, Z. Ping, G. Wang, L. Li, G. Li, and B. Zhang, "A Study of Charging Demand Estimation Model of Electric Passenger Vehicles in Beijing," in *Chinese Control Conference, CCC*, Jul. 2021, vol. 2021-July, pp. 5847–5852. DOI: 10.23919/CCC52363.2021.9550695.

[23] J. A. Domínguez-Navarro, R. Dufo-López, J. M. Yusta-Loyo, J. S. Artal-Sevil, and J. L. Bernal-Agustín, "Design of an electric vehicle fast-charging station with the integration of renewable energy and storage systems," *International Journal of Electrical Power and Energy Systems*, vol. 105, pp. 46–58, Feb. 2019, DOI: 10.1016/j.ijepes.2018.08.001.

[24] M. R. Mozafar, M. H. Moradi, and M. H. Amini, "A simultaneous approach for optimal allocation of renewable energy sources and electric vehicle charging stations in smart grids based on improved GA-PSO algorithm," *Sustain Cities Soc*, vol. 32, pp. 627–637, Jul. 2017, DOI: 10.1016/j.scs.2017.05.007.

[25] L. Kelly, A. Rowe, and P. Wild, "Analyzing the impacts of plug-in electric vehicles on distribution networks in British Columbia," in *2009 IEEE Electrical Power and Energy Conference, EPEC 2009*, 2009. DOI: 10.1109/EPEC.2009.5420904.

[26] Z. Yi, X. C. Liu, and R. Wei, "Electric vehicle demand estimation and charging station allocation using urban informatics," *Transp Res D Transp Environ*, vol. 106, p. 103264, May 2022, DOI: 10.1016/j.trd.2022.103264.

[27] K. Qian, C. Zhou, M. Allan, and Y. Yuan, "Modeling of load demand due to EV battery charging in distribution systems," *IEEE Transactions on Power Systems*, vol. 26, no. 2, pp. 802–810, May 2011, DOI: 10.1109/TPWRS.2010.2057456.

[28] A. K. Karmaker, S. Roy, and Md. R. Ahmed, "Analysis of the Impact of Electric Vehicle Charging Station on Power Quality Issues," in *2019 International Conference on Electrical, Computer and Communication Engineering (ECCE)*, Feb. 2019, pp. 1–6. doi: 10.1109/ECACE.2019.8679164.

[29] J. C. Gómez and M. M. Morcos, "Impact of EV battery chargers on the power quality of distribution systems," *IEEE Transactions on Power Delivery*, vol. 18, no. 3, pp. 975–981, Jul. 2003, DOI: 10.1109/TPWRD.2003.813873.

[30] C. Zhou, H. Wang, W. Zhou, K. Qian, and S. Meng, "Determination of maximum level of EV penetration with consideration of EV charging load and harmonic currents," in *IOP Conference Series: Earth and Environmental Science*, Oct. 2019, vol. 342, no. 1. doi: 10.1088/1755-1315/342/1/012010.

[31] L. Pieltain Fernández, T. Gómez San Román, R. Cossent, C. Mateo Domingo, and P. Frías, "Assessment of the impact of plug-in electric vehicles on distribution networks," *IEEE Transactions on Power Systems*, vol. 26, no. 1, pp. 206–213, Feb. 2011, DOI: 10.1109/TPWRS.2010.2049133.

[32] S. Deb, K. Tammi, K. Kalita, and P. Mahanta, "Impact of Electric Vehicle Charging Station Load on Distribution Network," *Energies (Basel)*, vol. 11, no. 1, p. 178, Jan. 2018, DOI: 10.3390/en11010178.

[33] M. A. Sayed, R. Atallah, C. Assi, and M. Debbabi, "Electric vehicle attack impact on power grid operation," *International Journal of Electrical Power & Energy Systems*, vol. 137, p. 107784, May 2022, DOI: 10.1016/j.ijepes.2021.107784.

[34] M. K. Gray and W. G. Morsi, "Power Quality Assessment in Distribution Systems Embedded With Plug-In Hybrid and Battery Electric Vehicles," *IEEE Transactions on Power Systems*, vol. 30, no. 2, pp. 663–671, Mar. 2015, DOI: 10.1109/TPWRS.2014.2332058.

[35] M. Yang, L. Zhang, Z. Zhao, and L. Wang, "Comprehensive benefits analysis of electric vehicle charging station integrated photovoltaic and energy storage," *J Clean Prod*, vol. 302, Jun. 2021, DOI: 10.1016/j.jclepro.2021.126967.

[36] A. Cabrera-Tobar, A. M. Pavan, N. Blasuttigh, G. Petrone, and G. Spagnuolo, "Real time Energy Management System of a photovoltaic based e-vehicle charging station using Explicit Model Predictive Control accounting for uncertainties," *Sustainable Energy, Grids and Networks*, vol. 31, Sep. 2022, DOI: 10.1016/j.segan.2022.100769.

[37] M. S. Islam, N. Mithulananthan, K. Bhumkittipich, and A. Sode-Yome, "EV charging station design with PV and energy storage using energy balance analysis," in *Proceedings of the 2015 IEEE Innovative Smart Grid Technologies - Asia, ISGT ASIA 2015*, Jan. 2016. DOI: 10.1109/ISGT-Asia.2015.7386999.

[38] P. García-Triviño, J. P. Torreglosa, L. M. Fernández-Ramírez, and F. Jurado, "Control and operation of power sources in a medium-voltage direct-current microgrid for an electric vehicle fast charging station with a photovoltaic and a battery energy storage system," *Energy*, vol. 115, pp. 38–48, Nov. 2016, DOI: 10.1016/j.energy.2016.08.099.

[39] F. Calise, F. L. Cappiello, A. Cartenì, M. Dentice d'Accadia, and M. Vicidomini, "A novel paradigm for a sustainable mobility based on electric vehicles, photovoltaic panels, and electric energy storage systems: Case studies for Naples and Salerno (Italy)," *Renewable and Sustainable Energy Reviews*, vol. 111, pp. 97–114, Sep. 2019, DOI: 10.1016/j.rser.2019.05.022.

[40] A. VPG Araújo, D. N. Araujo, A. S. Vasconcelos, W. A. de Silva Júnior, and P. A. Rosas, "A Proposal for Technical and Economic Sizing of Energy Storage System and PV for EV Charger Stations with Reduced Impacts on the Distribution Network," 2021.

[41] D. Yan, H. Yin, T. Li, and C. Ma, "A Two-Stage Scheme for Both Power Allocation and EV Charging Coordination in a Grid-Tied PV-Battery Charging Station," *IEEE Trans Industr Inform*, vol. 17, no. 10, pp. 6994–7003, Oct. 2021, doi: 10.1109/TII.2021.3054417.

[42] L. S. A. Grande, I. Yahyaoui, and S. A. Gómez, "Energetic, economic and environmental viability of off-grid PV-BESS for charging electric vehicles: A case study of Spain," *Sustain Cities Soc*, vol. 37, pp. 519–529, Feb. 2018, DOI: 10.1016/j.scs.2017.12.009.

[43] M. Chandrakar, H. B, R. M J, A. H A, S. T S, and P. Malipatil, "Modeling and Simulation of EV charging station during Peak Load condition using PV and BES," in *2021 4th International Conference on Recent Developments in Control, Automation & Power Engineering (RD CAPE)*, Oct. 2021, pp. 450–453. DOI: 10.1109/RDCAPE52977.2021.9633533.

[44] V. Jain, Seema, and B. Singh, "A Three Phase Grid Connected EV Charging Station with PV Generation and Battery Energy Storage with Improved Power Quality," in *Conference Record - IAS Annual Meeting (IEEE Industry Applications Society)*, 2021, vol. 2021-October. doi: 10.1109/IAS48185.2021.9677311.

[45] B. Singh and A. K. Sharma, "Benefit maximization and optimal scheduling of renewable energy sources integrated system considering the impact of energy storage device and Plug-in Electric vehicle load demand," *J Energy Storage*, vol. 54, Oct. 2022, DOI: 10.1016/j.est.2022.105245.

[46] K. Kasturi and M. Ranjan Nayak, "Optimal Planning of Charging Station for EVs with PV-BES Unit in Distribution System Using WOA."

[47] R. D. Trevisan, T. A. Nguyen, and R. H. Byrne, "Sizing Behind-the-Meter Energy Storage and Solar for Electric Vehicle Fast-Charging Stations; Sizing Behind-the-Meter Energy Storage and Solar for Electric Vehicle Fast-Charging Stations," 2020.

[48] H. S. Salama and I. Vokony, "Comparison of different electric vehicle integration approaches in presence of photovoltaic and superconducting magnetic energy storage systems," *J Clean Prod*, vol. 260, Jul. 2020, DOI: 10.1016/j.jclepro.2020.121099.

[49] E. Verband der Elektrotechnik, *NEIS 2021; Conference on Sustainable Energy Supply and Energy Storage Systems : 13-14 Sept. 2021*.

[50] J. Liu, C. Gao, and Y. Cao, "Multi-Objective Optimized Configuration of Electric Vehicle Fast Charging Station Combined with PV Generation and Energy Storage," in *2020 IEEE 3rd International Conference on Electronics Technology (ICET)*, May 2020, pp. 467–473. doi: 10.1109/ICET49382.2020.9119613.

[51] U. Datta, A. Kalam, and J. Shi, "Smart control of BESS in PV integrated EV charging station for reducing transformer overloading and providing battery-to-grid service," *J Energy Storage*, vol. 28, Apr. 2020, DOI: 10.1016/j.est.2020.101224.

[52] C. D. M. Affonso and M. Kezunovic, "Technical and economic impact of PV-bess charging station on transformer life: A case study," *IEEE Trans Smart Grid*, vol. 10, no. 4, pp. 4683–4692, Jul. 2019, DOI: 10.1109/TSG.2018.2866938.

Chapter 7

DESIGN OF SMART VERTICAL HYDROPONIC SYSTEM

Islem Ben HASSINE[1], Dhafer MEZGHANNI[1], Anouar BELKADI[1], Nizar SGHAEIR[2], Abdelkader MAMI[1]

1 University of Tunis El Manar, Faculty of sciences of Tunis, Department of Physics, UR-LAPER, 2092, Tunisia
2 University of Tunis El Manar, Faculty of sciences of Tunis, Department of Physics, Laboratory of Research on Microwave Electronics, 2092, Tunisia

INRODUCTION

This study intends to improve the farmer's quality of life by resolving the aforementioned issues with a vertical Internet of Things-based device. In order to provide farmers with better access to and a more beneficial use of abundant products while they are not on the ground, vertical hydroponic horticulture keeps track of trends, regeneration history, and pertinent information about the farmers [2]. Farmers in small fields should benefit from the water growing structure's ability to increase production yields.

A good technique that uses less dirt [3]. In this new environment, hydroponics concentrated on the horizontal plane because it allowed for more room and had the potential to govern an entire structure in the future [4]. Figure 1 below depicts a modern hydroponics model.

Envisaged design of the system

On the storage device, we have four sensors that are specifically designed to monitor this system in real time: a pH sensor, a temperature sensor, an electrical peculiarity indicator for the EC, and a water flow detector. Additionally, the pH sensor measures the water's pH. The pH of the water is typically seven, but if there are additives, it can drop to five or six. Only a small amount of water, which we typically utilize as manure and monitor via loop valves, is required by plants. The ultrasonic sensor efficiently monitors the plants by measuring the degree. Small plants require a certain water temperature, so we frequently use a sensor to set the temperature. Stacks of water that can be reused later are kept in the water combination pond supply. To avoid any delays, the water reuse unit gathers any extra or discarded water from the entire structure and uses it for the supporting framework. The basin's sustenance levels are stabilized by the system's general water flow, which is accessible in the pipes. In figure 2 below, our system has been schematized.

Design and operating structure

Figure 1 below depicts the hydroponic vertical growing system model and the unit of the development area.

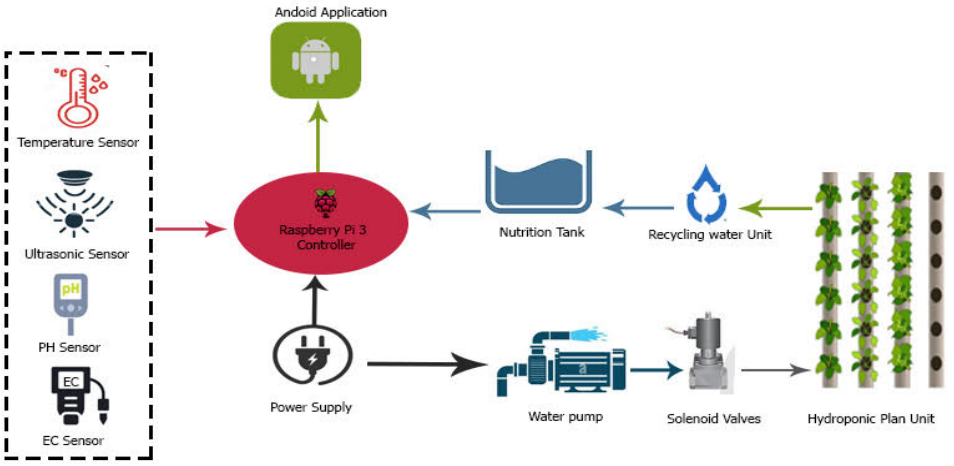

Figure 1. The model envisaged for the vertical structure of hydroponic production

Re-use the water

Pipelines are cut in accordance with the subtleties of the farmers. On this inclined system, the Rockwool has been positioned at a specified level and is ready for production. Due to the system's vertical design, the rock wool likely only saw a small portion of the water after it entered, with the remaining water being absorbed by the nearby structure.

Figure 2. System overview

The most crucial thing is to use the higher level (UL) and lower level (LL) classes to get a general idea of the level of the pond and the rainwater storage tank. An electronic valve should be coordinated with the RPI 3 microprocessor and the motor in order to siphon the water into the plants through the lines. All sensors, including those for humidity, pH, electrical conductivity (EC), and ultrasound, must adhere to strict restrictions. Additionally, each sensor needs to be linked and ready

for installation. The microcontroller gets the information from the device and makes a decision based on the state of the agricultural industry. If there is enough water, it can flow to the plants for a certain amount of time before the engine shuts down on its own. The corresponding tank provides the food. Finally, all the values are delivered to a flexible application and server for the reasons that drive further investigation. The illustrative figure presents the operational diagram and the vertical hydroponic structure's many properties (Fig. 1).

The heights of the water flow and its conditions:

1. When LL UL, No Action is revealed

2. After that, solenoid valve opened for a predetermined period of time.

3. If F UL, close the valve.

Where F = Water Flow, LL = Low Level, and UL = High Level. The aforementioned parameters are needed to adequately water the plants in a vertical hydroponic construction.

According to the unit's programming, the microcontroller unit now has the capacity to open the valve and determine how long it will stay open. The valve becomes inactive as soon as one of these three requirements is satisfied; nevertheless, if the water flow is below the low level, the valve opens swiftly for a set period of time. The third scenario is when the water level is greater than planned and the valve can then close.

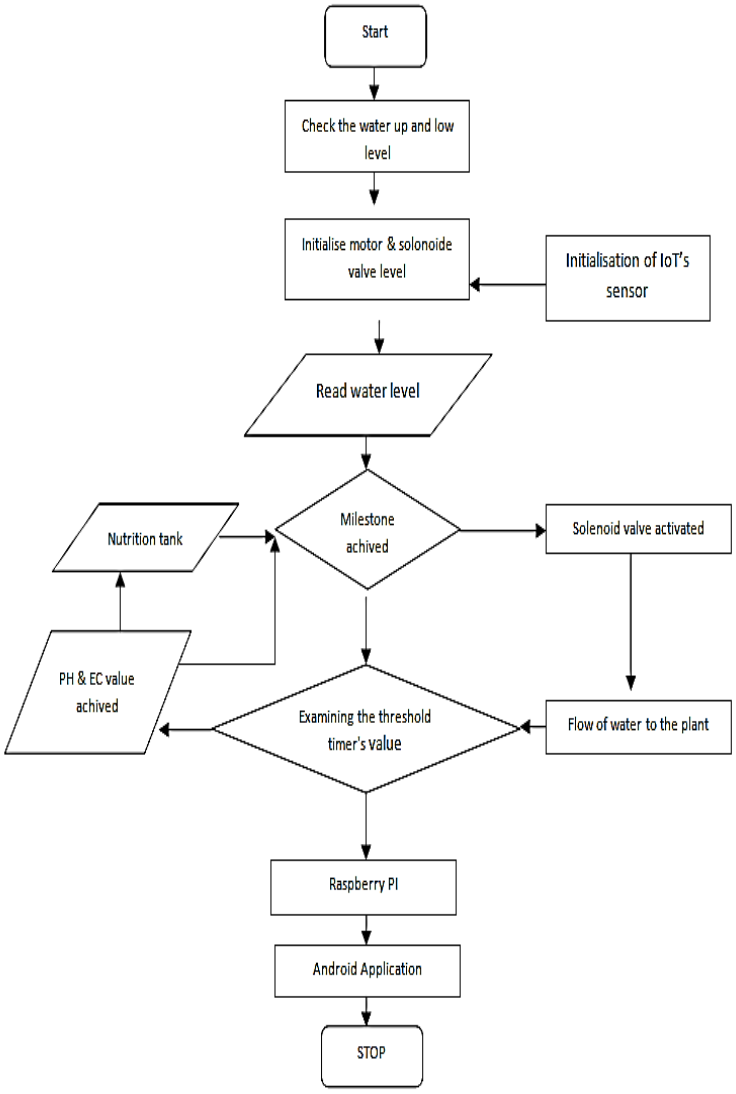

Figure 3. Flow chart of the hydroponic vertical growing system

RESULT AND ANALYSIS

The preliminary strategy for the aforementioned vertical hydroponic system has been put into practice in relatively constrained settings, like the home, and the results have been taken into consideration for further research. Four pipelines in all, a pump in the basin, a food tank, and Rockwool were thought to have been utilized in the process. For thirty days, this course of action was carried out in the regular temperature mode. Following the analysis of all the data, completely distinct findings were made and included to the Android mobile app. All of the station's sensors are wired to a microcontroller unit, which can gauge the equipment's levels while the engine is running. Normal pipe flow is possible while the loop valve is

open. Accurate evaluations are performed At the proper time, the water is removed from the engine so that it can convey the plants before it reaches the pipes. The plants are currently mounted outside and coated in rock wool. The essential water is used by the plants, and the remaining water is given to the matching unit. The leftovers might be delivered to the reservoir or utilised for other purposes. This method enables the maintenance of the consumption of water. Figure 3 shows the water level in the pipes using various different approaches.

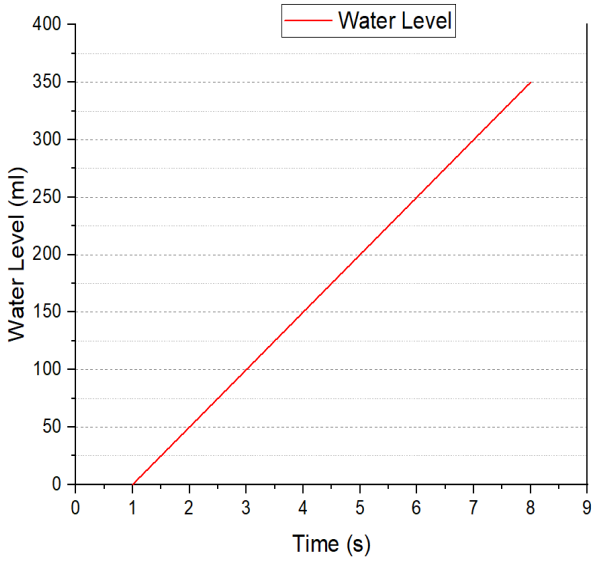

Figure 4. The level of water flowing into the system as a function of time

The output result to the user from the various paths on the tubes is illustrated in the following image in more detail. 5.

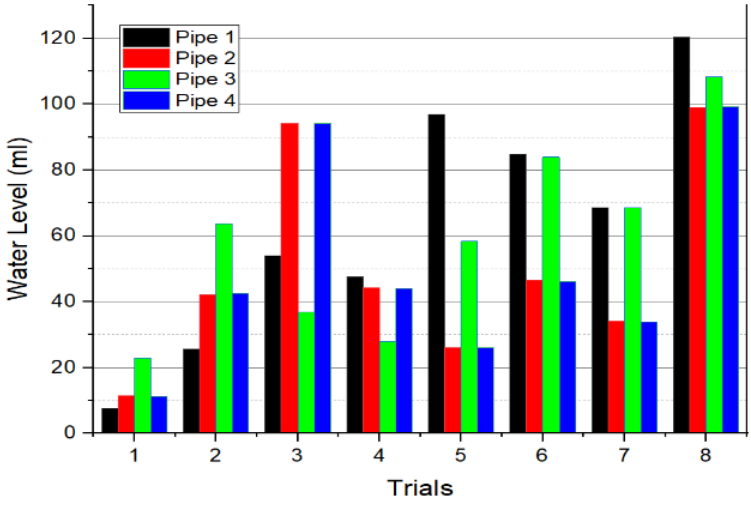

Figure 5. Water levels at various times in various lines.

The water flow on the pipes is completely different because of the installed Rockwool and the size of the maintenance tank. The differences in water flow in the pipes at various beginning units are depicted in Fig. 6.

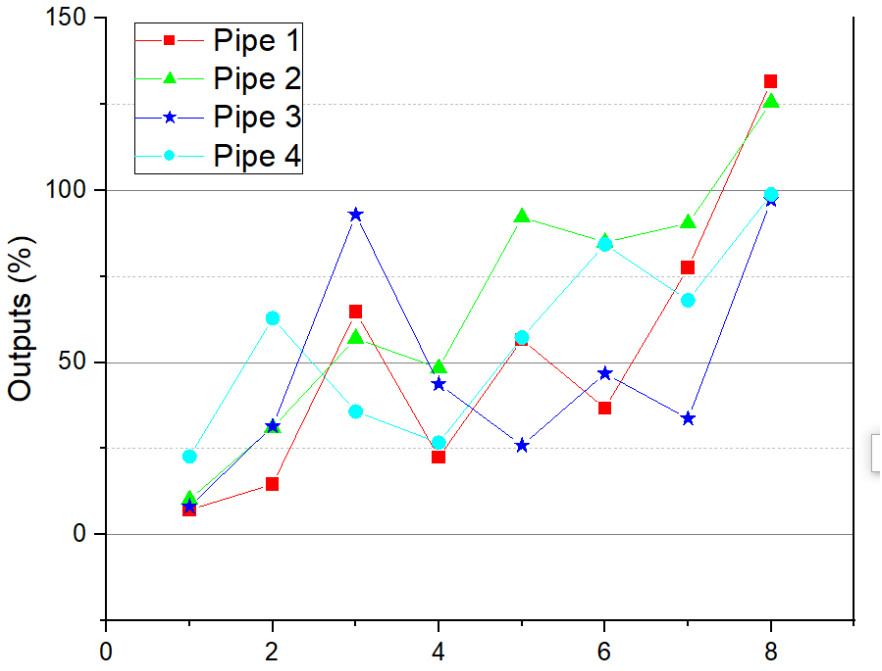

Figure 6. Performance of a vertical hydroponic system.

The amount of time needed for the water to flow differently in a structure with four lines is not constant. This is frequently a result of the plant's growth and its capacity to take in nutrients from the nutrition solution. Each line has fully variable water flow units that can be used in accordance with the requirements of the plants at various times. Because the IoT framework may be used by the ultrasonic sensor component to track the improvement, plant cultivation won't be adversely affected by changes in water levels in the lines. Figure 7 below shows how long it takes to change the water flow in the lines at various distances.

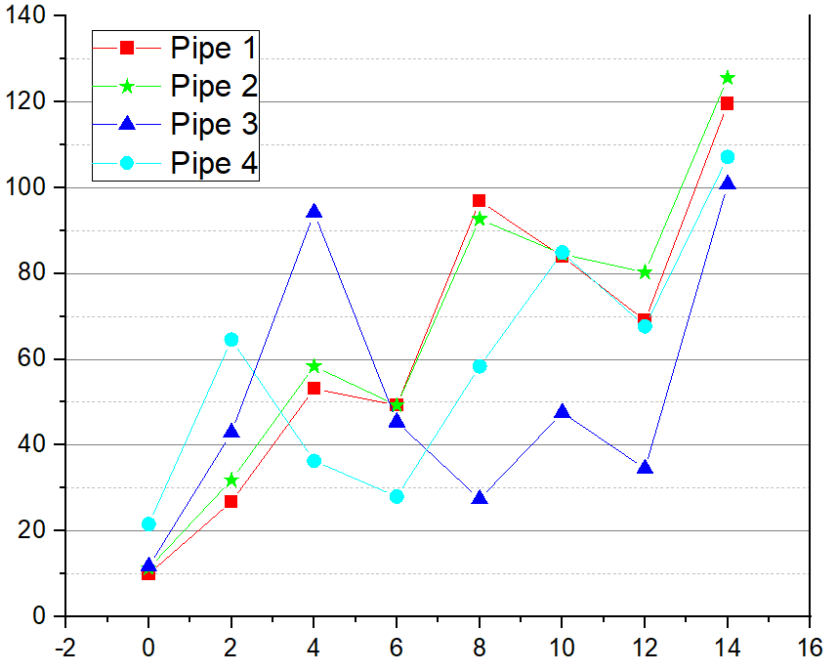

Figure 7. The different water flows in the pipes at different times

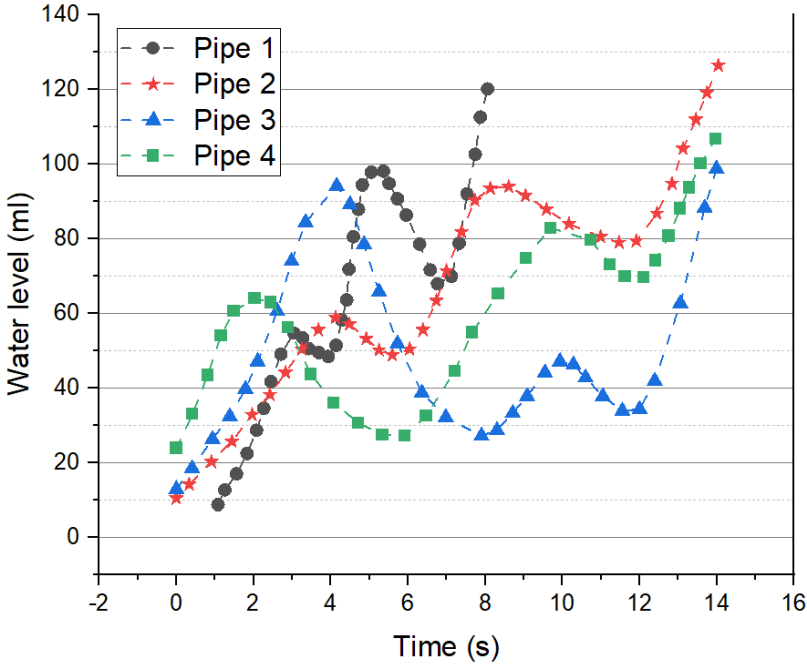

Figure 8. Time required for water flow variations in system conduits

The vertical hydroponic structure is filtered and shown using a robotic mobile android application, and the data is subsequently stored in databases for analysis. Finally, data was gathered from the outcomes and made available to users. This might be incredibly enlightening and simple to use to achieve desired outcomes. The main factors taken into account are plant height, leaf extent, and the number of leaves borne by the structure. A clever hydroponic system outperforms a conventional structure, despite the fact that the outcomes are singular. The quantity, width, and level of the leaves provide a fantastic system. Perception is not carried out in an exceedingly normal structure since the water flow and feed rate are continuously determined. Water is a really reasonable automatic system. Water is likely only provided in a perfectly suitable automated structure when the plant specifically requests it. The device's results over the course of one month in a constrained region are shown in Table I and Table II below.

Table 1. Smart Vertical Hydroponic System

Plant Details	Smart Vertical Hydroponic System			
	1Pipe	2 Pipe	3 Pipe	4 Pipe
H (cm)	10.9	9.8	11.0	10.6
W (cm)	4.7	4.2	3.9	2.8
Leafsproduced	9	9	9	9

Table 2. Normal Vertical Hydroponic System

Plant Details	Normal Vertical Hydroponic System			
	1 Pipe	2 Pipe	3 Pipe	4 Pipe
H (cm)	10.9	9.8	11.0	10.6
W (cm)	4.7	4.2	3.9	2.8
Leafsproduced	9	9	9	9

CONCLUSION

Reusing water is a massive development approach that can be analyzed with enormous amounts of Big Data, which might help lower the cost of development and acreage needed to build a sizable farm.

IoT technologies assist farmers in monitoring water levels and completely unexpected contamination using the flexible Android app. When there are low water levels or evaporation, the farm owner is instantly notified. A number of sensors are employed to assess the water flow and quality in order to benefit the plants. The level of the plants is noted each time they alter, and the findings are shared. Big data analysis is used by farmers to understand how plants, vegetables, and natural fruits are produced in relation to the seasons, such as winter and summer. Small-scale farmers can collect data using this technique since it is both simple and appropriate. This approach assists women in explicitly filling out the technical and financial fields.

REFERENCES

[1] N. Mzid. MThe reform of domestic work in Tunisia, Apr 2022.

[2] Zhengyu Zhu.Fog/edge computing technology and big data system with IoT (School of Information Engineering.PhD)

[3] Faraz Moghimi, Bahram Asiabanpour A Framework for Financial Analysis of the Vertical Farming Systems.

[4] A Raneesha Madushanki , Malka N. Halgamuge, W A H Sarangis Wirasagoda Adoption of the Internet of Things (IoT) in Agriculture and Smart Farming towards Urban Greening: A Review, DOI:10.14569/IJACSA.2019.0100402.

[5] W.Tampakleima Chanu, K.Sarda Devi, K.Chakrapani, B.Wangky, Hydroponics: An Advanced Technique for Vegetable Production (AgriCos e-Newsletter) d.

[6] Anouar Belkadi, Dhafer Mezghanni, and Abdelkader Mami, "IOT AND LIGHTING CONTROL FOR SMART GREENHOUSE", 7ème Conference Internationale des Energies Renouvelables CIER-2019 - Proceedings of Engineering & Technology -PET-, Vol. 59 December 2019.

[7] Ar. Farhat Ali, Futuristic Urbanism - An overview of Vertical farming and urban agriculture for future cities in Tunisia (may 2017).

[8] D.Petrovics, Integrating vertical farming at scale in urban food planning (J.2019).

[9] E. Yolanda Fitria, M.Ary Murti, C.Setianingsih in Jul 2021,Design of Integrated Control System Based On IoT With Context Aware Method In Hydroponic Plants.

[10] Anouar Belkadi, Dhafer Mezghanni, and Abdelkader Mami, (2019) "ENERGY DESIGN AND OPTIMIZATION OF A GREENHOUSE: A HEATING, COOLING AND LIGHTING STUDY", Engineering, Technology & Applied Science Research: 9 pp. 4235-4242 (3).

[11] N. Kumar,G.S. Verma, A.S. Bhoj, R.P. Joshi, T. Pant (Aug 2002),An estimate of yield and nutritive parameters of hybrid tomato (Lycopersicon esculentum) in hydroponics using rain water in Uttaranchal.

[12] Anouar Belkadi, Dhafer Mezghanni, and Abdelkader Mami, (2021) "ENERGY STUDY OF A GREENHOUSE AND OPTIMISATION OF THE CHOICE OF ITS SHAPE AND COVERING MATERIAL: BASED ON AN IMPROVED STATIC MODEL Engenharia Agricola 41 no3 pp. 297-310. Doi: 10.1590/1809-4430-Eng.Agric.v41n3p297-310/2021 .

[13] M. Mishra, S.Saxena, P. Arvind Shirke,plants-11-00579, DOI:10.3390/plants11050579, Feb 2022.

[14] V.Emilia Balas, A. Ella Hassanien, S.Chakrabarti, Lopa Mandal (Jan 2021),Proceedings of International Conference on Computational Intelligence, Data Science and Cloud Computing IEM-ICDC 2020: IEM-ICDC 2020.

[15] A. A. Elngar, A.Pawar, P.Churi ,Data Protection and Privacy in Healthcare: Research and Innovations(jan 2021) DOI: 10.1201/9781003048848.

[16] Randhir Kumar , Rakesh Tripathi, Data Provenance and Access Control Rules for Ownership Transfer Using Blockchain, Apr 2021, DOI: 10.4018/IJISP.2021040105OnDemand.

[17] Anouar Belkadi, Dhafer Mezghanni, and Abdelkader Mami, "ENERGY OPTIMIZATION OF GREENHOUSE", 7ème Conference Internationale sur l'énergie verte et l'ingénierie environnementale (GEEE-2020) - Proceedings of Engineering & Technology -PET-, Vol. 63 pp, 46-56 July 2020.

[18] X.Wu, J.Xu, W. Huang, W.Jian,A new mutual authentication and key agreement protocol in wireless body area network, Nov 2020,DOI: 10.1109/SmartCloud49737.2020.00045.

[19] J. Wang, Y.Luo, Y.Zhao, J. Le, Conference Paper: A Survey on Privacy Preserving Data Mining (Apr 2009).

[20] Mohammed Khan ,An Enhanced, Efficient and Robust Remote User Authentication Method, Dec 2020, DOI: 10.13140/RG.2.2.26935.96169.

[21] S. Q. Sabri , A.M. Ahmad, M.B. Abdulrazaq ,Design and Implementation of Student and Alumni Web Portal.

[22] Anouar Belkadi, Dhafer Mezghanni, and Abdelkader Mami, "ENERGY OPTIMIZATION OF A GREENHOUSE", 7ème Conference Internationale des Energies Renouvelables CIER-2019 - Proceedings of Engineering & Technology -PET-, Vol. 59 December 2019. Poster

[23] K. Rabieh , M. A. Azer,"jan 2011" Combating Sybil Attacks in Vehicular Ad Hoc Networks.

[24] BELKADI, A., MEZGHANI, D. AND MAMI, A. (2019). Energy Design and Optimization of a Greenhouse: A Heating, Cooling and Lighting Study. Engineering, Technology & Applied Science Research, Vol. 9 issue 3, pp. 4235-4242.

[25] Desmond Bala Bisandu ,Lecture notes on Data Engineering and Communication Technologies, "Mar 2019".

[26] D. Honi, IOT Based Automatic Vehicle Accident Detection and Rescue System (Apr 2019).

[27] V.Babenko, Data-Centric Business and Applications. Lecture Notes on Data Engineering and Communications Technologies, "Jul 2020", DOI: 10.1007/978-981-15-4474-3_51.

[28] X.Wang, F. Li, Y. Xie, S.Yang, Y. Wang, Gait and Respiration Based User Identification Using Wi-Fi Signal, DOI: 10.1109/JIOT.2021.3097892, (Jul 2021).

[29] Anouar Belkadi, Dhafer Mezghanni, and Abdelkader Mami, (2020) "DESIGN AND IMPLEMENTATION OF FLC APPLIED TO A SMART GREENHOUSE", Engenharia Agricola 42 no6 pp. 135-142. Doi: 10.1590/1809-4430-Eng.Agric.v40n6p777-790/2020.

Chapter 8

COMPARATIVE STUDY FOR THE SELECTION OF AN EFFECTIVE CONTROLLER FOR THE MANAGEMENT OF SMART GREENHOUSE

Anouar BELKADI[1] , Nizar SGHAIER[2], Islem Ben HASSINE[1], Dhafer MEZGHANNI[1], Abdelkader MAMI[1]

1 University of Tunis El Manar, Faculty of sciences of Tunis, Department of Physics, UR-LAPER, 2092, Tunisia
2 University of Tunis El Manar, Faculty of sciences of Tunis, Department of Physics, Laboratory of Research on Microwave Electronics, 2092, Tunisia

INTRODUCTION

This chapter book is an overview of the simulation used for different control modes applied to the heating and ventilation in order to compare between them and to be able to make the choice of an efficient control mode. The automated control is a technique for continuously regulating the physical quantities of a system such as temperature, humidity in order to impose on it an operating regime according to prescribed targets and levels in a disturbed environment.

Switch on/off control mode

In this section we aim to control the temperature in the greenhouse by applying the ON/OFF control mode. Figure 1 shows the reference trajectory and the evolution of the internal and external temperature. We also see that the internal temperature follows the set point perfectly.

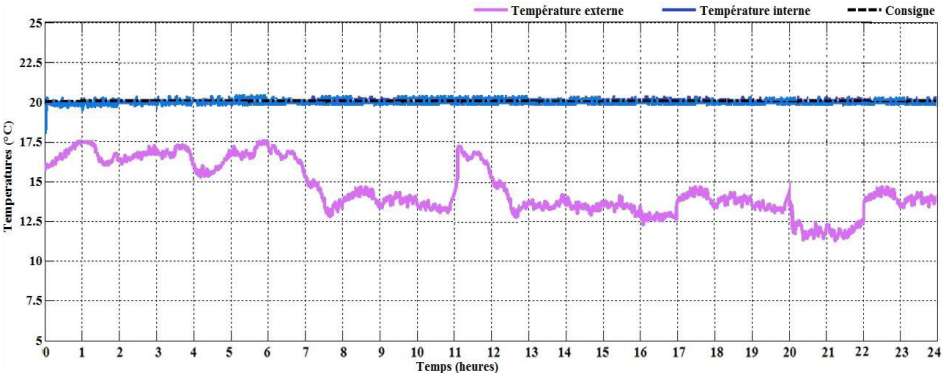

Figure 1. Temperature control in the greenhouse by means of a digital controller

Discrete control is simple in its application as it allows the temperature inside the greenhouse to be regulated despite fluctuations in the outside temperature. However, this method also has some disadvantages, such as the large number of ON/OFF switches.

These fluctuations are unavoidable because it has only two levels, either 0 or 100%, as shown in Figure 2.

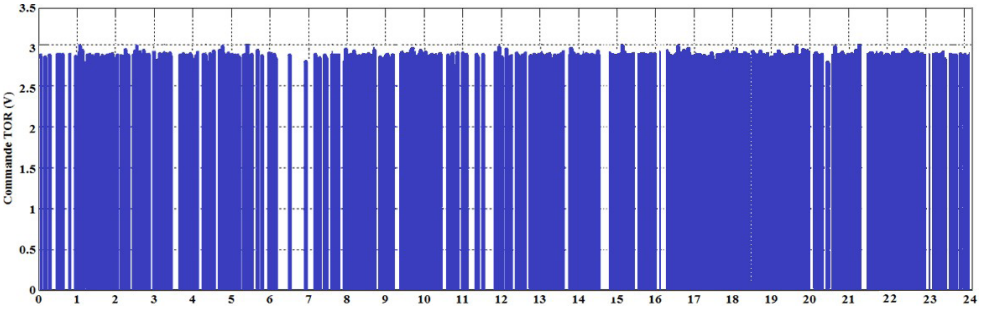

Figure 2. Evolution of the digital control

The evolution of the discrete control, shown in Figure 2, is addressed to the heating or ventilation device, as shown in Figure 3, which clearly shows the evolution of the commands that are sent to these two actuators in order to regulate the temperature inside the greenhouse.

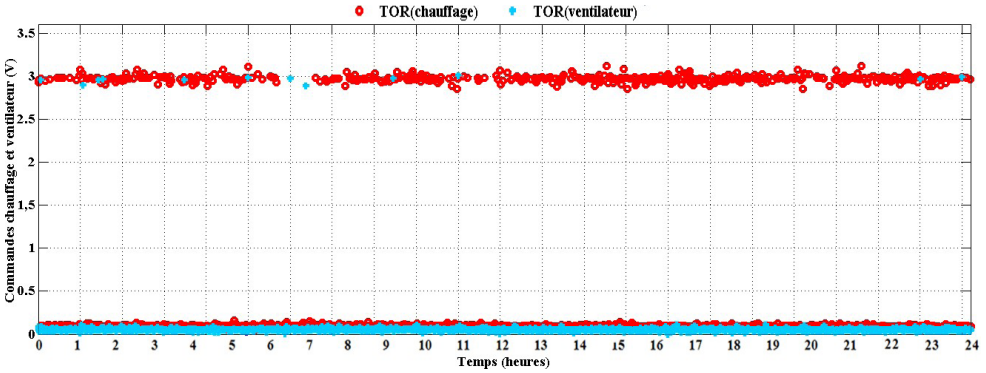

Figure 3. Evolution of heating and ventilation controls.

It can be seen that the two controls work alternately and that more heating is consumed because the outdoor temperature is very low. This large number of switching operations is the result of the effect of the disturbances imposed by the outside environment as well as the setpoint adjustment. We propose to solve the set point problem by adding several control steps, Figures 4 and 5 represent respectively the evolution of the controlled temperature and the evolution of the digital control inside the greenhouse during three hours.

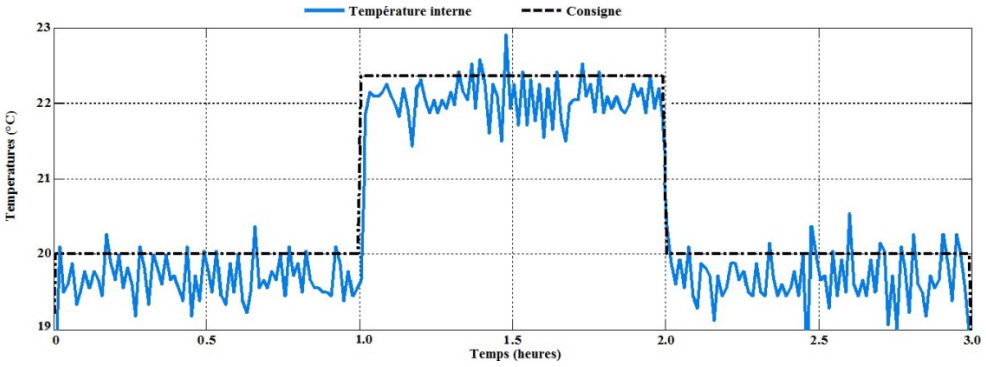

Figure 4. Setpoint and temperature over the interval [0, 3] h.

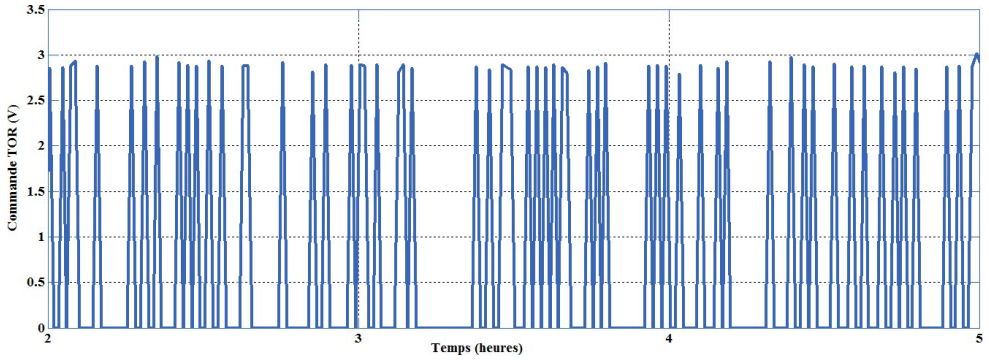

Figure 5. Digital control over the range [0, 3] h

It can be seen that the temperature evolution corresponds well to the set point, with a short rise time and a practically uniform static gain. However, there are too many transitions between heating and ventilation, which leads to poor energy use. Therefore, we need to use other means of progressive control to minimise the power consumption.

Implementation of the PID controller

In this section, we propose to establish a mathematical model of the internal temperature progression using the Broïda method. To simulate this evolution, we introduced a 3V step at the input of the open loop system to start the heating. We then determined the time response, and found that the initial temperature was 17°C and that it stabilised at 35.3°C

In order to be able to calculate the DC transfer function corresponding to the evolution of the internal temperature of the greenhouse, it is then necessary to calculate the pure time delay Tr and the time constant τ from the following Broïda equations:

$$T_r = 2.8t_1 - 1.8t_2 = 20.5(s) \text{ et } \tau = 5.5(t_2 - t_1) = 320(s) \quad (1)$$

This results in the following model.

$$F(P) = 6.17\frac{e^{-20.5}}{1+320P} \quad (2)$$

In order to validate the transfer function obtained, we simulated the index response in Matlab, as shown in Figure 6. We deduce that the transfer function thus obtained reflects the evolution of the internal temperature.

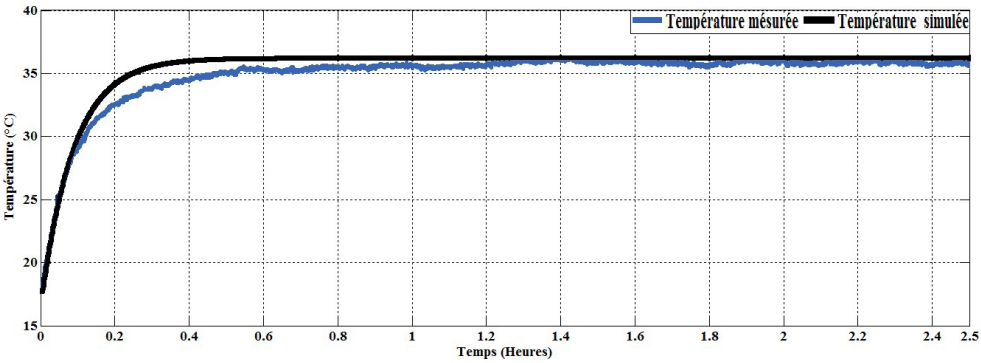

Figure 6. Simulation of the index response of the internal temperature in open loop.

In the following, we will use the transfer function assuming that the initial value of the internal temperature is zero since it is variable throughout the year. Our main goal is to control the temperature regardless of the choice of the initial temperature. Then, based on the different parameters identified, the gains of the PID control parameters are calculated by applying the following formulas:

$$\begin{cases} K_p = \dfrac{\dfrac{\tau}{T}+0.45}{1.2K} = 2.15 \\ k_i = \dfrac{0.75}{KT} = 0.005 \\ k_d = \dfrac{0.36\,\tau}{K} = 18.10 \end{cases} \tag{3}$$

These parameters were used to control the temperature in the greenhouse. We excited the system through several steps to ensure the controller worked properly.

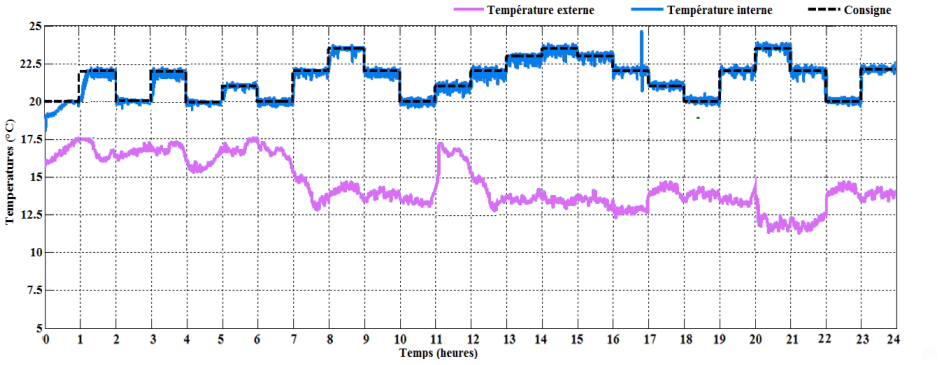

Figure 7. Temperature control in the greenhouse by PID

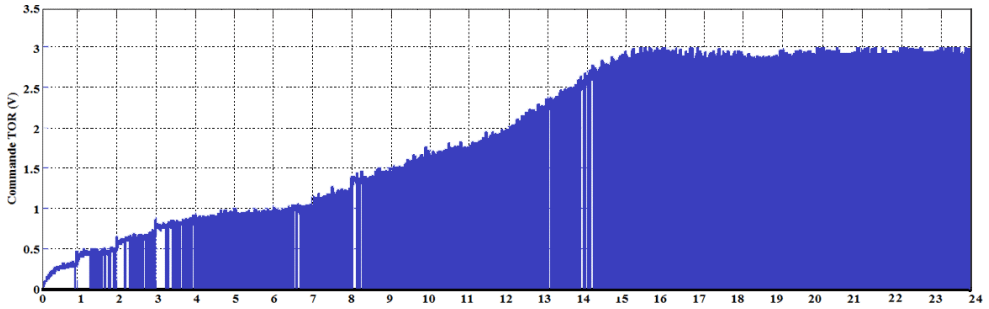

Figure 8. Evolution of PID control

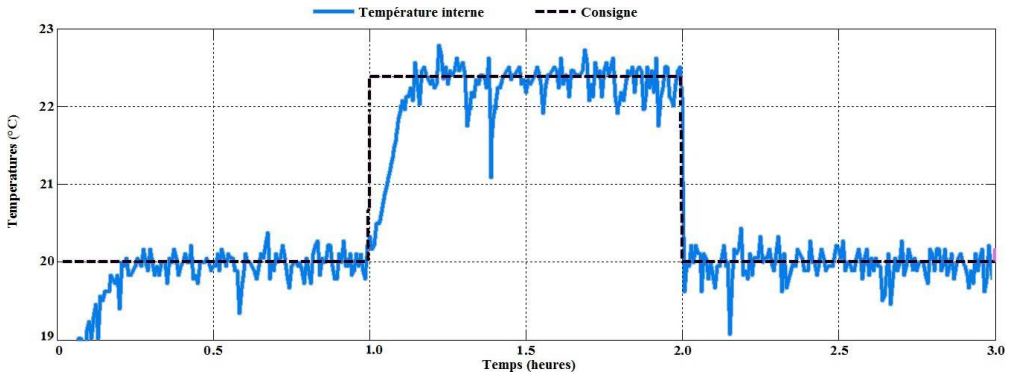

Figure 9. Temperature control using PID over the interval [0, 3] h.

Figure 9 shows the evolution of the controlled temperature over the period [0, 3] h. On this curve, it can be seen that there are fluctuations in the vicinity of the setpoint that do not exceed 0.5°C. These variations are caused by the external climatic parameters and by the lack of filtering of the input/output signals of the system.

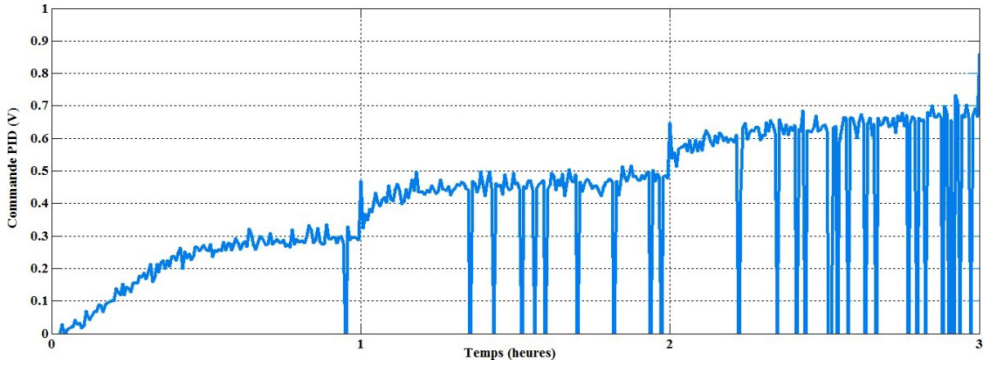

Figure 10. Evolution of the PID control over the interval [0, 3] h

Figure 10 shows the evolution of the control calculated with the PID controller. It can be seen that the control is progressive and is cancelled when the temperature reaches the desired value. It can also be seen that the temperature evolves in

accordance with the setpoint, with oscillations that do not exceed 1°C. These disturbances are mainly caused by the equipment used and external influences. PID control has been successful, but is still sensitive to the interference caused by the wide fluctuation of external weather parameters. Furthermore, it is based on a specific identification method for well-defined climatic conditions. This is why we observe saturations on the command to the actuators (Figure 8).

Implementation of *Fuzzy Logic*

We have one input variable: temperror which is actually the difference between the indoor temperature and the set point. We have two output variables: heating and fan (Figure 11).

For technological reasons, each variable has its own range of variation, which will be presented in the "FIS EDITOR" window:

- For inputs: Temperror varies from -10 to +10.
- For outings :

Heating from 0 to +100% (100% corresponds to the maximum speed of the motor).

Fan from 0 to +100% (100% corresponds to the maximum speed of the motor).

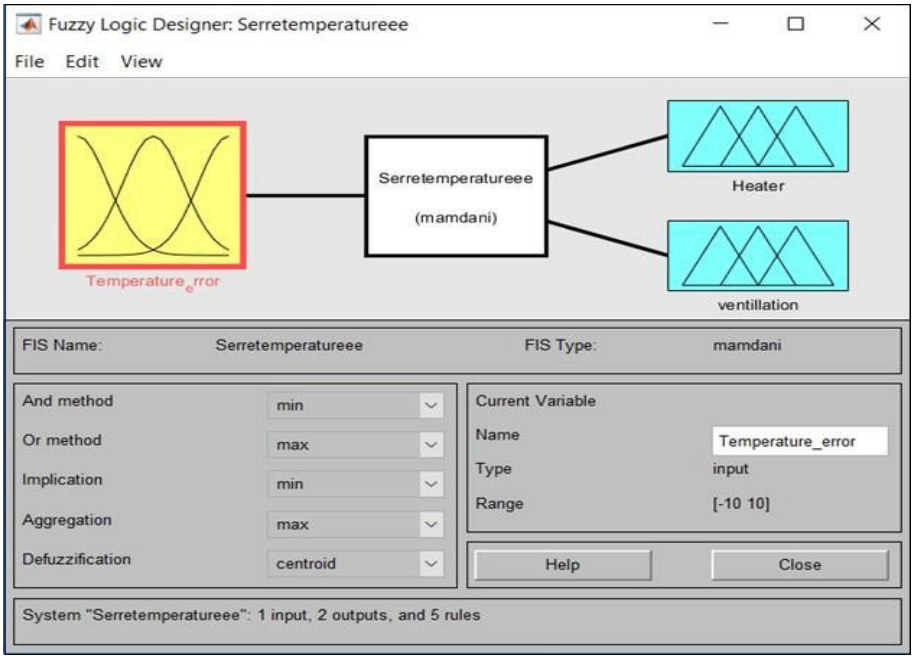

Figure 11. The inputs/outputs of our system on the FIS Editor window.

Fuzzification of Variables

In the following we will establish the ranges of variation (the fuzzy sets), define the membership functions for the inputs and outputs and give each element of the membership function a meaningful name as shown in Figure 12.

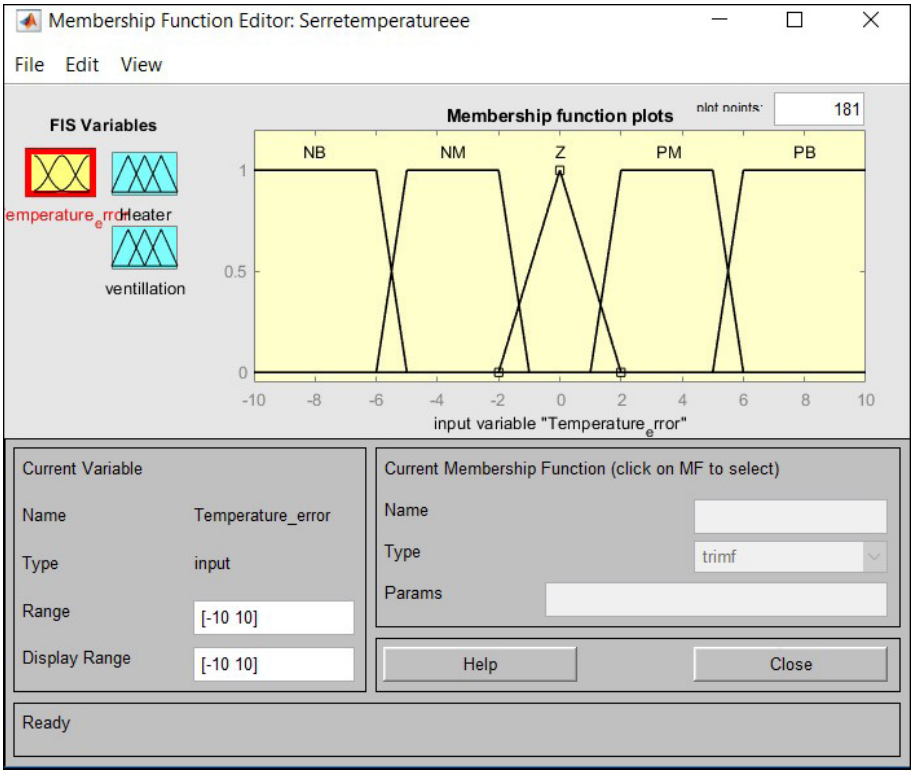

Figure 12. The temperror membership function.

For the input we chose four trapezoidal shaped fuzzy sets and one triangular shaped set: (NB: Negative Large; NM: Negative Medium; Z: Zero; PM: Positive Medium and PB: Positive Large). For the output we have chosen four trapezoidal and one triangular fuzzy sets for the heater and the fan respectively: (VL: very low speed; L: low speed; M: medium speed; H: high speed and VH: very high speed). As shown in Figure 13.

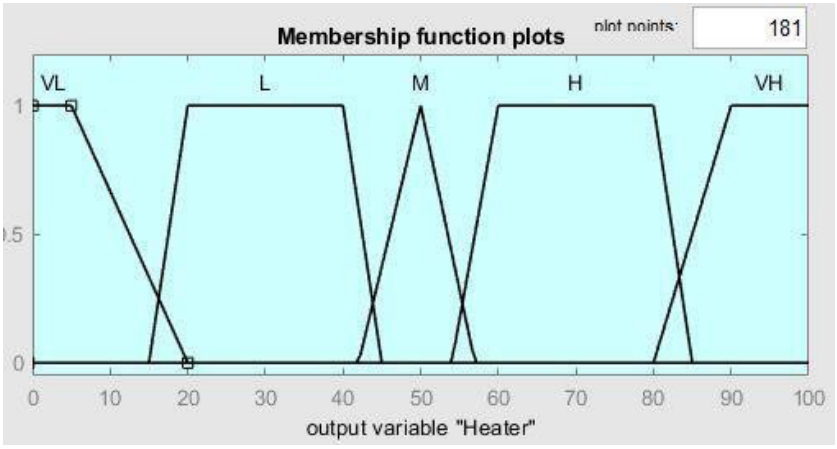

Figure 13. Fuzzy sets for heating.

Inference Rules

After defining the different membership functions, we implemented our inference rules (Figure 14), with the aim of realising the operating requirements of our system, For example: If (temperror is NB i.e. the difference between the internal temperature and the setpoint is very small) then the controller will automatically activate the heater at the maximum speed VH and the fan at its minimum speed VL.

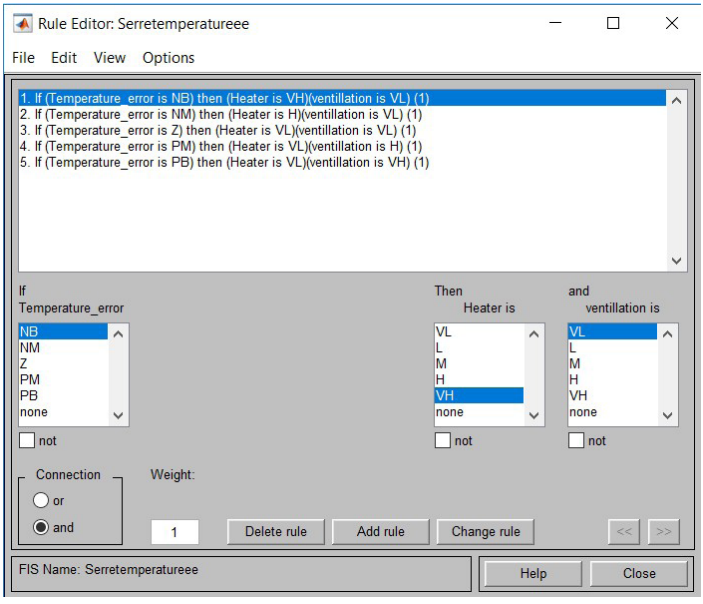

Figure 14 . Implementation of the inference rules.

Use of the Rule Viewer

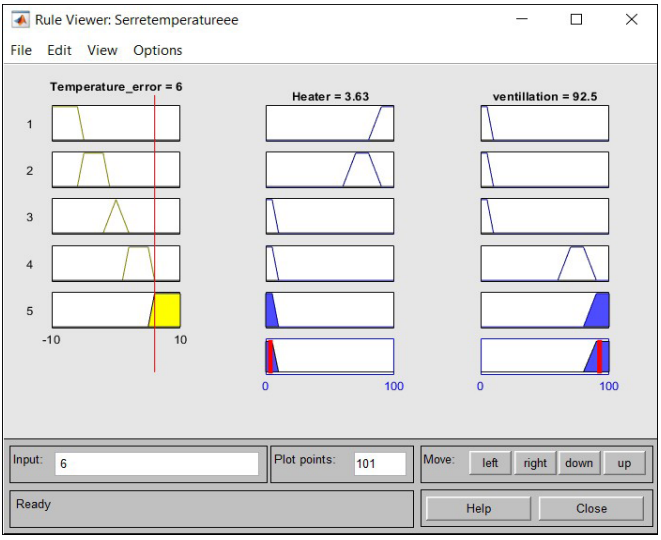

Figure 15. Rule viewer simulation of controller outputs.

The rule viewer is designed to simulate the system outputs by varying the inputs and is based on the inference rules implemented in the rule editor, e.g. for a temperature error of 6°C, the controller will activate the heater at 3.63% and the fan at 92.5%. The input value can be changed by dragging the marker with the mouse to see the influence on the defuzzed outputs.

The figure 16. illustrates the variation of the internal, external as well as the setpoint temperature. We see that the internal temperature evolves adequately with a very low rise time.

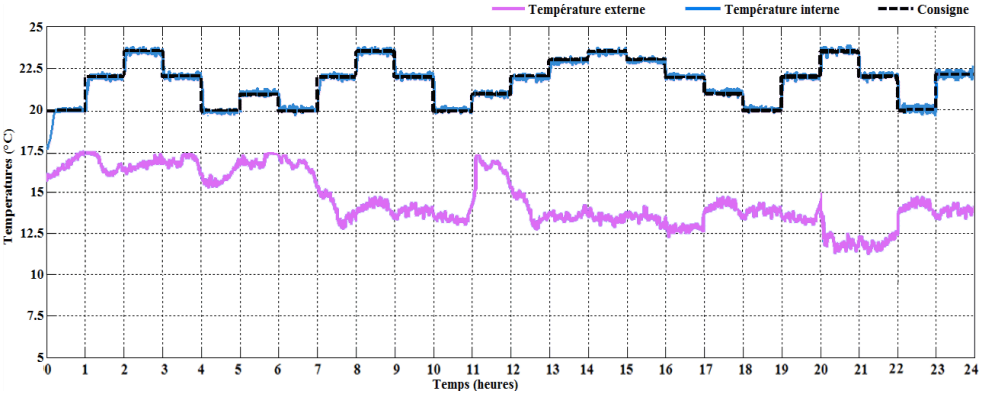

Figure 16. Internal temperature control by FLC

The figure 16. shows the variation in control exerted on the actuators. The pseudo-pulses shown there are from large setpoint derivations during the transition between operating points.

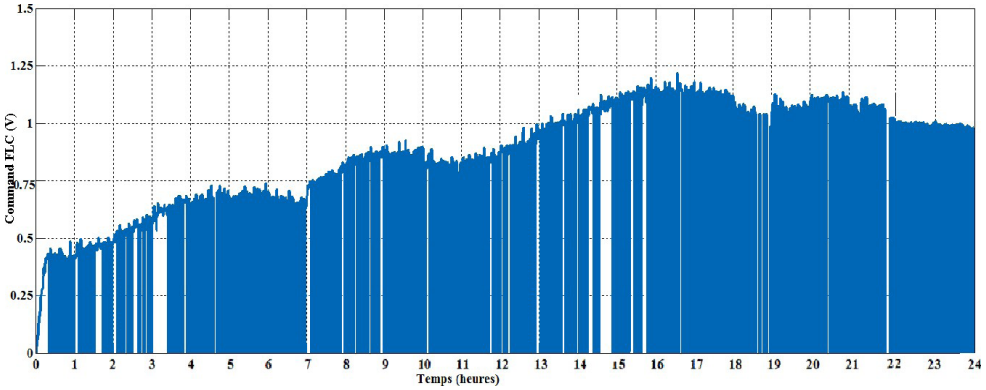

Figure 17. FLC process control

Figure 17, shows the variation of the internal temperature regulated over [0, 3] h, using the FLC. This temperature perfectly respects the set point with the minimum possible fluctuations.

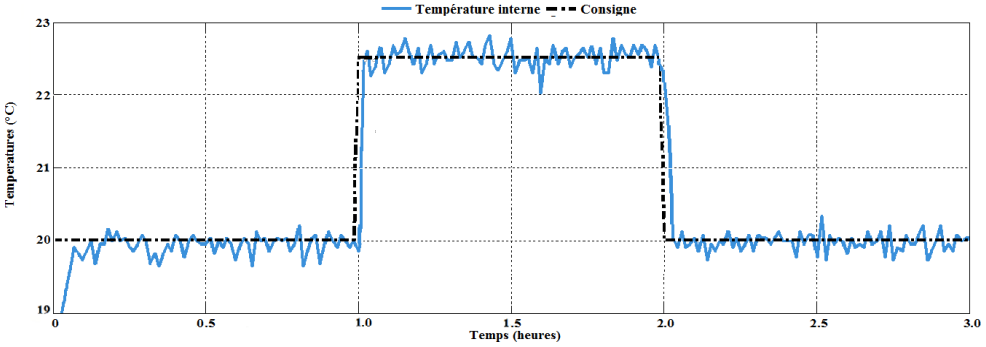

Figure 18. Temperature control over the interval [0, 3] h

Figure 18 shows the progression of the fuzzy control over [0,3] h. It is smoother than the previous control modes and resets quickly to its minimum value as its rise time is very short.

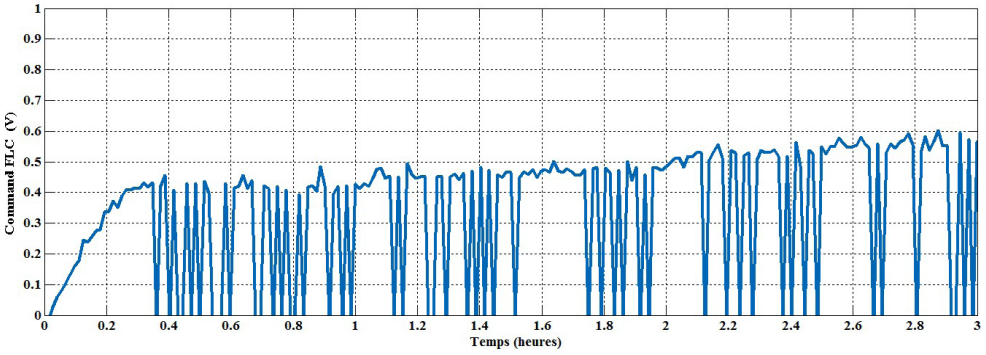

Figure 19. Evolution of the FLC command over the interval [0, 3] h

Choice of the Controller

The perfect controller does not really exist, and therefore a compromise must be found between the various desired specifications, such as the speed of the system, its accuracy, its robustness, its repeatability due to a change in the setpoint or to external disturbances.

In this section of the chapter, we will present the comparison of the experiments carried out on the different controllers used, such as the TOR, PID and FLC.

In order to compare the temporal results recorded for the different temperature ranges, we will focus on the index responses obtained for the first three hours, presented in figures (4, 10, 19), in order to simplify the reading and understanding of the curves. These figures allow us to visualise the variation of the internal temperature during the same period of time and applying the same external climatic conditions but using different regulation modes.

All of the controllers used in this work were able to control the internal temperature in the greenhouse. Indeed, we found that the temperature level in the greenhouse was kept within the desired range and fluctuated around the set points.

The method of control by means of the TOR technique has shown that temperature control in the greenhouse is not a recommended technique as the exhaustive external disturbances involved numerous switches and transitions between the different actuators and this technique has several fluctuations, and this represents a major shortcoming, especially in terms of the life of the equipment and the poor management of the energy consumed

On the other hand, by observing these figures which illustrate the evolution of the control system used, we note that the PID control has a very high power consumption to reach the target set. Indeed, we notice that this control is cancelled late compared to other types of controllers and that the number of resets is relatively low.

Furthermore, its value does not exceed 0.75 (V) during the very first three hours of regulation. The PID reach a maximum value that exceeds 1.3V and does not guarantee reliability performance in the presence of excessive variations in external parameters. Indeed, this technique requires a very precise and restricted operating time. The main interest in implementing this technique is to find a mathematical model that is as valid as possible.

It is also very important to emphasise that the PID become saturated after a few hours due to strong external climatic disturbances.

CONCLUSION

In this chapter book, we have first presented some notions on automatic control. Then, we described the operation of discrete, PID and fuzzy controls.

Then, we used the Matlab Simulink software to simulate the temperature in the greenhouse using the different control techniques.

Finally, we compared these controllers in order to choose the appropriate controller for the types of non-linear systems that have strong external disturbances.

ACKNOWLEDGMENT

I gratefully acknowledge the support and generosity of ALH institute, without which the present study could not have been completed.

REFERENCES

[1] IRENA. Renewable energy in the water, energy and food nexus, Int. Renew. Energy Agency, 2015, 1–125.

[2] A. CHOUCHAINE, E. FEKI, A. MAMI, 2011 Stabilization using a discrete fuzzy PDC control with PID controllers and pole placement: application to an experimental greenhouse, J. Control Sci. Eng. 2011 1–9, http://dx.doi.org/10.1155/537491.

[3] BELKADI, A., MEZGHANI, D. AND MAMI, A.. "Design and implementation of flc applied to a smart greenhouse", Engenharia Agricola 2020, 42 no6 pp. 135-142. Doi: 10.1590/1809-4430-Eng.Agric. 2020, v40n6p777-790/2020.

[4] Ma, D., Carpenter, n., Maki, h., Rehman, T. U Tuinstra, M. R., & Jin, J. Greenhouse environment modeling and simulation for microclimate control. Computers and Electronics inAgriculture, 162, 2019, 134–142. doi:10.1016/j.compag.2019.04.013.

[5] Anouar Belkadi, Dhafer Mezghanni, and Abdelkader Mami, "Energy design and optimization of a greenhouse: a heating, cooling and lighting study", Engineering, Technology & Applied Science Research, 2019, 9 pp. 4235-4242 (3).

[6] Ahemd, H.A., AL-Faraj, A.A., ABDEL-GHANY, A.M., (2016). Shading greenhouses to improve the microclimate, energy and water saving in hot regions: a review. Sci. Horticult. 2016, 201, 36–45.

[7] Anouar Belkadi, Dhafer Mezghanni, and Abdelkader Mami, "IOT AND LIGHTING CONTROL FOR SMART GREENHOUSE", 7ème Conference Internationale des Energies Renouvelables CIER-2019 - Proceedings of Engineering & Technology -PET-, December 2019, Vol. 59

[8] GE, Y., BAI, G., STOERGER, V., SCHNABLE, J.C., Temporal dynamics of maize plant growth, water use, and leaf water content using automated high throughput RGB and hyperspectral imaging. Comput. Electron. Agric. 2016, 127, 625–632.

[9] Anouar Belkadi, Dhafer Mezghanni, and Abdelkader Mami, "IOT AND LIGHTING CONTROL FOR SMART GREENHOUSE", 7ème Conference Internationale des Energies Renouvelables CIER-2019 - Proceedings of Engineering & Technology -PET-, December 2019, Vol. 59

[10] A. PAWLOWSKI, M. BESCHI, J.L. GUZMAN, A. VISIOLI, M. BERENGUEL, S. DORMIDO, Application of SSOD-PI and PI-SSOD event-based controllers to greenhouse climatic control, ISA Trans. 65, 2016, 525–536, http://dx.doi.org/10.1016/j.isatra.

[11] Anouar Belkadi, Dhafer Mezghanni, and Abdelkader Mami, "IOT AND LIGHTING CONTROL FOR SMART GREENHOUSE", 7ème Conference Internationale des Energies Renouvelables CIER-2019 - Proceedings of Engineering & Technology -PET-, December 2019, Vol. 59

[12] S. MOHAMED, I.A. HAMEED, 2014; A GA-based adaptive neuro-fuzzy controller for greenhouse climate control system, Alex. Eng. J., 2016, http://dx.doi.org/10.1016/j.aej.

[13] Anouar Belkadi, Dhafer Mezghanni, and Abdelkader Mami, "ENERGY OPTIMIZATION OF GREENHOUSE", 7ème Conference Internationale sur l'énergie verte et l'ingénierie environnementale (GEEE-2020) - Proceedings of Engineering & Technology -PET-, 2020 Vol. 63 pp, 46-56.

[14] Anouar Belkadi, Dhafer Mezghanni, and Abdelkader Mami, "ENERGY STUDY OF A GREENHOUSE AND OPTIMISATION OF THE CHOICE OF ITS SHAPE AND COVERING MATERIAL: BASED ON AN IMPROVED STATIC MODEL Engenharia Agricola, 2021, 41 no3 pp. 297-310. Doi: 10.1590/1809-4430-Eng.Agric.v41n3p297-310/2021 .

[15] D.M. ATIA, H.T. EL-MADANY,; Analysis and design of greenhouse temperature control usingadaptive neuro-fuzzy inference system, J. Electr. Syst. Inf. Technol, 2016, http://dx.doi.org/10.1016/j.jesit.

[16] Anouar Belkadi, Dhafer Mezghanni, and Abdelkader Mami, "ENERGY OPTIMIZATION OF A GREENHOUSE", 7ème Conference Internationale des Energies Renouvelables CIER-2019 - Proceedings of Engineering & Technology -PET-, December 2019, Vol. 59. Poster

Chapter 9

INVESTIGATION OF THE EFFECTS OF DIFFERENT TEMPERATURE PERFORMANCE TYPES OF MAGNET ON MOTOR PERFORMANCE PARAMETERS IN PMBLDC GEARLESS MOTOR FROM ELECTRIC VEHICLE TRACTION MOTORS

Murat TOREN[1], Hakki MOLLAHASAOGLU[1], Sebahattin Efe TORAN[1]

1 Recep Tayyip Erdogan University, Faculty of Engineering And Architecture, Department of Electrical and Electronic Engineering, Rize, Türkiye

INTRODUCTION

In recent years, fossil fuel and greenhouse gas emissions have been high in our country and in the world. One of the reasons for this is the high number of vehicles with internal combustion motors used in transportation. Therefore, the automobile industry is switching to electric vehicle transport. The main advantages of EVs are their low emissions, quiet operation and high efficiency. The reason for these advantages in EVs is the electric motors used. The type of electric motor is of great importance in regulating the operating characteristics of the vehicle. Asynchronous motors, direct current (DC) motors, brushless DA motors, permanent magnet synchronous motors and switched reluctance motors are the main types of electric motors preferred in EVs [1]. In the chapter, the examination of various types of electric motors used in EVs, the number of uses and the estimation for the coming periods are made [2]. Looking at these studies, it is seen that BLDC motors are widely used in EVs due to their high power density, high efficiency and easier control [3]. In addition, by using permanent magnets instead of rotor windings in the motor structure, BLDC can become more compact and produce high power-torque density [4]. For PMBLDC motor supervision [5] and drive [6] are being studied. Looking at such studies, it is seen that single [7] inverters are used for the control and supervision of electric vehicle applications, or individual inverters [8] are used to control the torque of each motor separately. Apart from these, methods called phase advance and hold control are also used [9]. However, studies on optimum torque and efficiency performance for PMBLDC are more popular [10]. In particular, permanent magnet and rotor configurations strongly influence the torque and efficiency performance of permanent magnet electric motors. In the chapter, different rotor configurations of the BLDC motor with 35 kW Halbach array fixed magnet were compared and evaluated. Finite element technique was used to analyze and compare different geometry parameters and rotor magnet configurations to improve efficiency and torque performance [11]. In a different study using the finite element technique, a comparative analysis is performed for eight different model designs of PM BLDC motor with ferrite magnet. As a result of the comparison, it is proven that the reference design has a lower knock torque and a lower drive torque compared to other motor designs [12]. One of the areas where PMBLDC motors are studied for efficiency and high torque capacity is the permanent magnet types in their structure. Alnico, Ferrite (ceramic), SmCo and NdFeB magnets are used in PMBLDC motors. However, among these types of magnets, boron (NdFeB) magnets, which consist of rare earth elements, neodymium, iron and elements of different densities, are widely preferred because they provide a good magnetic field per volume. The reference study compares the performance of NdFeB magnet types with different power densities (N28-N35-N52). As a result of the study, N52 type magnets were found to have a higher torque and efficiency ratio than other types of magnets [13]. In a different study, the performance and cost of the 3-phase

PMBLDC motor are investigated using the finite element method. In the comparison made using NdFeB and ferrite magnets, it is determined that the motor with Ferrite magnet is heavier and more costly than the NdFeB magnet motor [14].

However, in this chapter, the performance effects of NdFeB type N35 magnet types with different performances at different temperatures, which are widely used in PMBLDC gearless motor structure and can be used in traction motors of EVs, are examined. Effects of magnets on the engine; It is aimed to generate data for magnet selection in motor design by obtaining the effects of performance parameters output power, torque and efficiency at temperatures of 20°C, 60°C and 100°C.

Permanent Magnet Brushless Direct Current Motors (PMBLDC)

Nowadays, PMBLDC motors are preferred in many applications, especially in EVs. These motors have advantages such as long operating life, very small RF noise compared to the traditional brushed direct current motor, low maintenance cost and no arcing, higher efficiency and ability to go to very high speeds, and high dynamic response [15]. These motors are equipped with a coil-wound stator that generates a fixed, single or multipolar electromagnetic field and a movable rotor part with a fixed magnet. There's an air gap between the stator and the rotor. The coils are wound into the stator slots in the motor. The PMBLDC motors are classified according to their gear condition and rotor structure. Figure 1 shows the classification of these motors.

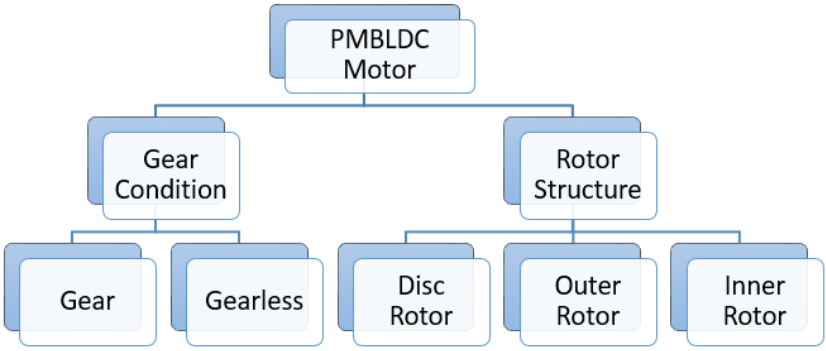

Figure 1. Classification of PMBLDC motors

In PMBLDC gearless motors, the rotor as a whole is moved by copper windings fixed to the rotor shaft. Thus, friction losses are reduced as there will be no friction. In addition, its regenerative braking feature leads to the preference of the gearless motor in EVs. In geared PMBLDC motors, the motor is connected to the stator with a gear reduction system. Although high torque and efficiency are achieved by means of geared structure, the losses of these motors are high and require more maintenance.

PMBLDC motors consist of a fixed magnet rotor and a stator with windings placed on it. However, the stator structure with windings made to produce a sinusoidal flux

density in the air gap of the machine is similar to that of an asynchronous motor. The stator structure consists of an outer body and a core with windings. The windings can be distributed windings or undistributed windings according to the stator design. In the stator, 3-phase windings are wound in the stator core. As with the three-phase induction motors from the stator windings in the BLDC motor, a rotating magnetic field is generated when the alternating current passes, allowing the rotor to rotate. The magnets could be embedded in the inner rotor, surface mounted, or in a Halbach array. The general structure of the PMBLDC motor and the frequently used types of magnets according to their placement in the rotor are given in Figure 2.

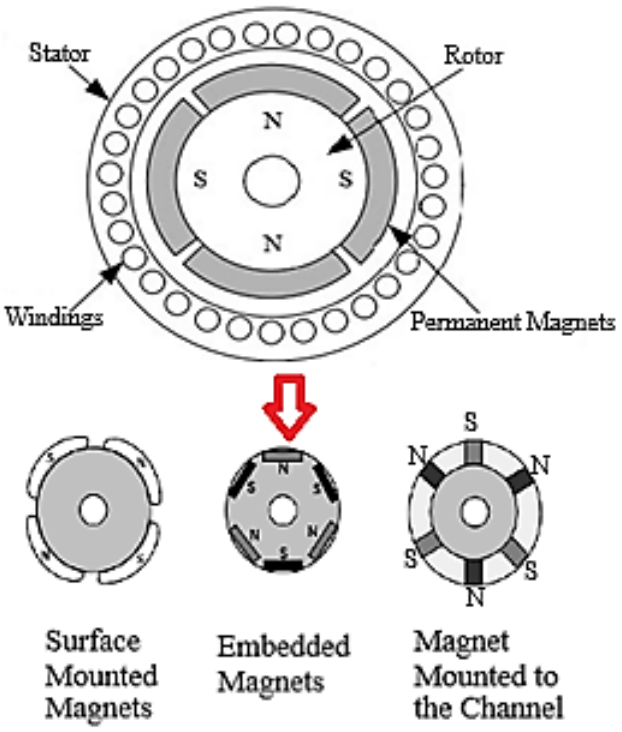

Figure 2. The general structure of the PMBLDC motor

PMBLDC motors consist of permanent magnet rotor and stator. The magnets are placed between the magnetic material brushes of the pole pieces in the rotor. The performance evaluation of magnets used in FDA motors utilizes the motor's magnetic equivalent electrical circuit. Figure 3 shows the magnetic equivalent circuit of the PMBLDC motor.

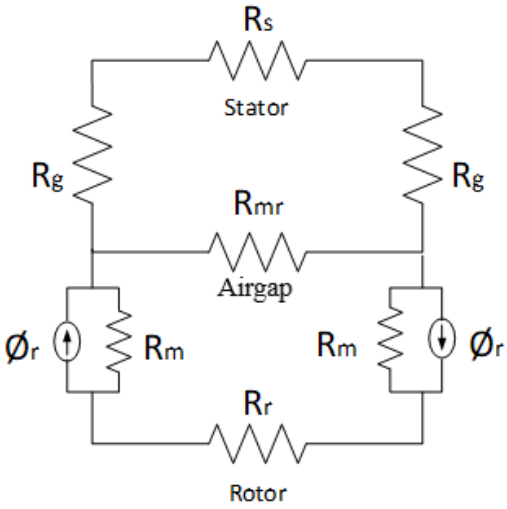

Figure 3. PMBLDC gearless motor magnetic equivalent circuit

The performance of the permanent magnet determined using the magnetic equivalent circuit given in Figure 3 depends on the type, characteristics and size of the magnet. In the position where the magnet is located, the equivalent consists of a flux source ($\emptyset_r$) and a parallel internal reluctance value (R_m), and the magnetic flux value in the equivalent expression is expressed by Equation 1.

$$\emptyset_r = B_r * A_{mk} \quad (1)$$

Here $\emptyset_r$, B_r ve A_{mk} refer to the magnetic flux produced by the magnet, the permanent flux density of the magnet and the cross-sectional area of the magnet, respectively. The cross-sectional area is given in Equation 2.

$$A_{mk} = W_{mk} * \mathrm{L} \quad (2)$$

In Equation 2, W_{mk} refers to the width of the magnet and L the length of the package. Here, it can be seen that the size of the magnet is associated with the magnetic flux, and therefore to the motor performance. In addition, the reluctance value given in the equivalent circuit of the magnet is determined with Equation 3.

$$\emptyset_r = B_r * A_{mk} \quad (3)$$

Here, h_m, refers to the length of the magnet, μ_0 the magnetic permeability of the air gap, μ_r the magnetic permeability of the magnet. The air gap reluctance value in the magnetic equivalent circuit is given in Equation 4.

$$\emptyset_r = B_r * A_{mk} \quad (4)$$

In Equation 4, $\mathrm{R}_g, g, k_{cs}, D_{ms}$ and α_{mk}; refer to air gap reluctance, air gap length, crankcase coefficient, magnet surface diameter and magnet surface angle, respectively.

When all these equations are examined, it is seen that the performance values of PMBLDC motors depend on the permanent magnet parameters used in the motors. In addition, in the design of PMBLDC motors, the choice of the housing-pole combination of the motor as well as the magnet design is important.

FINDINGS AND RESULTS

The higher the degree of the magnet (the number after 'N'), the stronger the magnet becomes. Any letter following the degree refers to the degree of temperature of the magnet. If there is no letter following the degree, the magnet is at the standard temperature. Temperature values standards are determined as M-H-SH-UH-EH and AH [16]. The temperature degree of each class is different according to the maximum operating temperatures and the maximum temperature values called Curie temperature, where the magnet loses its permanent magnetism feature, and these values are given in Table 1.

Table 1. Operating and curie temperatures of NDFEB magnets.

Magnets Type	Max. Operating Temperature (°C)	Curie Temperature (°C)
N	80	310
NM	100	340
NH	120	340
NSH	150	340
NUH	180	350
NEH	200	350
NAH	220	350

Permanent magnets are classified according to where they are used in the industrial area and according to their working and best performance temperatures. These classes (AH, EH, H, M, MX, SH, SHX, UH, X, etc.) also show the strength of the magnet in the magnetic field. In this chapter, the technical characteristics and parameters of the PMBLDC motor with N35 type permanent magnet are given in Table 2.

Table 2. The gearless PMBLDC motor basic parameters.

Parameters	Values
Current	24 A
Voltage	110 V
Continuous power	2,45 kW
Peak power	8 kW
Continuous Torque	52 Nm
Peak torque	345 Nm
Frequency	400 Hz
Base speed	200 rpm
Maximum speed	395 rpm
Poles	16

The model of the PMBLDC gearless motor designed in the Anssys Maxwell analysis program is given in Figure 4. Here, steel 1008 material was used in the core of the motor, and the stator groove structure is given in Figure 4. N35 type magnet was used in the rotor groove part of the motor and its geometry was designed.

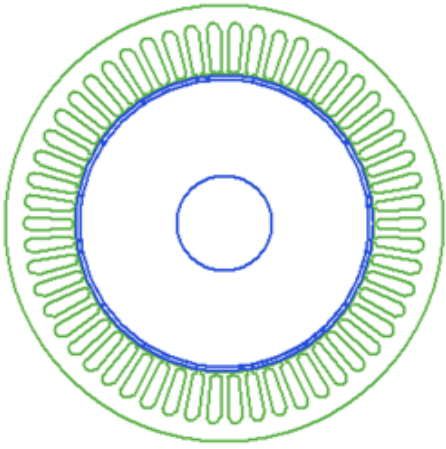

Figure 4. A PMBLDC gearless motor schemes

In the chapter, the effects of types of NdFeB type magnet group element produced with N35 type rare earth elements used in the rotor structure of PMBLDC gearless motor with different performance values at different temperature values, when the ambient temperature value is 20 °C and at 60°C and 100 °C, which they can reach during operation on motor performance parameters were determined. In the Anysy Maxwell analysis of the motor, mesh was assigned to the surfaces every 0.0092 mm interval for magnetic analysis. The view of geometry designed for electromagnetic analysis is as in Figure 5.

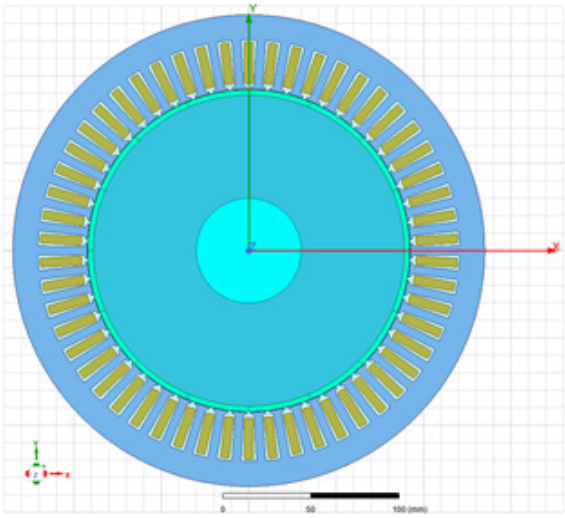

Figure 5. A PMBLDC gearless motor schemes (mesh)

The maximum speed values of the analyzed PMBLDC Gearless motor when the N35 magnet rotor structure is operating at 20 °C and then at 60 °C and 100 °C are given in Figure 6.

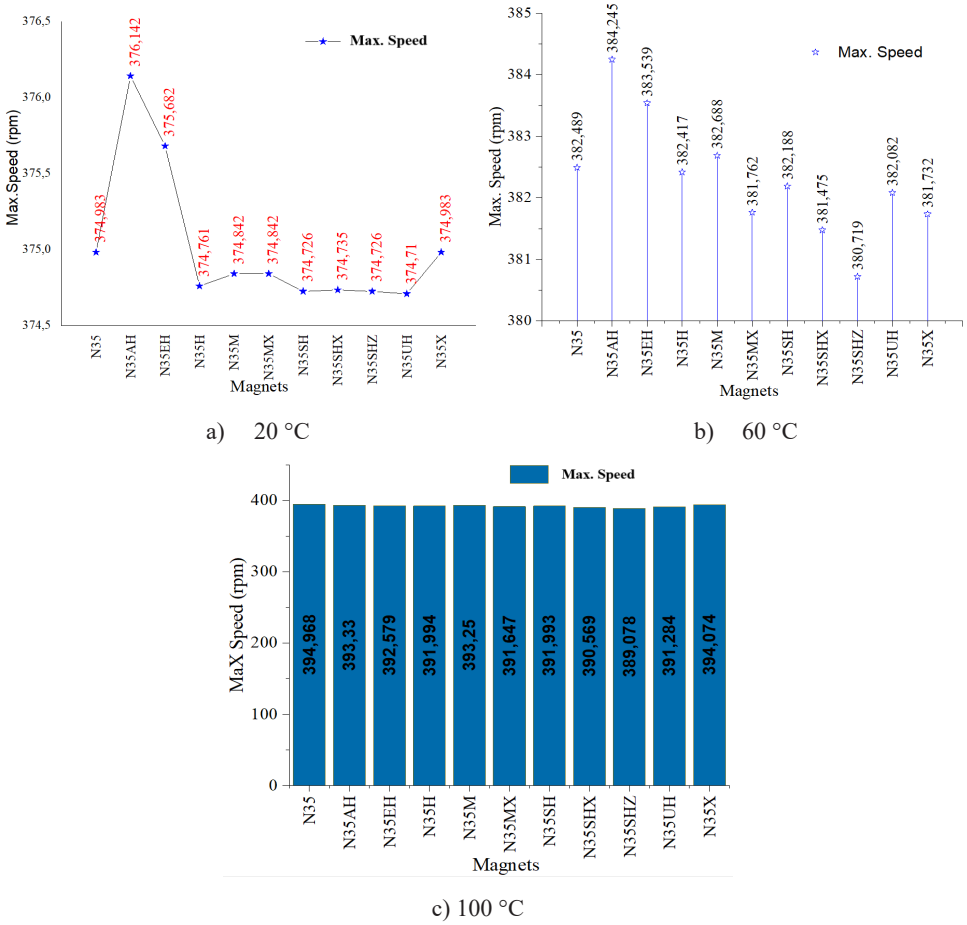

Figure 6. Effect of N35 type magnets with different temperature degrees used in PMBLCD Gearless motor on motor speed at different ambient temperatures

When Figure 6 is examined, it is seen that the effect of N35 type magnet with different temperature degrees used in PMBLDC gearless motors on motor speed varies in 20 °C, 60 °C and 100 °C ambient conditions. It is seen that N35AH magnets at 20 °C and 60 °C and N35 magnet at 100 °C provide higher speed performance. The performance difference of different types of these magnets at different temperatures confirms the formation of operating ranges according to the NdFeB type magnet temperature values given in Table 1.

Figure 7 shows the efficiency values of N35 type magnets with different temperature degrees used in PMBLDC Gearless motor at different ambient temperatures (20 °C, 60 °C and 100 °C).

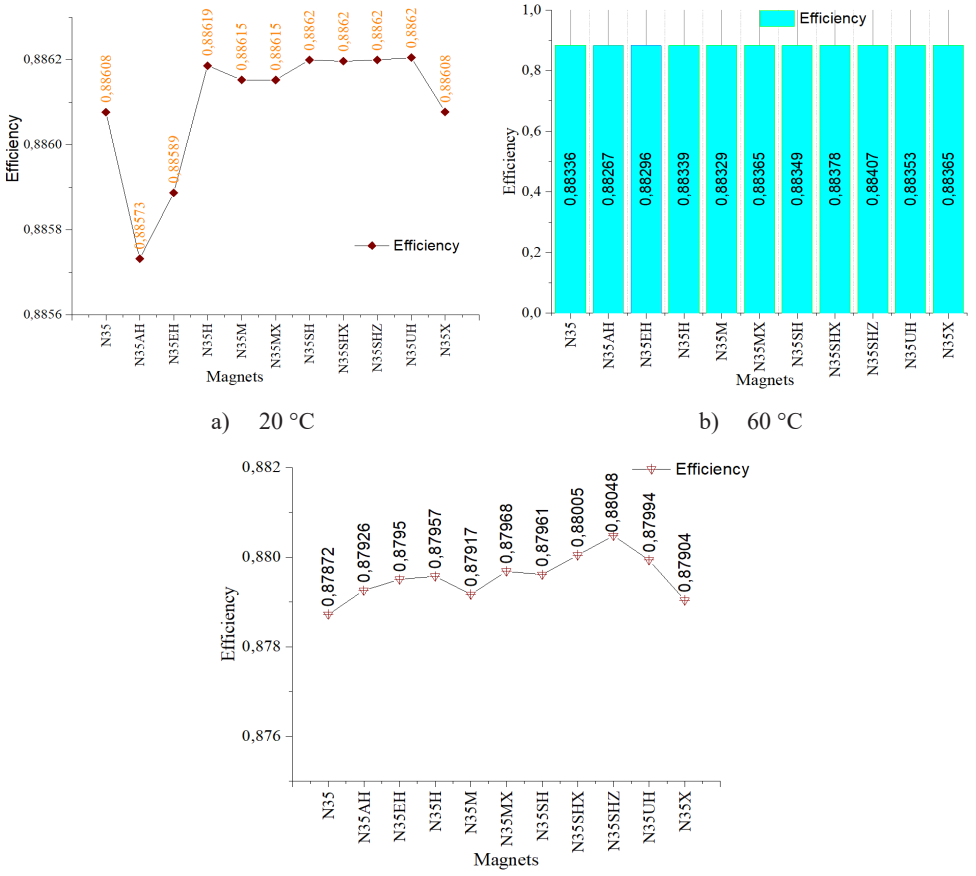

Figure 7. Effect of N35 type magnets with different temperature degrees used in PMBLCD Gearless motor on motor efficiency at different ambient temperatures

When the motor efficiency performance of the N35 type magnet with different temperature degrees used in PMBLDC Gearless motors under 20 °C, 60 °C and 100 °C ambient conditions is examined according to the data shown in Figure 7, it is determined that there is no very high rate of change but there are differences. Considering the maximum magnet operating temperatures of the PMBLDC Gearless motor operating at different ambient temperatures, it is seen that the efficiency performance of the N35SHZ type magnet of the N35 permanent magnet motor with a maximum operating temperature of 150°C is better than other types.

Figure 8 shows the effect of N35 type magnets with different temperature degrees used in PMBLDC Gearless motor on motor output power at different ambient temperatures (20 °C, 60 °C and 100 °C).

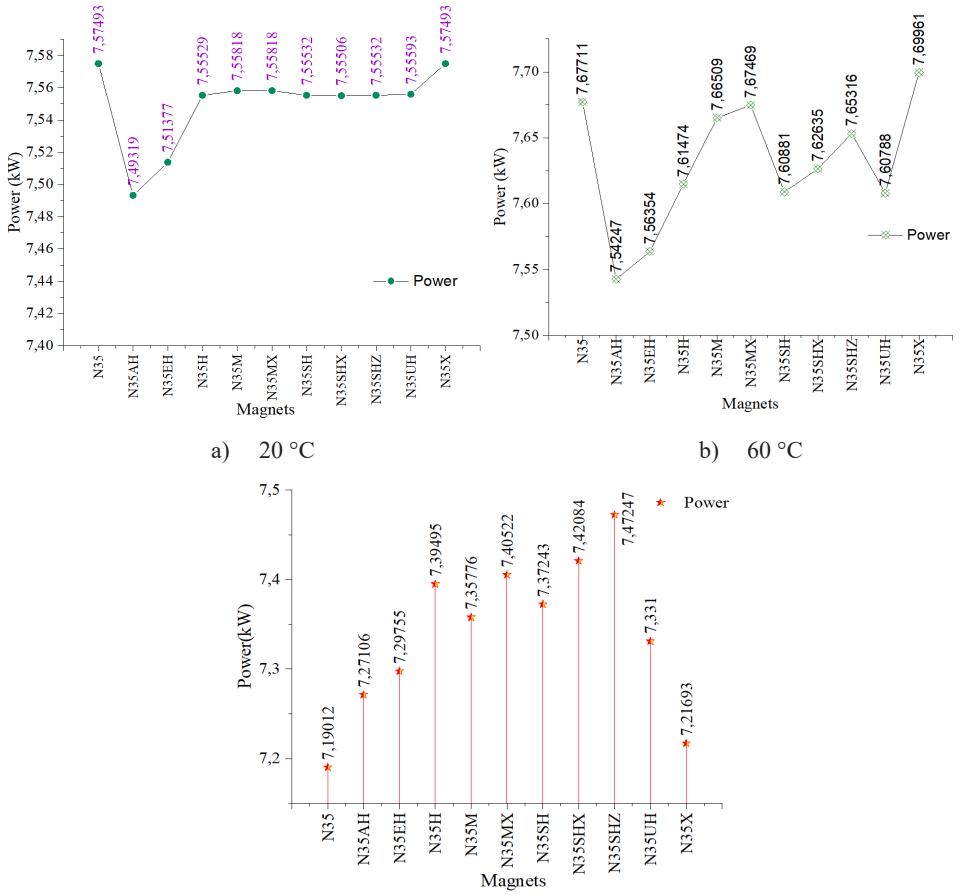

Figure 8. Effect of N35 type magnets with different temperature degrees used in PMBLCD Gearless motor on motor power at different ambient temperatures

In the PMBLCD Gearless motor with 8 kW label value, it is seen that the output power values differ in the effect of the N35 type magnet with different temperature degrees used in the motor on the motor performance at 20 °C, 60 °C and 100 °C temperature conditions. It is seen that the N35X type magnet at 20 °C and 60 °C operating conditions and the N35SHZ type magnet at 100 °C operating conditions are more effective in the power performance of the N35 permanent magnet motor. The effect of N35 type magnets with different temperature degrees used in PMBLDC Gearless motor on motor output torque at different ambient temperatures (20 °C, 60 °C and 100 °C) is given in Figure 9.

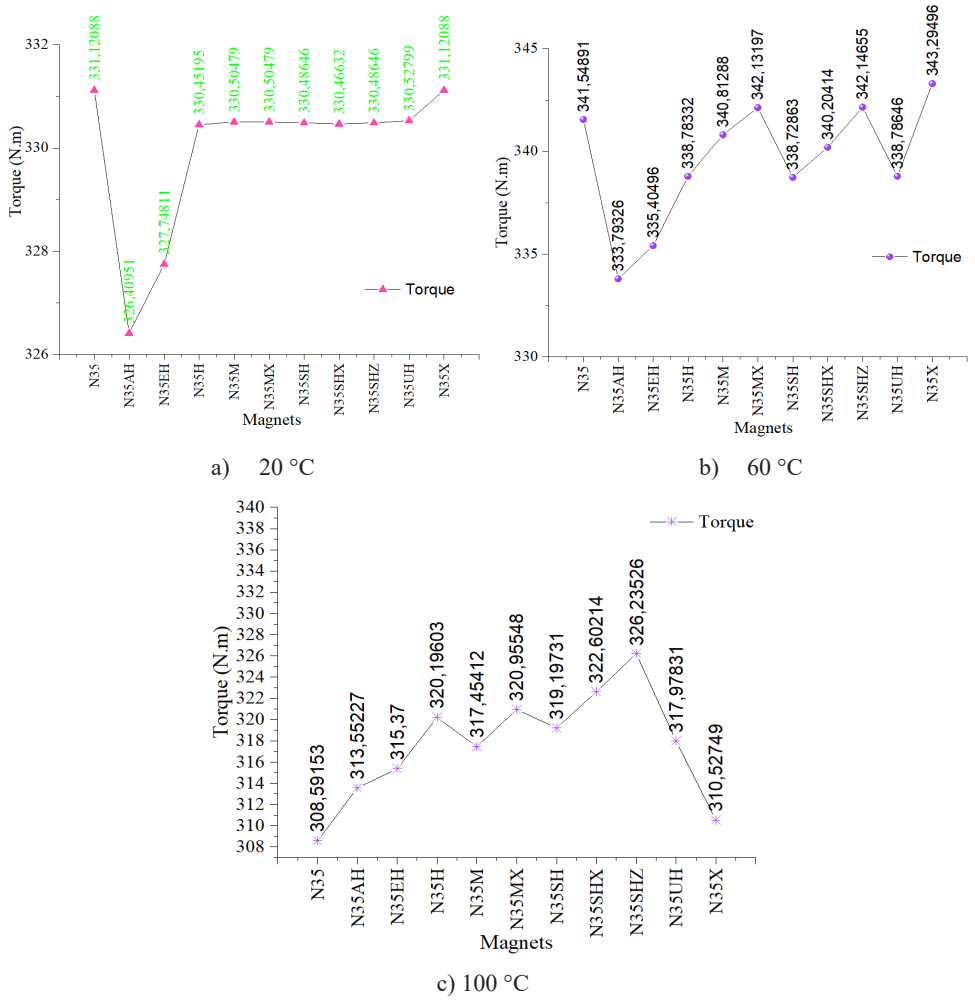

a) 20 °C

b) 60 °C

c) 100 °C

Figure 9. Effect of N35 type magnets with different temperature degrees used in PMBLCD Gearless motor on motor torque at different ambient temperatures

According to the label values of the prototype motor used in the chapter, it is determined that the torque values of the PMBLCD Gearless motor with a maximum torque value of 345Nm have an effect on the motor performance under 20 °C, 60 °C and 100 °C temperature conditions in the N35 type magnet with different temperature degrees used in the motor. Accordingly, it is seen that N35 and N35X type magnets are more effective at 20 °C and 60 °C operating conditions, and N35SHZ type magnet is more effective at the torque of N35 permanent magnet motor at 100 °C operating conditions.

CONCLUSIONS

The PMBLDC gearless motor with 8kW output power used in the chapter is one of the motor types that can be used as a traction motor in EVs with a simple structure in electric vehicle technology. Determining the parameters affecting the performance of this motor with more optimum values during the design phase is necessary to perform the system performance in the best way. In this chapter, it was tried to determine the effect of N35 magnet type, which is widely used in the motor structure that has an effect on the performance parameters of the motor that has an effect on the system performance, on the motor output parameters of the types that provide performance at different temperature values. It has been obtained that N35 magnet type produces the best power and torque values during motor operation at 20 °C and 60 °C, and N35 and N35X data at 100 °C, and N35SHZ at 100 °C. In addition, when the efficiency of the motor was evaluated, the best efficiency value was obtained in the N35SHZ magnet type in all of the 20 °C, 60 °C and 100 °C temperature data tested in the chapter. In addition, it has been determined that the maximum speed value of PMBLDC gearless motor during idling is reached at 20 °C and 60 °C with N35AH magnet type values, and at 100 °C with N35 magnet type values. According to these values, which temperature performance N35 type magnet can be used for N35 magnet type during design in EVs where PMBLDC gearless motor is used was determined according to the preferences sought.

REFERENCES

[1] H. Kaymaz and M. F. Demir , “Elektrikli Otomobiller için Çekiş Motor Tip Seçimi”, International Periodical of Recent Technologies in Applied Engineering, vol. 2, no. 1, pp. 35-41, Apr. 2020

[2] M. Toren and H. Mollahasanoglu , “Elektrikli ve Hibrit Araçlardaki Elektrik Motorlarının İçten Yanmalı Motorlarda Oluşan ⟦CO⟧_2 Emisyonunda Meydana Getireceği Değişimin Tahmini ve Verimliliğe Etkisi: Türkiye Örneklemesi”, El-Cezeri, vol. 9, no. 3, pp. 1082-1097, Sep. 2022, doi:10.31202/ecjse.1107454

[3] H. Lu, L. Zhang and W. Qu, “A New Torque Control Method for Torque Ripple Minimization of BLDC Motors with Un-Ideal Back EMF,” in IEEE Transactions on Power Electronics, vol. 23, no. 2, pp. 950-958, March 2008, doi: 10.1109/TPEL.2007.915667.

[4] A. Usman and B. S. Rajpurohit, “Time-Efficient Fault Diagnosis of a BLDC Motor Drive Deployed in Electric Vehicle Applications,” 2020 IEEE Global Humanitarian Technology Conference (GHTC), 2020, pp. 1-5, doi: 10.1109/GHTC46280.2020.9342941.

[5] M. S. Trivedi and R. K. Keshri, “Evaluation of Predictive Current Control Techniques for PM BLDC Motor in Stationary Plane,” in IEEE Access, vol. 8, pp. 46217-46228, 2020, doi: 10.1109/ACCESS.2020.2978695.

[6] N. Reddy T., V. R. Basam and M. R. Pasumarthi, “A New Method for Multi-loop Control Tuning of High Power PM-BLDC Motor Drive,” 2019 4th International Conference on Electrical, Electronics, Communication, Computer Technologies and Optimization Techniques (ICEECCOT), 2019, pp. 89-94, doi: 10.1109/ICEECCOT46775.2019.9114566.

[7] M. Ebadpour, M. B. B. Sharifian and E. Babaei, “Modeling and control of dual parallel BLDC motor drive system with single inverter,” 2017 International Electrical Engineering Congress (iEECON), 2017, pp. 1-4, doi: 10.1109/IEECON.2017.8075750.

[8] L. Popescu, L. Melcescu, L. Dumitran, A. Crăciunescu, and A. Stănescu , “Control analysis of a bi-motor electric traction system for energy and performance optimization”, AIP Conference Proceedings 2570, 040002 (2022) https://doi.org/10.1063/5.0099663

[9] L. Popescu, L. Melcescu, O. Craiu, A. Craciunescu and V. Bostan, “Phase Advance and Dwell Control Applied to a PM BLDC Motor for Increasing the Maximum Speed of an Electric Vehicle,” 2022 International Symposium on Power Electronics, Electrical Drives, Automation and Motion (SPEEDAM), 2022, pp. 850-855, doi: 10.1109/SPEEDAM53979.2022.9841974.

[10] L. Yang, W. Fu, D. Wu, T. Yang and J. Zhao, “Influence of Magnetic Hall Sensors on Slotless Permanent Magnet BLDC Motor,” 2021 IEEE 4th International Electrical and Energy Conference (CIEEC), 2021, pp. 1-5, doi: 10.1109/CIEEC50170.2021.9510949.

[11] D. B. Minh, V. D. Quoc, and P. N. Huy, “Efficiency Improvement of Permanent Magnet BLDC Motors for Electric Vehicles”, Eng. Technol. Appl. Sci. Res., vol. 11, no. 5, pp. 7615–7618, Oct. 2021

[12] K. Smółka, A. Firych-Nowacka, and S. Wiak, “Comparison of the Design of 3-Pole BLDC Actuators/Motors with a Rotor Based on a Single Permanent Magnet,” Sensors, vol. 22, no. 10, p. 3759, May 2022, doi: 10.3390/s22103759.

[13] M. Toren, “Comparatıve analysis of the magnet effects on the permanent magnet BLDC motor performance used in electric vehicles.” Electr Eng vol. 104, pp. 3411–3423, 2022 https://doi.org/10.1007/s00202-022-01536-1

[14] A. Saxena, “Performance and cost comparison of PM BLDC motors for ceiling fan,” 2014 IEEE International Conference on Power Electronics, Drives and Energy Systems (PEDES), 2014, pp. 1-5, doi: 10.1109/PEDES.2014.7042082.

[15] J. Feng, K. Liu, and Q. Wang “Scheme based on buck-converter with three-phase H-bridge combinations for high-speed BLDC motors in aerospace applications.” IET Electr Power Appl vol. 12, pp. 405–414, 2018. https://doi.org/10.1049/iet-epa.2017.0615

[16] K&J Magnetics. [Online]. Available: https://www.kjmagnetics.com/

Chapter 10

PREDICTION OF SOLAR POWER ENERGY BY USING THE ARIMA MODEL

Ali SHAN[1], Muhammad ZOHAIB[1], Huseyin Fuat ALSAN[2], Taner ARSAN[2]

1 Kadir Has University: Department of Electronics Engineering, Istanbul, Türkiye
2 Kadir Has University: Department of Computer Engineering, Istanbul, Türkiye

INTRODUCTION

As humanity knows, electricity demand is increasing daily, and fossil fuels are limited worldwide. Now engineers are trying to find other ways for most renewable energy sources to fulfill the electricity demand. Most people use photovoltaic solar energy, and the ratio of solar installations is increasing. Solar energy is clean energy and does not produce any pollutants, a natural process that converts sunlight rays directly into electricity.

Fossil fuels like petroleum and natural gas are costly, and the total amount decreases daily. The massive amount of fossil fuels will significantly affect our clean environment. In addition, researchers can see that present nuclear energy has almost reached its end, and it is unclear whether the new will supply the same amount of power or not [1].

Energy prediction is a topic that has been under consideration in power systems for a very long time. In power engineering, energy generation prediction allows us to organize our load according to our generation. The crucial point is how to make a prediction model based on existing data and forecast the value for the future for a certain period. Even with many kinds of provided models, forecasting is still unclear due to high accuracy requirements nowadays due to development in energy-saving and generation sectors [2].

In the literature, various methods are used for prediction, which can be separated into three fundamental classes: hybrid methods, conventional-statistical methods, and artificial intelligence models [3]. Traditionally through mathematical equations, the output was related to the inputs. This white box model is used for multiple regression, linear regression, and autoregressive moving averages (ARMA). Grey prediction is also another commonly used method. For more data sets, these algorithms can work and are very easy to implement. Still, their prediction precision will generally be low if it is compared with recent machine learning algorithms. State-of-the-art machine learning needs complex computations. It can give us strong learning ability and high accuracy. Black-box models are the second class of learning algorithms in which artificial intelligence methods are mainly used. Still, these methods are applicable and efficient for only data with undefined internal dynamics (linear and non-linear). There is another method called hybrid methods that combine two methods of optimization and artificial intelligent algorithms, which are very efficient and have high precision. However, due to their high computational complexity, they are less commonly used among researchers [4].

In 2001, a network name EUNITE planned a worldwide competition on electrical energy prediction problems. In which SVR (support vector regression) or SVM (support vector machine) outperforms all other algorithms [5]. Some latest research has realized that for time series prediction, Random Forest Regression (RFR) is also very useful and efficient; even in some data sets, it is better than SVM [6].

The forecasting algorithm known as ARIMA, or "Autoregressive Integrated Moving Average," is founded on the notion that past values of the time series alone can be used to predict future values. The ARIMA model is a time series model commonly studied in forecasting, and research is still ongoing to make it more efficient. Reasons for the recognition are the implementation's simplicity and the well-known Box Jenkins methodology [7, 8].

The remaining paper is organized as follows: Section II overviews machine learning methods. In section III, the methodology is defined. In section IV, the results of the proposed work are given. Moreover, in section V, the paper concludes with future work.

MACHINE LEARNING METHODS

Random Forest Regression

Several techniques have been used for prediction in the last few decades. One of the best methods used is random forest regression. In Random Forest (RF), many decision trees are generated. Every observation feeds every decision tree. The most occurring outcome for every observation is taken from the final output. For those classes, which are not cooperating in building trees, an error assessment is made, and this error is called out-of-bag errors, which are estimated and denoted in percentage [9].

Each decision split selects the feature randomly in an (RF). These randomly chosen features reduce the correlation between trees and result in it increasing our efficiency, and next, it improves our power of prediction. There are several advantages of random forest regression. The first is the overfitting problem; the second is that they are less sensitive to outliers. Finally, in the case of training data, feature importance is generated automatically [10].

Another motivation for random forest regression is to give us all the benefits researchers can get from decision trees. In addition, the involvement of more features like its voting scheme by which decisions are made, the use of bagging on samples, and a subset of random variables because of these different properties enable us to give good results compared to decision trees [11].

The random forest is suitable for high-dimensional data because it can handle all missing, continuous, binary, and categorical values. The ensemble scheme and bootstrapping make it possible to make Random Forests strong against the overfitting problem. As a result, the researchers do not need to trim the trees. Besides high prediction, Random Forest is highly efficient and parametric for different datasets. Random Forest is unique among other machine learning modules in terms of accuracy and prediction.

Random Forests magnify the number of trees by making them from different data subsets to eliminate the correlation or relationship of other trees. This process

is-called bagging. A technique used for the creation of training data by taking repetitive sampling randomly with the replacement of the original data set without removing or deleting any data selected from the input for the following data set:

$$\{h(x, \Theta_k),\ k\ =\ 1, \ldots, K\} \tag{1}$$

where Θ_k represents the same distribution random vector, maybe some of the data are never used, and some data be used more than any time. Thus, increasing our stability and increasing our prediction level. Figure 1 shows the configuration of Random Forests. A Random Forest functions by creating some decision trees throughout training times and outputting the means of the classes as the prediction of all the trees [12].

Support Vector Machines (SVM)

Vapnik and his team invented the support vector machine in 1995. Recently the yon basis base of Statistic Learning Theory (SLT), Structural Risk Minimization (SRM), and Support Vector Machine (SVM) have been able to solve regression and problems before it was only applied to classification problems [13]. Due to many promising and catching features and good empirical performance support, vector machines are becoming increasingly popular. For the different classification and regression applications, SVM helps us to analyze the data. SVM is broadly used due to the variety of explaining the non-linear problem. Even if our training data is small, researchers can use it for both regression tasks and classification tasks in terms of regression named Support Vector Regression (SVR).

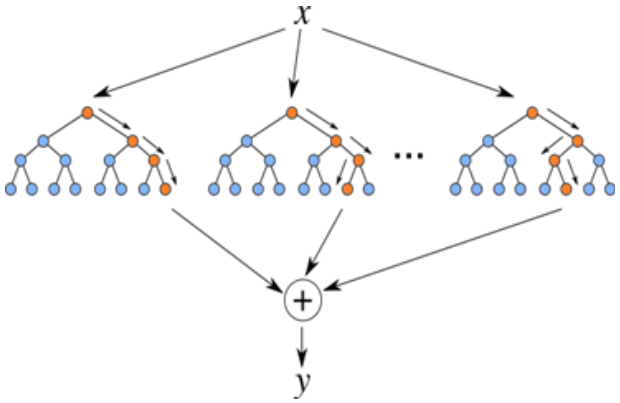

Figure 1. Random Forests Regression

Sample set for a study N input-output data

$$D = \{(x_1, y_1), (x_2, y_2), \ldots, (x_N, y_N)\}\ \in\ R_k \times R \tag{2}$$

In addition, its function of regression is denoted as

$$F\ (f \mid f\ (x_i = w_T \cdot x_i + b,\ \ w\ \in\ R_k) \tag{3}$$

where w, b and x_i are normal vectors to the hyperplane, the input vectors, and the hyperplane's distance, respectively. The key idea is to use a non-linear mapping

process. The vector input high dimensional feature stores will be mapped using non-linear SVM. There are more chances that data can be separated linearly [14]. The formulated problem can be seen below.

$$minimize \quad \frac{1}{2}||w||^2 + C\ \sum_i(\xi_i + \xi_i^2) \tag{4}$$

$$y_i - (w^T\phi(x_i) + b) \leq \epsilon + \xi_i^* \tag{5}$$

where ξ stands for the slack variable, and C is the cost function and measures the model's precision, ϵ represents the error allowed for each point of the training set. The model accuracy will be significantly higher if C is more significant, but overfitting may result. A big hyperplane will be used, if C is tiny on the con tray side. There may be misclassified samples if the training set is linearly separable. Special kernel functions (x_i, x_j) can take the place of the mapping function $(x_i$) in the high-dimensional space, and the necessary calculations can be performed directly in the input space by performing kernel techniques on the kernels [15]. The method that has been studied the most is using artificial networks. However, the SVM outperforms traditional ANNs in regression and classification thanks to its strong body generalization ability. Due to its light-solving and flexible or variable control methods, the SVM algorithm is one of the options for prediction and modeling in various applications [16]. The point is considered a training example from the hyperplane sets or hyperplanes, which come in infinite space with many dimensions. As a result, a non-linear classification can be applied to the developed linear data classifier [17].

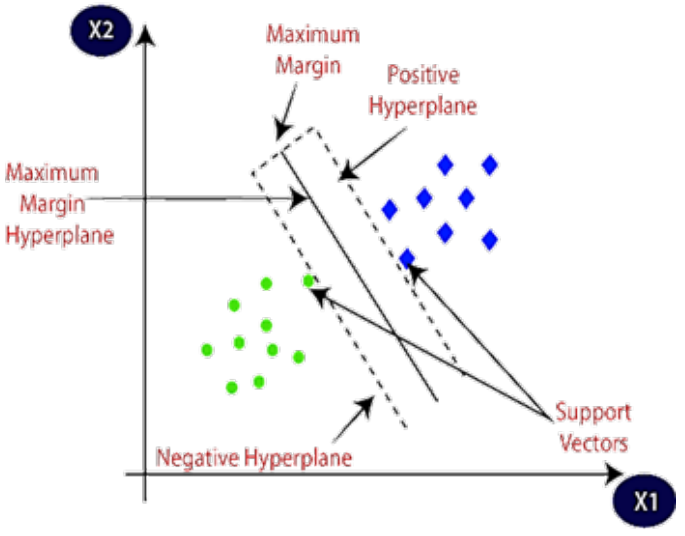

Figure 2. Support Vector Machine

The SVM algorithms' main goal is to make the aggregate decision boundaries gate the n^{th} dimensional spaces into classes so people plus can put the new data point into the appropriate categories shortly. The excellent decision boundary y

is a hyperplane. SVM calculates and uses support vectors that can help us create hyperplanes. In Figure 2, two main categories are classified using a decision boundary or hyperplane.

2.3 ARIMA Model

ARIMA is one of the essential forecasting methods that has been around since George Box and Gwilym Jenkins first introduced it. Contribution to the ARIMA model was published in the 1970s in a book titled time series analysis, forecasting, and control [18]. The methods and techniques introduced in their publication are still used today and can be called the Box-Jenkins approach. This is a very foundational technique. Based on ARIMA itself, many other autoregressive methods have also risen, so what happened in ARMA is even a time series that ARIMA uses the information contained in that series itself to predict future values.

Several organizations are very sensitive to sudden and significant changes in the future due to the error it can cause to even the essential systems. Whereby all requirements of financial firms are correctly and accurately predicting the future, the predictions become vital once you contemplate that they are the signal of survival and, therefore, the language of a commercial enterprise inside the world. The predicted values are mostly demand but can also be something else, like price or supply. At the same time, forecasting assumes future values of the studied variable forecasting method is divided into four types [19].

- Time-series
- Simulations
- Causals
- Qualitative

Time series is a collection of considerations organized in progressive order of, relating to, or arranged in or according to the order of time). Time-series forecasting models use mathematical methodology and approaches based on previous data to forecast demand. It is based on the premise that the coming time is an extension of the last; as a result, which may confidently estimate future demand using previous data. Research in different sectors and fields has been conducted on demand forecasting using time series analysis. They include demand forecasts for food sales, tourism, maintenance repair parts, power, automobiles, and other items and services. The predicting accuracies of time series analysis depend on the demand time series features. We will get high predicting accuracies if the transition curves are stable and periodic but will not achieve massive credibility if the loops have significantly different patterns [20].

To model time series: moving-average, exponential-smoothing, and ARIMA are examples of conventional statistical models that may be used to represent time series. The future values depend on the past data or are required to be linear functions.

Hence, these models are linear. The researcher has focused on the linear model over the past several years since they have shown to be simple to understand and apply. Another limitation of the traditional ARIMA technique is that determining a good model for time series data necessitates many observations. ARIMA model (p, q, d) is a kind of ARIMA model in which [21]. ARIMA model is given in Eq. 6, 7 and 8 where autoregressive (AR) part is given in Eq. 6, moving average (MA) part is given in Eq. 7. Integrated part is given as y_t' where $y_t' = y_t - y_{t-1}$ is first difference. Final equation of ARIMA is given in Eq. 8 as AR and MA combined with difference values.

$$y_t = \alpha + \beta_1 y_{t-1} + \beta_2 y_{t-2} + \cdots + \beta_p y_{t-p} + \epsilon_t \quad (6)$$

$$y_t = \alpha + \epsilon_t + \phi_1 \epsilon_{t-1} + \phi_2 \epsilon_{t-2} + .. \phi_q \epsilon_{t-q} \quad (7)$$

$$y_t' = \alpha + \beta_1 y_{t-1}' + \beta_2 y_{t-2}' + \cdots + \beta_p y_{t-p}' + \phi_1 \epsilon_{t-1} + \phi_2 \epsilon_{t-2} + .. \phi_q \epsilon_{t-q} + \epsilon_t \quad (8)$$

where;

p = number of autoregressive terms

d = order of differences

q = number of moving averages terms

METHODOLOGY

3.1 Dataset

There are nine months between 2018 and 2019 in the available data set. The dataset includes daily 15-minute data for the 1200 kWp solar power plant in the Istanbul Water and Sewerage Administration (ISKI)'s İkitelli Drinking Water Treatment Plant. Time is on the x-axis, and magnitude is on the y-axis. Additionally, equal time intervals were required on the y-axis. Python was used to read the data and plot it as a time series, as depicted in Figures 3 and 4. The ARIMA model's general procedure is as follows:

- Visualizing time series data and making the time series data stationary.
- Plotting, correlation, and auto co-relation for the values of 'p', ' d', and 'q'.
- Using rolling forecast method, model is trained in slices of data, and later used for forecasting.

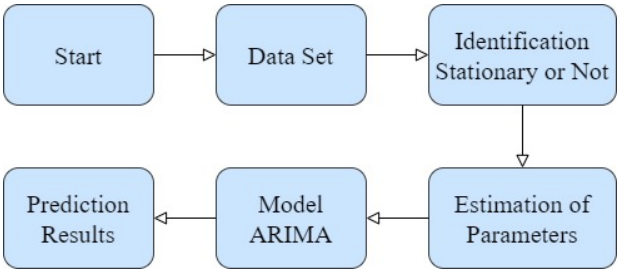

Figure 3. Flow chart of ARIMA model

Dataset is used for the month of June 2018 in the pre-processing modeling plot of our dataset. To know whether our data is stationary or not. Stationary data means that the data have a constant mean and variance over time, and non-stationary shows variation or without a constant mean over time. The primary requirement of ARIMA is to make our data stationary.

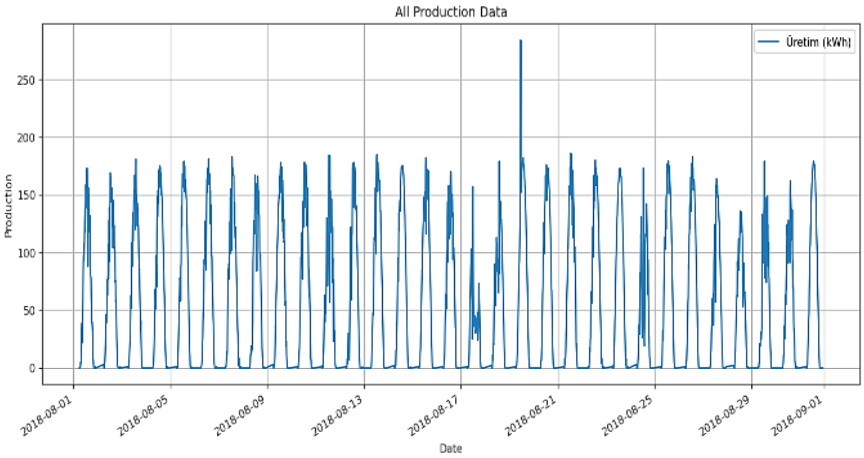

Figure 4. Time series analysis of all production data

3.2 Stationary / Not

After examining the plots, there is a statistical test to check whether our data is stationary. The test is called the augmented Dickey-Fuller *(ad fuller)* test for that purpose; we can import the *ad fuller* function from Python library stats models. In addition, passing our time series data in *ad fuller* will get a p-value if the value of 'p' is more significant than 0.05 means that the series is not stationary. However, our data is already stationary because our p-value is 0.000 and we will not have to use it.

The simple method is to find the difference that will subtract the past value from the given value so that the upcoming values will be different. Sometimes it depends on how complicated the series is, so in this case. There may be more than one difference that needs to be made. Therefore, the value of d represents the low number of differences in making data stationery. In addition, if the time series is stationary, the 'value will be zero. The upcoming terms are 'p' and 'q'. p is used for autoregressive it represents the number of lags of 'Y' and is used for prediction. q is used for moving average terms and represents the number of lagged forecast errors and the error values, which will use in the ARIMA model.

3.3 Auto-Regressive and Moving Average Model

The partial auto-correlation function (PACF) and auto-correlation function (ACF) can be used to determine the values of "p" and "q" to construct an ARIMA model that is accurate. The value p means autoregressive (AR) term and q means moving average (MA) or forecast error term. The plots of PACF and ACF are shown in Figure 5 and Figure 6.

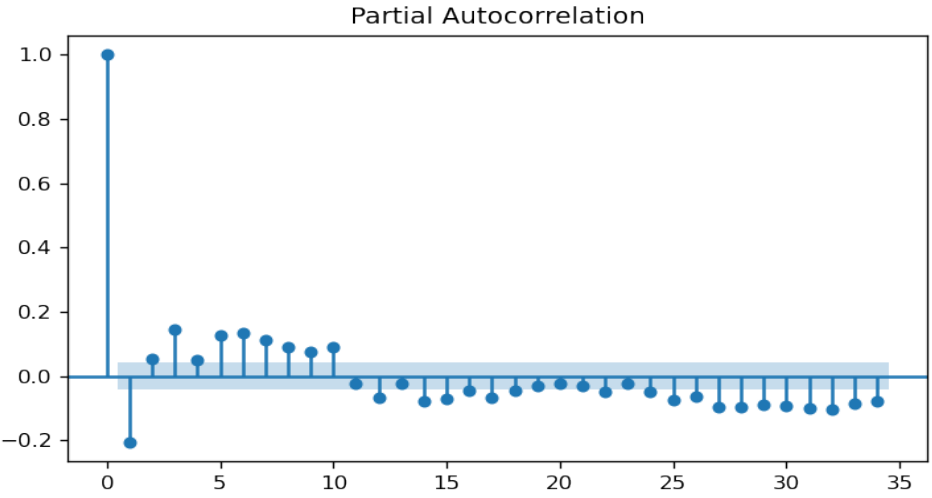

Figure 5. Partial Co-relation

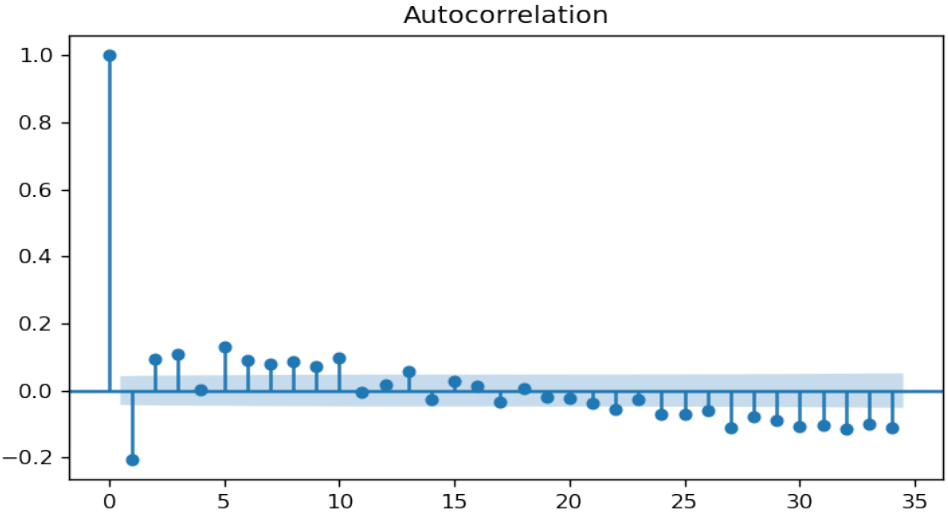

Figure 6. Auto Co-relation

PREDICTION RESULT

In Figure 7, blue is the original value, and red is the forecast value close to our actual values, so theoretically, our ARIMA model fits correctly. We got different model parameters from the PACF and ACF plots from the range (0 to 3) after using the AIC. The best combination is (2, 0, 3); the value of p, d, and q. You can easily see the difference between Mean Square Error and Root Mean Square Error-values is shown below in "Table 1" for ten different months starting from June until May.

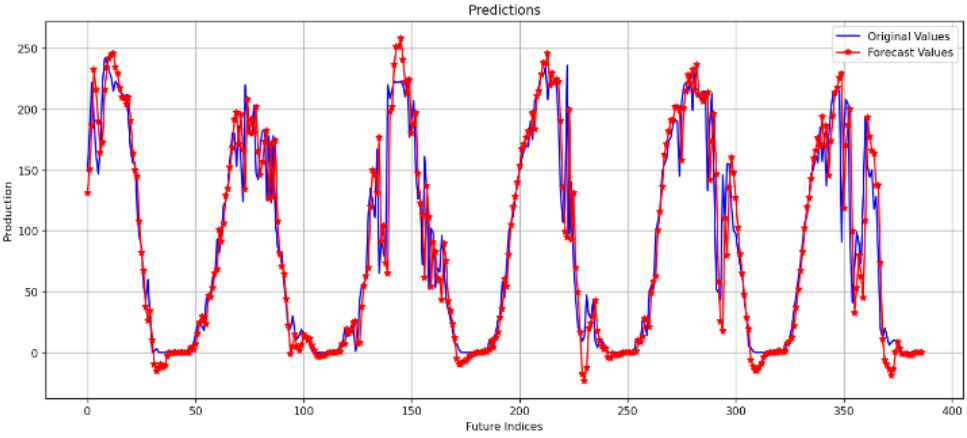

Figure 7. Final plot for prediction

Table 1. Error Metrics

Metrics for Mean Square Error and Root Mean Square Error									
Mon	**Jun**	**Aug**	**Sep**	**Nov**	**Dec**	**Feb**	**Mar**	**Apr**	**May**
MSE	56.80	35.23	56.11	23.80	44.96	61.04	74.4	78.21	83.49
RMSE	7.02	5.32	7.49	4.70	4.99	6.75	7.84	8.11	8.50

CONCLUSION

In this research paper, a model has been developed and examined to predict total solar energy generation using a simple and well-known time series method called ARIMA. Different techniques like ADF, ACF, PACF, and differencing tests are used in this model. Various combinations of ARIMA model parameters and AIC are compared to get the appropriate values. On the other hand, there might be other factors that can affect our models' accuracy. For the ARIMA model, our model must be stationary. If researchers do not know whether their system is stationary, they need to make an ADF test, and from the augmented Dickey-Fuller test, if our value of $p = 0$ means, our system is stationary. The value of p and q is calculated from PACF and ACF plots. Finally, this research will be a building block for predicting future solar energy generation. Our future work will compare all other machine-learning techniques and show which is more efficient and straightforward.

REFERENCES

[1] Khan, I., Zhu, H., Yao, J. and Khan, D. Photovoltaic power forecasting based on Elman neural network software engineering method. IEEE International Conference on Software Engineering and Service Science (ACCESS), 2017:747–750.

[2] Huo, J., Shi, T., and Chang, J. Comparison of Random Forest and SVM for electrical short-term load forecast with different data sources. 7th IEEE International conference on software engineering and service science (ACCESS), IEEE, August 2016:1077-1080.

[3] Kang, C., Xia, Q., and Zhang, B. Review of power system load forecasting and its development. Automation of Electric Power Systems, 2004, 28(17):1-11.

[4] Liao, N. H., Hu, Z. H., Ma, Y. Y., and Lu, W. Y. Review of the short-term load forecasting methods of the electric power system. Power System Protection and Control, 2011, 39(1): 147-152.

[5] Wu, X. Y., He, J. H., Zhang, P., and Hu, J. Power system short-term load forecasting based on improved random forest with grey relation projection. Automation of Electric Power Systems, 2015. 39(12):50-55.

[6] Chen, B. J., and Chang, M. W. Load forecasting using support vector machines: A study on UNITE competition 2001. IEEE Transactions on Power Systems, 2004, 19(4): 1821-1830.

[7] Box, G. E. P., and Jenkins, G. Time Series Analysis, Forecasting, and Control. Holden-Day, San Francisco, CA, 1970.

[8] Zhang, G. P. Time series forecasting using a hybrid ARIMA and neural network model. Neurocomputing, 2003, 50: 159-175.

[9] Chen, B. J., Chang, M. W., and Lin, C. J. Load forecasting using support vector machines: A study on UNITE competition 2001, IEEE Transactions on Power Systems, November 2004, 19(4): 182 1- 1830.

[10] Wu, X., He, J., Zhang, P. and Hu, J. Power system short-term load forecasting based on improved random forest with grey relation projection, Dianli Xitong Zidonghua / Automation of Electric Power Systems, 2015, 39(12): 50-55.

[11] Premalatha, M., and Naveen, C. Analysis of different combinations of meteorological parameters in predicting the horizontal global solar radiation with ANN approach: A case study. Renewable and Sustainable Energy Reviews, 2018, 91: 248-258.

[12] Ho, T. K. The random subspace method for constructing decision forests. IEEE Transactions on Pattern Analysis and Machine Intelligence, 1998, 20(8): 832-844.

[13] Ramedani, Z., Omid, M., Keyhani, A., Shamshirband, S., and Khoshnevisan, B. Potential of radial basis function-based support vector regression for global solar radiation prediction. Renewable and Sustainable Energy Reviews, 2014, 39:1005-1011.

[14] Gu, W., Wu, Z., Bo, R., Liu, W., Zhou, G., Chen, W., and Wu, Z. Modeling, planning and optimal energy management of combined cooling, heating and power microgrid: A review. International Journal of Electrical Power & Energy Systems, 2014, 54:26-37.

[15] https://levelup.gitconnected.com/random-forest-regression-209c0f354c84

[16] Deng, H., Fannon, D., and Eckelman, M. J. Predictive modeling for US commercial building energy use: A comparison of existing statistical and machine learning algorithms using CBECS microdata. Energy and Buildings, 2018, 163: 34-43.

[17] Yen, C. F., Hsieh, H. Y., Su, K. W., Yu, M. C., and Leu, J. S. Solar Power Prediction via Support Vector Machine and Random Forest. In E3S Web of Conferences, EDP Sciences, 2018, 69: 01004.

[18] https://www.javatpoint.com/machine-learning-support-vector-machine-algorithm.

[19] Shumway, R. H., and Stoffer, D. S. Time series analysis and its applications (Vol. 3). New York: Springer, 2000.

[20] Box, G. E., Jenkins, G. M., Reinsel, G. C., and Ljung, G. M. Time series analysis: forecasting and control. John Wiley & Sons, 2015.

[21] Anderson, T. W. The Statistical Analysis of Time Series, New York: John Wiley & Sons, 1971.

Chapter 11

MIMO ANTENNA WITH DUAL-BAND 28/38 GHZ FOR 5G APPLICATIONS

Nizar SGHAIER[1], Anouiar BELKADI[2], Islem Ben HASSINE[2]
Lassaad LATRACH[1], Ali GHARSALLAH[1]

1 University of Tunis El Manar, Faculty of Science of Tunis, Department of Physics, Laboratory for Research on Microwave Electronics, 2092, Tunisia
2 University of Tunis El Manar, Faculty of Science of Tunis, Department of Physics, UR-LAPER, 2092, Tunisia

INTRODUCTION

The last two decades have witnessed a meteoric growth of new information and communication technologies, with new innovative devices and services attracting more and more users. The number of subscribers to cell phone services continues to grow. According to the TeleGeography Institute, the world will have approximately 7.95 billion mobile subscribers by the end of 2019, compared to 6.97 billion in 2014. The internet, which can be considered the common thread between all these technologies, is increasing in traffic every year. According to a study by the Massachusetts Institute of Technology (MIT), more than 80% of internet traffic is carried out by mobile devices (smartphones, tablets, etc.) versus 12% with computers. More than 90% of mobile devices have access to the Internet via telephone operators and this number is increasing every year.

Faced with this growing demand, communication system designers are always challenged to make new advances in order to provide users with reliable, fast and available services. Although 4G seems to satisfy the current needs in terms of quality of service, it will not take into consideration the new specifications with the massive use of augmented reality, online video games and the arrival of autonomous cars, etc. These services require increasingly high data rates with very low latency [1-2].

To meet all these requirements, standardization bodies (3GPP, ITU, etc.) have established the 5G (or NR) standard for mobile telephony. 5G aims not only to increase bandwidth and network throughput, but also reduce the energy consumption of all network equipment and offer a stable and reliable service [3-5].

In order to achieve these objectives, 5G proposes the use of two frequency domains: the FR1 (frequencies below 6GHz (Sub-6GHz)) [6-9] and also the FR2 (millimeter band from 24GHz to 60GHz) [10-13]. The FR1 will be used primarily to ensure backward compatibility with existing networks. To overcome the problems of poor propagation of millimeter waves, the use of massive MIMO associated with MIMO beamforming is proposed. The NR is largely based on the implementation of small-cells inside the macro-cells. The small cells, connected to the macro-cells, will be directly implanted in access points in the vicinity of homes to reduce latency and also energy consumption [14].

In this context, several proposals for 5G antennas have been published. Researchers have worked on mono-band antennas as shown in references [15-17], other researchers in references [19-24] have made dual-band antennas and a triple-band antenna has been designed and simulated as shown in reference [18].

In this chapter, we will perform the manufacture of a 4x1 MIMO dual-band antenna for a Smartphone 5G FR2 band (millimeter band) band) 5G (28GHz and 38GHz). The designs and simulations are performed using CST software and the obtained bandwidth around 28GHz is (27.25 – 29 GHz) and that around 38GHz

is (34.5 – 41GHz). The antenna array (MIMO) consists of four identical antennas and the coupling between elements is less than -23dB. At 28GHz and 38GHz, the MIMO antenna's total gain is 9.7 dBi and 11.5 dBi, respectively.

METHODOLOGY OF DESIGN

The methodology for the design of the desired antenna consists of the following steps:

- To create on a Rogers type substrate of length Lp= 11 mm and width Wp=7 mm a patch of increasing shape of dimensions Lc =1.2mm and Dc = 2.7 mm which is fed by a microstrip line matched to 50 Ohm of length La= 6.3 mm and width 0.8 mm as shown in figure 1.a.
- To create a slot on the left with dimensions Ls= 1.9 mm and Ws = 0.3 mm and create a slot on the right with dimensions Ln= 1.6 mm and Wn = 0.3 mm as shown in figure 1.b.
- To create a slot below crescent with length Le= 1.4 mm and width We = 0.7 mm (see figure 1.c).
- The ground plane used is partial of length 6.3 mm (see figure 1.d)

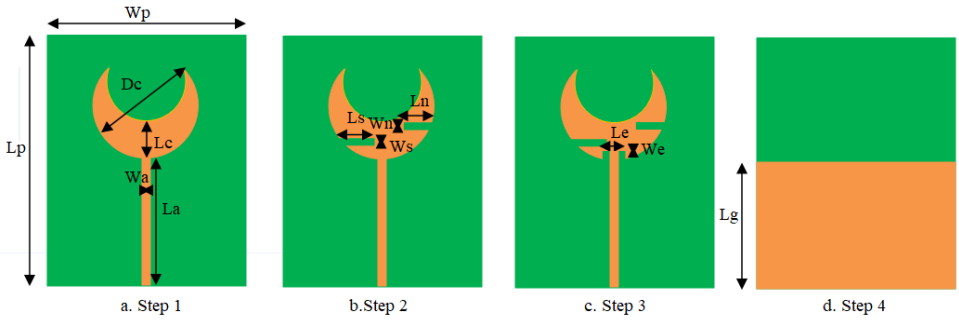

Figure 1. Methodology of Design

Figure 2 depicts the evolution of parameter S11. In the first step, the result of the simulation shows an appearance of the first 28 GHz frequency band. The second step allows the birth of a second band but not adapted. In the third and fourth step, we have archived the desired result i.e. a dual band antenna 28/38 Ghz.

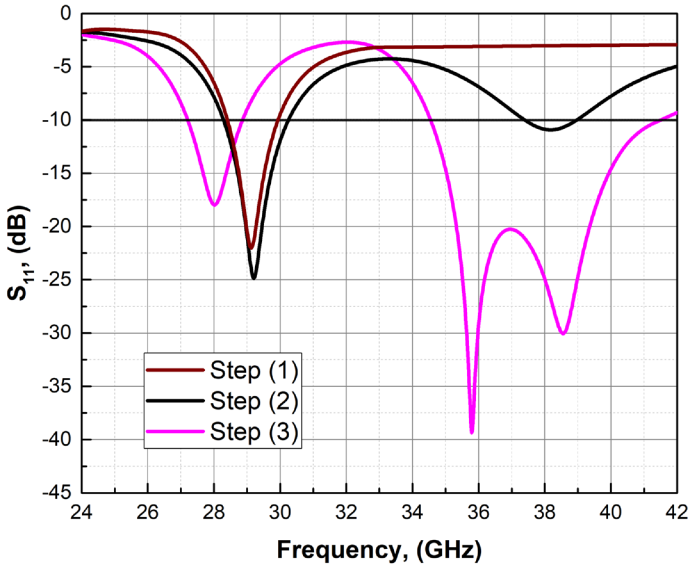

Figure 2. Evolution of parameter S11

To be sure of the simulated results we built the antenna and measured the reflection coefficient S11. Figure 3 indicates a good agreement between the simulated and measured results. The frequency bands realized by the antenna are: 27.25 to 28.9 GHz at 28 GHz and 34.5 to 40.5 GHz at 38 GHz.

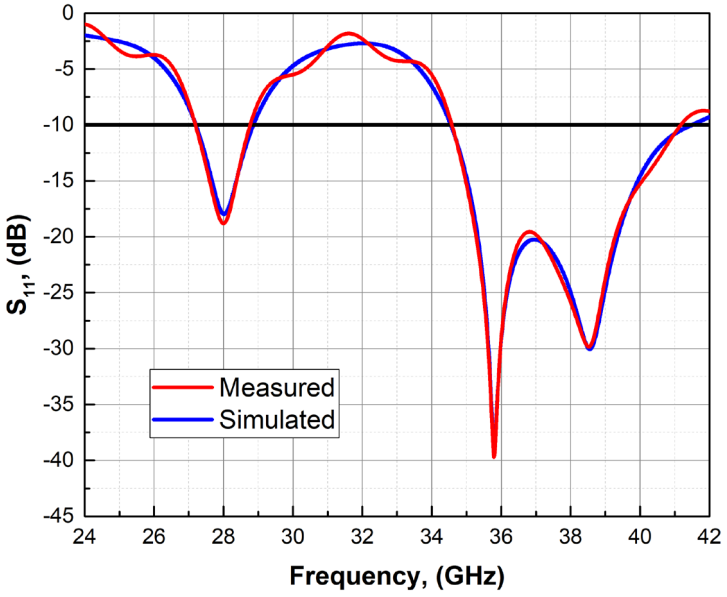

Figure 3. The reflection coefficient: simulated and measured

MIMO ANTENNA DESIGN

After the study and optimization of the radiating element, we started with a parametric study to design the MIMO antenna corresponding to the specifications. The desired structure of square shape with length 20 mm is illustrated in figure 4 and is composed by four radiating elements which are placed orthogonally in order to reduce the electromagnetic coupling.

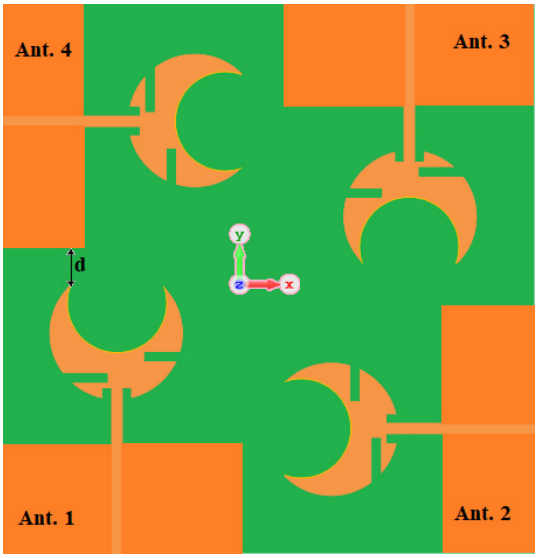

Figure 4. MIMO Antenna design

As mentioned in figure 5, to maintain the response of the radiating element the minimum distance between the antennas should be 3 mm and the optimum performance is taken at 4mm.

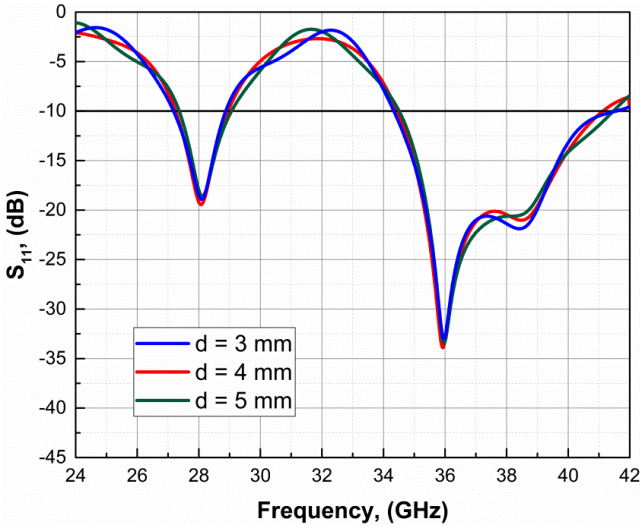

Figure 5. Reflection coefficient as a function of d.

To verify the isolation between the four radiating elements, we simulated the current distribution surface as shown in Figure 6. The concentration of the current density is only around excited port which confirms our model.

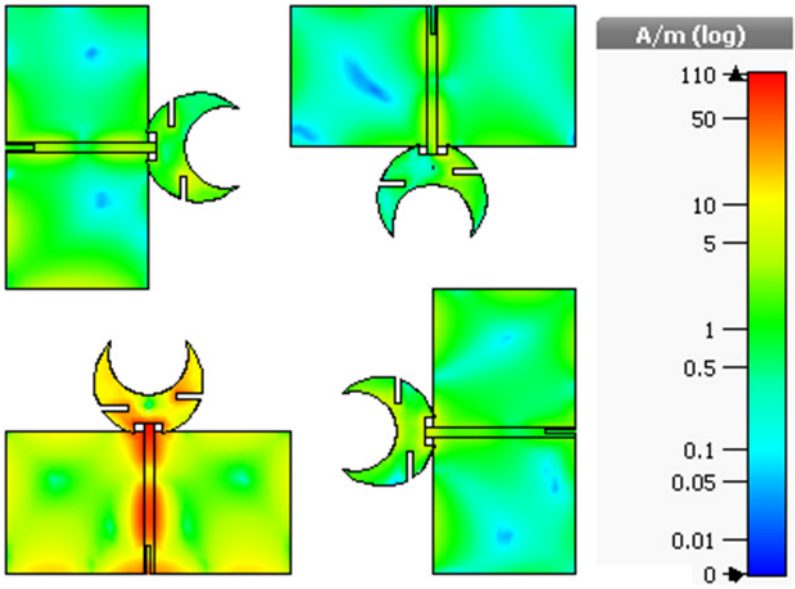

Figure 6. The distribution of surface currents.

RESULTS AND DISCUSSION

After setting up the desired structure, we built the antenna (see figure 7) to compare and validate the performances.

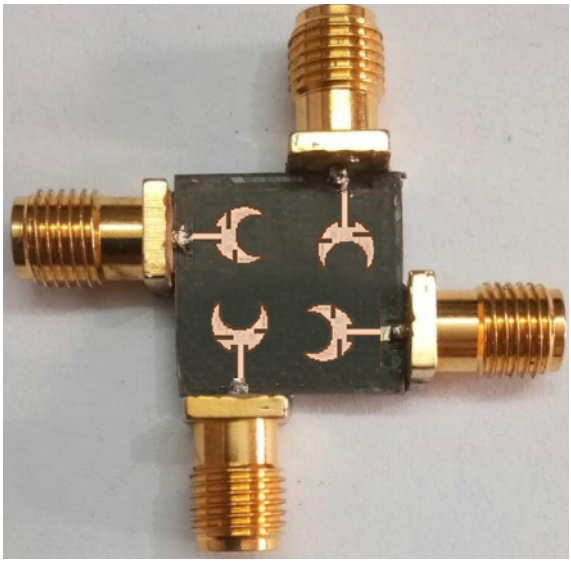

Figure 7. Photographs of the fabricated antenna.

S-parameters

In this section, we have measured and simulated the reflection and transmission coefficients (see figure 8). It is clear that our antenna allows covering two frequency bands around two resonant frequencies 28 Ghz and 38 GHz with an isolation that exceeds 24dB in both frequency bands.

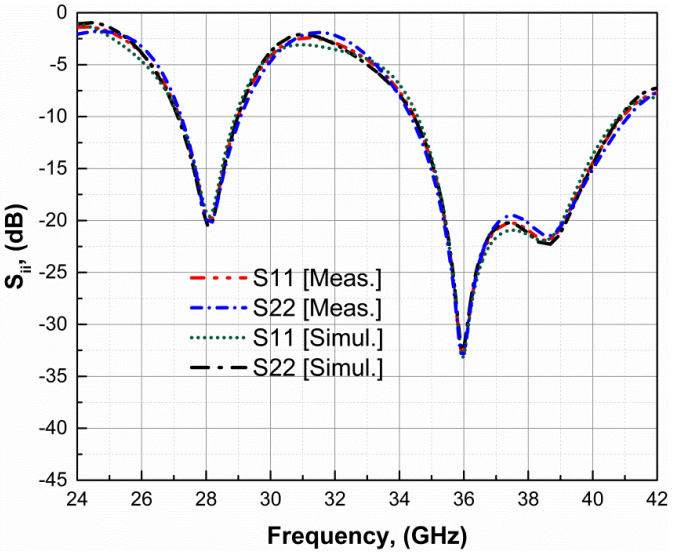

(a)

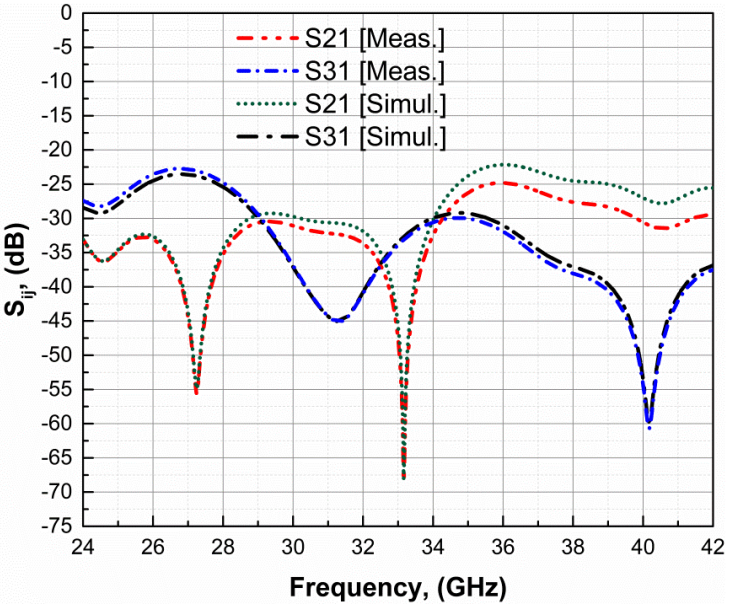

(b)

Figure 8. S-Parameter: (a) reflection and (b) transmission.

Radiation patterns

After confirming the frequency bands of the antenna, we measured the efficiency and gain of the antenna (see figure 9). Referring to the results, the efficiency of the antenna exceeds 80% for both frequency bands with a minimum gain are equal to 9.7 dBi.

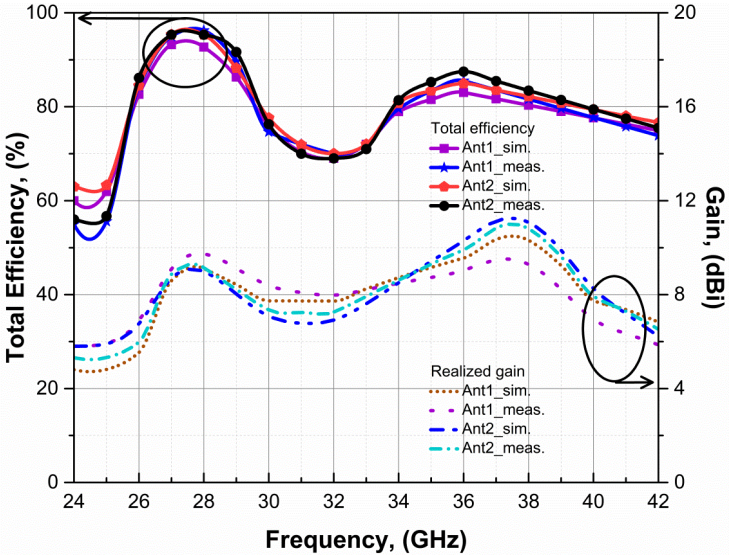

Figure 9. Radiation patterns: gain and efficiency.

Diversity Performance

The diversity performance is ideally composed of three elements which are: envelope correlation coefficient (ECC), diversity gain (DG), and channel capacity loss (CCL). In this paragraph, we measured and simulated the three parameters as shown in figures 10, 11 and 12.

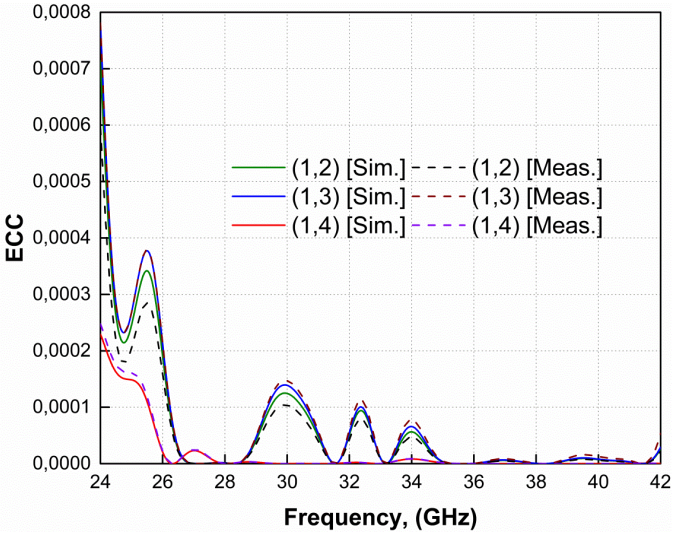

Figure 10. The simulated and measured ECC.

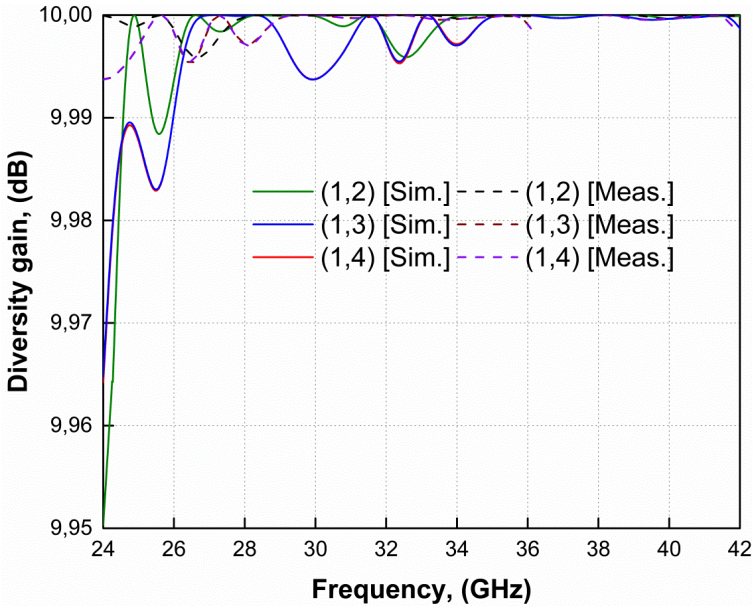

Figure 11. The simulated and measured DG .

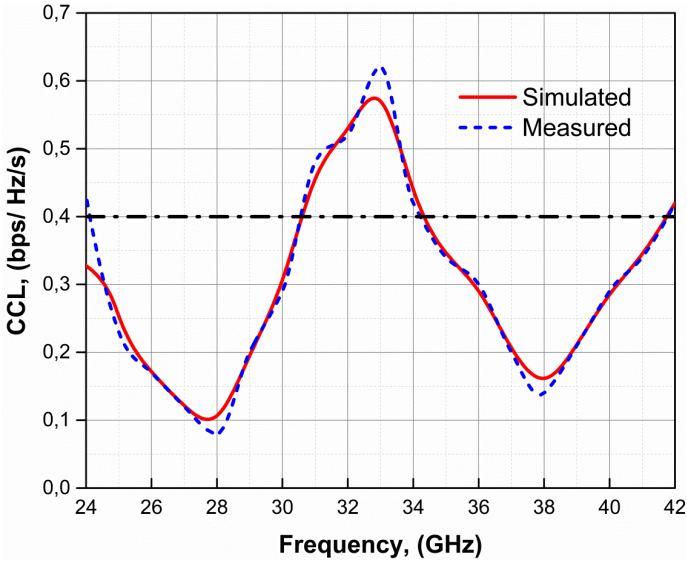

Figure 12. The simulated and measured CCL

We can conclude that the antenna has an ECC less than 0.0001, a DG more than 9.99 and a CCL less than 0.4 bit/s/Hz.

Performances

A performance comparison with the literature is made in table 1.

Table 1. Performance comparison

Reference	Freq., (GHz)	Eff., %	Isol., dB	ECC	Gain, dBi
[15]	28	82	17	0.01	8.3
[16]	28	86	40	0.0003	12
[17]	28	92	29	0.16	6.1
[18]	28/43/52/57	86.5-90	20	0.01	7.3/7.03/7.2/8.03
[19]	28/38	NA	30/22	0.0001	5.2/5.3
[20]	27/39	99.5/98.6	30/25	0.0001	5/5.7
[21]	28/38	91.2-89.6	27	NA	7/8
[22]	28/38	NA	24/20	0.01	6.6/5.86
[23]	28/38	86	30	0.004	7.58/5.72
[24]	28/37	NA	NA	NA	7.9 x 13.7
Proposed	28/38	83-95	24/25	0.0001	9.5/11.7

CONCLUSION

In this chapter we have realized the design of a dual-band MIMO antenna with four elements operating at $28GHz$ and $38GHz$ for smartphones. The obtained results, such as S-parameters, efficiencies, and radiation patterns, are exactly what MIMO systems require. The normally involves clearly demonstrates that our antenna design is a good potential candidate for future 5G millimeter band portable device applications.

REFERENCES

[1] Li, J.-F.; & Chu, Q.-X. (2011). "A Compact Dual-Band Mimo Antenna of Mobile Phone". Journal of Electromagnetic Waves and Applications, 25 (11-12), 1577–1586. Doi:10.1163/156939311797164800.

[2] Kumar, J. P. and Karunakar, G. (2019). "Compact C-shaped MIMO diversity antenna for quad band applications with hexagonal stub for isolation improvement". International Journal of RF and Microwave Computer-Aided Engineering. doi:10.1002/mmce.21971.

[3] T. Yamada, T. Nishio, M. Morikura, and K. Yamamoto, "Experimental evaluation of IEEE 802.11ad millimeter-wave WLAN devices, " in Proc. 21st Asia–Pacific Conf. Commun. (APCC), Oct. 2015, pp. 278–282.

[4] Riaz, M. J., A. Sultan, M. Zahid, A. Javed, Y. Amin, and J. Loo, "MIMO antennas for future 5G communications, " 2020 IEEE 23rd International Multitopic Conference (INMIC), 1–4, IEEE, 2020.

[5] Sulyman, A. I., Nassar, A. T.; Samimi, M. K.; Maccartney, G. R., Rappaport, T. S.; & Alsanie, A. (2014). "Radio propagation path loss models for 5G cellular networks in the 28 GHZ and 38 GHZ millimeter-wave bands". IEEE Communications Magazine, 52(9), 78–86. doi:10.1109/mcom.2014.6894456.

[6] Sharaf, M. H.; Zaki, A. I.; Hamad, R. K. and Omar, M. M. M. (2020). "A Novel Dual-Band (38/60 GHz) Patch Antenna for 5G Mobile Handsets". Sensors, 20(9), 2541. doi:10.3390/s20092541.

[7] Ikram, M.; Nguyen-Trong, N.; Abbosh, (2019) "A. Multiband MIMO microwave and millimeter antenna system employing dual-function tapered slot structure". IEEE Trans. Antennas Propag., 67, 5705–5710. 10.1109/TAP.2019.2952461.

[8] Rappaport, T. S.; Xing, Y.; MacCartney, G. R.; Molisch, A. F.; Mellios, E. and Zhang, J. (2017). "Overview of Millimeter Wave Communications for Fifth-Generation (5G) Wireless Networks—With a Focus on Propagation Models". IEEE Transactions on Antennas and Propagation, 65(12), 6213–6230. doi:10.1109/tap.2017.2734243.

[9] S. H. Chae; S. Oh and S. Park, (2007) "Analysis of Mutual Coupling, Correlations, and TARC in WiBro MIMO Array Antenna," in IEEE Antennas and Wireless Propagation Letters, vol. 6, pp. 122-125, doi: 10.1109/LAWP.2007.893109.

[10] Jeong, M. J.; Hussain, N.; Park, J. W.; Park, S. G.;Rhee, S. Y. and Kim, N. (2019). "Millimeter-wave microstrip patch antenna using vertically coupled split ring metaplate for gain enhancement". Microwave and Optical Technology Letters. doi:10.1002/mop.31908.

[11] Feng, W.; Li, Y., Jin, D. ; Su, L. and Chen, S. (2016). Millimetre-Wave Backhaul for 5G Networks: Challenges and Solutions. Sensors, 16(6), 892. doi:10.3390/s16060892.

[12] Nizar S.; Lassaad L. and Ali G.,(2022) "Design of a Dual-Polarized UWB 5G NR Antenna", Wireless Personal Communications, Springer , 123 (2), 1293–1310. https://doi.org/10.1007/s11277-021-09181-w.

[13] Al Abbas, E.; Ikram, M.; Mobashsher, A. T. and Abbosh, A. (2019). MIMO Antenna System for Multi-Band Millimeter-Wave 5G and Wideband 4G Mobile Communications. IEEE Access, 7, 181916–181923. doi:10.1109/access.2019.2958897.

[14] Nizar S.; and Lassaad L., (2021) "Design and analysis of wideband MIMO antenna arrays for 5G smartphone application". International Journal of Microwave and Wireless Technologies, 14(4), 511-523. https://doi.org/10.1017/S1759078721000659.

[15] Khalid, M.; Iffat Naqvi, S.; Hussain, N.; Rahman; M., Fawad; Mirjavadi, S.S.; Muhammad Jamil, K.; Amin, Y. (2020) "4-Port MIMO Antenna with Defected Ground Structure for 5G Millimeter Wave Applications". Electronics, 9(1), 71. doi:10.3390/electronics9010071.

[16] Bilal, M.; Naqvi, S.I.; Hussain, N.; Amin, Y.; Kim, N. (2022) "High-Isolation MIMO Antenna for 5G Millimeter-Wave Communication Systems". Electronics, 11, 962. https://doi.org/10.3390/electronics11060962.

[17] Kamal, M.; Yang, S.; Ren, X.-C.; Altaf, A.; Kiani, S.; Anjum, M.; Iqbal, A.; Asif, M.; Saeed, S. (2021) "Infinity Shell Shaped MIMO Antenna Array for mm-Wave 5G Applications". Electronics, 10, 165. https://doi.org/10.3390/electronics10020165

[18] May Abd A. E.; Asmaa Elsayed F.; and Khalid Fawzy A. (2022) "Millimetric-Wave Quad-Band MIMO Antennas for Future Generations of Mobile Communications". Progress In Electromagnetics Research B, Vol. 95, 41-60. doi:10.2528/PIERB22010101.

[19] Sabek, A.R.; Ali, W.A.E. and Ibrahim, A.A. (2022) "Minimally Coupled Two-Element MIMO Antenna with Dual Band (28/38 GHz) for 5G Wireless Communications". J Infrared Milli Terahz Waves, 43, 335–348 https://doi.org/10.1007/s10762-022-00857-3.

[20] Ali, W. ; Das, S. ; Medkour, H. and Lakrit, S. (2021) "Planar dual-band 27/39 GHz millimeter-wave MIMO antenna for 5G applications" Microsystem Technologies, 27, 283–292 doi:10.1007/s00542-020-04951-1.

[21] Marzouk, H. M.; Ahmed, M. I. and Shaalan, A.-E. H. (2019). "Novel dual-band 28/38 GHz MIMO antennas for 5G mobile applications". Progress In Electromagnetics Research C, 93, 103–117. doi:10.2528/pierc19032303.

[22] A. E. Farahat and K. F. A. Hussein, (2022) "Dual-Band (28/38 GHz) Wideband MIMO Antenna for 5G Mobile Applications". in IEEE Access, vol. 10, 32213-32223. doi: 10.1109/ACCESS.2022.3160724.

[23] Thi Thanh Tu, D.; Gia Thang, N.; Tuan Ngoc, N.; Thi Bich Phuong, N. and Van Yem, V. (2017). "28/38 GHz dual-band MIMO antenna with low mutual coupling using novel round patch EBG cell for 5G applications". International Conference on Advanced Technologies for Communications (ATC). doi:10.1109/atc.2017.8167644.

[24] Aghoutane B.; Das S.; EL Ghzaoui M.; Madhav B.T.P.; El Faylali H. (2022) "A novel dual band high gain 4-port millimeter wave MIMO antenna array for 28/37 GHz 5G applications". AEU - International Journal of Electronics and Communications,145 , art. no. 154071. https://doi.org/10.1016/j.aeue.2021.154071.

ISBN: 978-625-6382-50-3

/egitimyayinevi
/egitimyayinevi
/egitimyayinevi
www.egitimyayinevi.com
siparişleriniz için: www.kitapmatik.com.tr